M.Sc. Project

Development of CO_2-O_2 CARS thermometry and concentration measurements for applied flame diagnostics

N. Griffioen

Technische Universiteit Delft

TU Delft

M.Sc. Project

Development of CO_2-O_2 CARS thermometry and concentration measurements for applied flame diagnostics

by

N. Griffioen

to obtain the degree of Master of Science
at the Delft University of Technology,
to be defended publicly on Tuesday April 6, 2021 at 09:30 AM.

Student number:	4275772	
Project duration:	March 19, 2020 – April 6, 2021	
Thesis committee:	Prof. Dr. Ir. P. Colonna,	TU Delft, chair
	Dr. A. Anisimov,	TU Delft, external examiner
	Dr. G.A. Bohlin,	TU Delft, principal supervisor
	Ir. F. Mazza	TU Delft, daily supervisor

An electronic version of this thesis is available at `http://repository.tudelft.nl/`.

TU Delft

Preface

The path that brought me here can be traced back to my first memories of watching nature documentaries as a little child. Through my experiences in South Africa, this fascination for nature grew into a desire to protect and a feeling of responsibility in ensuring the continuation of its existence. Human development and the ever increasing pressure it is exerting on the planet, is the main threat for a healthy co-existence between nature and humans in my eyes. Technology has enabled this human development and has been the catalyst for the rate at which it is expanding. One can not deny that technology has played a major role in the depletion of the planet's natural balances (destruction of the rain forest, climate change etc.). On the other hand however, it is also pivotal to realize that technology is largely driven by societal need and it is also thanks to technology that it is possible to put the impacts of big issues into perspective. Although technology has contributed to the creation of many current day issues, I believe it will also provide the solutions to resolve them.

This realization made me take the choice to pursue an education in engineering in order to equip myself with the knowledge and capabilities to contribute to the evolution of technology in ways that I believe lead to a prosperous future for both humans and planet. During the course of my master I had the chance to broaden my knowledge in the field of aerospace propulsion and power technologies and became especially intrigued by the application of coherent anti-Stokes Raman scattering (CARS) spectroscopy for flame diagnostics. Being impressed by the possibilities it offers, my curiosity grew in finding out what it takes to be part in the development of such a diagnostic tool. I became interested to know how it can be used to optimize combustion applications in the aerospace industry, with the aim of reducing the impact that modern air-breathing turbo-engines have on the environment.

When Alexis Bohlin came with the proposal of a thesis topic that would help to extend the capabilities of the current CARS system to measure CO_2, my enthusiasm was sparked and thus followed one of the best learning experiences I have yet gone through. Together with Francesco Mazza, who took on the role as my daily supervisor during the project, he helped me through each step of the way. Finally, we managed to create a functioning tool to measure both CO_2 and O_2 adding to the goal of making the CARS system at the TU Delft a truly multiplex diagnostic system. I sincerely hope that the small contribution from this project, will help in the greater picture of further developing cutting edge tools to reduce the environmental impact of combustion based propulsion systems in the aerospace industry, and beyond.

N. Griffioen
Delft, March 2021

Contents

List of Figures

List of Tables

Abstract

In this M.Sc. thesis project a model is developed and validated that simulates the coherent anti-Stokes Raman scattering (CARS) signal of CO_2 and O_2 in the spectral region between 1250cm^{-1} and 1680cm^{-1}. The aim is to perform temperature and concentration measurements in a typical hydrocarbon-air combustion flame. The project makes use of a two-beam time resolved CARS setup, with ultraboadband generated light from the pump/Stokes beam to excite the Raman transitions in this spectral window. In the 1250-1680cm^{-1} region, CARS signatures of both CO_2 and O_2 are visible making it possible to perform thermometry on both molecular species, while also offering the option of evaluating relative CO_2-O_2/O_2-CO_2 concentrations. The appearance of the oxygen ro-vibrational (O-, S- and Q-branch) spectrum at low temperatures, along with a strong manifestation of the CO_2 Fermi influenced Q-branch (with red-shifted peaks below 1300cm^{-1} and blue shifted peaks above 1350cm^{-1}) at higher temperatures, makes it possible to perform thermometry in low and high temperature combustion environments on both the reactant and product side. A total of 256 vibrational levels for CO_2 are taken into account for the model to simulate the CO_2 Fermi polyad. From these 256 vibrational levels, 181 Raman transitions are possible that fulfill the criteria of Δv_1=1, Δv_2=0, Δv_3=0, Δl=0 and ΔJ=0 . Three different experiments are performed including an M-flame, a V-flame and two experiments conducted in air for model validation. The temperature analysis using CO_2 provided satisfactory results regarding temperature assessments. Depending on the experiment, standard deviations below 2.3% and mean temperatures to within 1% of the temperatures corresponding to the expected values. The O_2 analysis showed a good correspondence to the CO_2 temperature values, differing by 40-82K. The O_2 analysis showed low standard deviations for the air temperature assessment (3.27%) and predicted the ambient temperature with a difference lower than 2K. The M-flame experiments showed the least correspondence to actual values. These unsatisfactory results can for one part be attributed to the high signal-to-noise ratios (SNR) and for one part due to the flickering of the flame. In terms of concentration assessment the model closely evaluates O_2-CO_2 concentrations in the ambient air and from an exhaled human breath, while the flame assessments had a mediocre correspondence to the predicted ones from *chem1d*. All in all the project shows that CO_2 temperature and concentration measurements in this CARS spectral region is feasible. It offers promise from a combustion perspective due to the possibility of performing simultaneous (O_2) rotational and (CO_2/O_2) vibrational thermometry, which makes it possible to perform measurements on both the product and reactant side of the flame front, while including spectral signatures of possibly three major molecular combustion species: CO_2, O_2 and H_2. Further improvements to the model and the application of the technique, make more complex combustion studies possible and help achieve the goal to develop a ultrafast, multiplex, state-of-the-art laser diagnostic tool for gas phase combustion measurements.

Introduction

Due to an immense population of over 7 billion people, humanity is having an unprecedented impact on our planet's ecology. One of the biggest challenges being climate change caused by the emission of greenhouse gases (GHG). Greenhouse gas emissions are still increasing globally with the biggest influence coming from the emission of carbon dioxide (CO_2) through the burning of hydrocarbon-based fossil fuels. Atmospheric fossil fuel combustion leads directly to the emission of CO_2, being the primary product of the chemical reaction along with water vapour. Nevertheless, fossil fuel combustion is still deeply rooted in our economy and transport systems. Especially the shipping and aviation industry still heavily rely on it, with virtually no feasible sustainable alternatives available [1]. As such, it is essential to find ways of reducing their impact by lowering the carbon footprint of the engines these systems operate on. Consequently, the current combustion technologies constantly need to be revised and improved, in order to minimize their CO_2 emissions and explore new fuel alternatives. This means investigating the very details of the chemical processes that play a role in fossil fuel combustion, a study which requires state-of-the-art diagnostic tools for meaningful and effective analysis. Within the field of combustion diagnostics, coherent anti-Stokes Raman scattering (CARS) spectroscopy has emerged as a top of the shelf, laser diagnostic tool for chemical species concentrations and temperature measurements in gas-phase environments. Its non-intrusive, in-situ measurement capability combined with a high spatial and temporal resolution makes CARS a valuable technique to employ in this research area.

The M.Sc. project presented in this document aims to extend the capabilities of the CARS system at the "Ultrafast Laser Diagnostic Laboratory", to the measurement of CO_2-O_2 temperature and concentrations. The M.Sc. topic falls within the wider scope of an ongoing project at the Technical University (TU) of Delft, that aims to develop a ultrafast, multiplex, state-of-the-art laser diagnostic tool for gas phase combustion measurements. The implementation of this capability to measure CO_2, requires the generation of a model that simulates the CO_2 CARS spectrum. This model can then be employed in combination with a fitting algorithm to determine CO_2 temperature and concentration from experimental CARS spectra obtained in a typical hydrocarbon-air flame. In doing so, a special method for determining temperature and concentration is investigated. By looking at a specific section ($1250 cm^{-1}$-$1680 cm^{-1}$) of the CARS spectrum, it is possible to perform relative concentration measurements on carbon dioxide as well as oxygen. Additionally it offers the possibility of performing rotational and vibrational temperature measurements simultaneously. Both CO_2 and O_2 play a chief role in the chemical reaction processes related to the combustion of hydrocarbon fuels. While CO_2 is more prominent on the product side and O_2 is represented in higher concentrations on the reactant side. This combination makes the approach interesting from a combustion diagnostic perspective, as both can serve to validate predictions made by current combustion models and contribute to experimental analysis.

The thesis is organized into five main chapters. *Chapter 1* covers some of the basic theoretical concepts regarding coherent Raman scattering that need to be understood in order to better apprehend the discussions that follow in later chapters. *Chapter 2* then covers the details regarding the model that is employed to simulate the molecular responses for carbon dioxide and oxygen. This is then followed by *chapter 3* where the CARS system and experimental setup are presented. Subsequently, *chapter 4* elaborates on the steps taken in the data processing and presents the results, including the spectral fits and frame by frame temperature analysis. Finally, *chapter 5* states the relevant conclusions and offers suggestions on how to further improve the measurement capability in the near future.

1 Theory

This first chapter covers the underlying theoretical notions that describe CARS, and make it possible to simulate the CARS spectrum of CO_2 in *Matlab*®. First, Raman scattering in general is described in section 1.1, before section 1.2 specifically describes coherent Raman scattering and how it relates to the molecular energy structure. Section 1.3 presents the advantages and basic working principles of the two beam CARS system used at the laboratory. Finally, section 1.4 explains how the vibrational modes of CO_2 relate to its species specific energy structure and how it translates into the resonant lines that can be observed in the laboratory and modelled using *Matlab*®.

1.1. Raman Scattering

Raman scattering is a form of light-matter interaction that involves the inelastic scattering of light from molecules. It occurs through an energy exchange between the incoming light photon and the considered molecule. If a given molecule is excited (e.g. by an incoming photon), it takes on a higher energy level. If it stays at this excited state the molecule has absorbed the incoming energy and "stored" it in one of its degrees of freedom. For the molecule to drop from an excited energy state to its ground state, it has to loose energy, which can be done through the emission of a photon. This can occur in two different ways, either through spontaneous (incoherent) emission or through stimulated (coherent) emission. In general the changes in energy that accompany these processes follow the conservation of energy according to the Planck-Einstein relation, eq. (1.1). Here $\hbar = \frac{h}{2\pi}$, where h is the the Planck constant, ω the frequency and E the energy.

$$\hbar\omega = E_{excited} - E_{ground} \tag{1.1}$$

Scattering of light occurs when a photon is absorbed, and immediately re-emitted by a molecule. One could view it as the photon colliding with the molecule resulting in an exchange of energy, where the direction of this scattered photon is dictated by the conservation of momentum. There are two forms of scattering, one is elastic (or Rayleigh) scattering and the other is called inelastic (or Raman) scattering.

Elastic in this case means that the incoming photon is scattered at the same frequency as it came in, resulting in a net zero shift in internal energy.

Inelastic means that the outgoing photon is shifted in energy compared to the incoming one, making the outgoing photon higher or lower in energy, entailing a change in internal energy of the molecule.

The inelastic energy shift is called Stokes shift if the photon is re-emitted at a lower frequency and anti-Stokes shift if it is re-emitted at a higher frequency. Figure 1.1 a) provides a diagram that describes the different scattering pathways. Alternatively these shifts are called red-shifts for the lower energy shifts and blue-shifts for the higher energy shifts, owing to such a frequency difference.

In fig. 1.1 b) a schematic on inelastic scattering is given. The distribution of the scattered photons over the frequency domain determines the so-called "power spectrum" of the Raman-scattered light. This is what then translates into the spectral lines, corresponding to specific shifts in energy and energy level populations. Every molecular species has its own rotational and vibrational energy structure, that induce very specific shifts in energy levels resulting in a spectral 'fingerprint' for each molecule. This fingerprint is what makes it possible to distinguish between different molecular species, making simultaneous multi-species analysis possible (i.e. multiplexed spectroscopy).

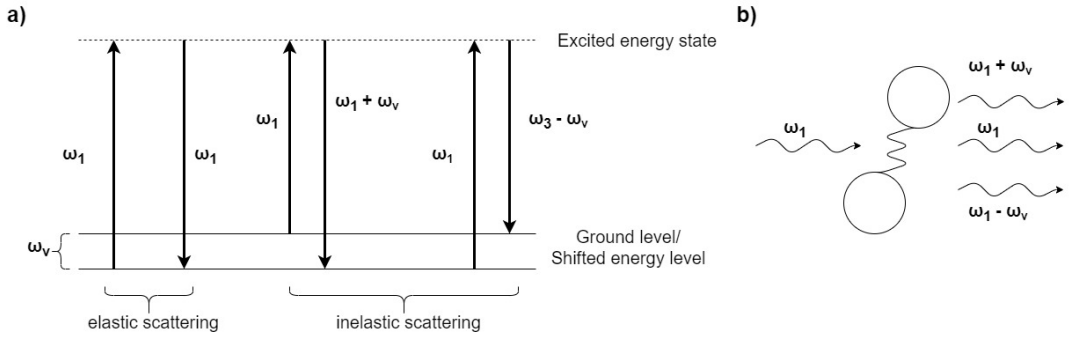

Figure 1.1: a) Schematic of different light scattering mechanisms showing the energy shifts from a given initial ground level to an excited energy state and either dropping back to the initial ground level (elastic) or a different energy level (inelastic). b) Schematic of spontaneous Raman scattering where ω_v is the resonance frequency of the molecule [2].

1.2. Coherent anti-Stokes Raman Scattering

The energy of a molecule can be characterized by three energy modes: rotational, vibrational and electronic [3]. The first two are related to the motion of the nuclei, while the electronic energy modes are related to the motions of the electrons. The energy transitions from one energy state to another can include changes in one, two or all three of these energy modes. These three types of energy modes can be decoupled, which occurs via the Born-Oppenheimer approximation. The latter essentially leads to the splitting of the total wave function into distinct nuclear and electronic wave functions. The theoretical notions regarding the wave function will not be discussed in this work as it requires a deeper look into the domain of quantum mechanics, deemed unnecessary for understanding the theory at hand. In physical terms, the Born-Oppenheimer approximation enables the assumption that the variation of the electronic wave function with the nuclear coordinate is small. In more simplistic terms, one could see it as the electrons moving at much greater speeds around the nuclei, than the vibrational and/or rotational oscillations of the nuclei themselves. Hence, the electronic energy modes and the energy modes related to the motions of the nuclei can be treated as two independent energy systems. Similarly, since the variation of the vibrational motion is small with changes in rotational motion, both can (in a first approximation) be treated as separate energy systems. Regarding the CARS technique applied in this thesis work, the energy modes of interest are the rotational and vibrational energy modes. Consequentially, one vibrational energy mode can be subdivided into a multitude of rotational energy modes. In the same manner, one electronic energy mode (or energy configuration) can be subdivided into multiple vibrational energy modes (see fig. 1.2).

For a preliminary understanding of the rotational and vibrational modes, it helps to consider the case of a diatomic molecule (e.g. O_2-oxygen or H_2-Hydrogen), treated as a rigid, non-vibrating rotor. From Quantum mechanics, the energy contained in a rotor is quantized according to the relation [3]:

$$E_r = hcBJ(J+1) \tag{1.2}$$

where J is the rotational quantum number , J=0, 1, 2, ... and B is the rotational constant, h is the the Planck constant and c is the speed of light. Strictly speaking however, a diatomic molecule is not a rigid rotator, where increased rotational motion, leading to higher rotational energy, goes hand in hand with distortions due to centrifugal effects. This is corrected by the introduction of the centrifugal correction term D, such that:

$$E_r = hc[BJ(J+1) - DJ^2(J+1)^2] \tag{1.3}$$

The inclusion of the centrifugal correction term, results in a decrease of the energy gaps between subsequent rotational quantum levels. The vibrational energy modes can to a first approximation be modelled as a harmonic oscillator with vibrational frequency ν. From quantum mechanics only certain discrete energy modes or energy levels are possible, given by the equation:

$$E_v = h\nu(v + \frac{1}{2}) \tag{1.4}$$

where v is the vibrational quantum number. Equation (1.3) however, is only applicable to a certain extent and does not encompass enough detail regarding molecular physics. The Morse potential shown by the solid, curved line in fig. 1.2 gives a more complete description, including the effects of molecular dissociation and

nuclear repulsion. If the internuclear distance is increased to infinity it will require enough energy to overcome the electromagnetic attraction leading to molecular dissociation. This energy is called the dissociation energy E_{dis} . On the other hand, reducing the internuclear distance leads to strong repulsion of the positively charged nuclei. The Morse potential is described by a relation including the species-specific constant a, the associated dissociation energy E_{dis} and the change in internuclear distance d from the equilibrium internuclear distance d_{eq}:

$$V = E_{dis}[1-\exp(a\cdot\Delta d)]^2, \Delta d = d_{eq} - d \tag{1.5}$$

An important consequence of the Morse potential is that the energy "ladder" becomes non-equidistant (see fig. 1.2). The energy jumps from one vibrational energy level to another become smaller going up the ladder. The vibrational energy used to describe a given energy level now contains higher order terms, and includes the anharmonicity constant x_e, following the equation [3]:

$$E_v = hc\left[\omega_e\left(v+\frac{1}{2}\right) - \omega_e x_e\left(v+\frac{1}{2}\right)^2 + \cdots [\text{ Joule }]\right. \tag{1.6}$$

where $\omega_e = \nu/c$ is the equilibrium vibrational coonstant expressed in wavenumbers (unit: cm^{-1}), c being the speed of light and v being the vibrational quantum number taking values v=0, 1, 2, ... For one vibrational level eq. (1.6) can be reduced to $E_v = hcG_v$, where G_v is the evaluated term in the square brackets, representing the shift in vibrational frequency, relative to the ground vibrational state (v=0). In reality, a molecule rotates and vibrates at the same time. The vibrational motion of the molecule has an effect on the rotational moment of inertia, leading to a change in rotational energy. Consequentially, the rotational constant B and centrifugal constant D, depend on the vibrational motion. This is taken into account by introducing small corrections, leading to the equations:

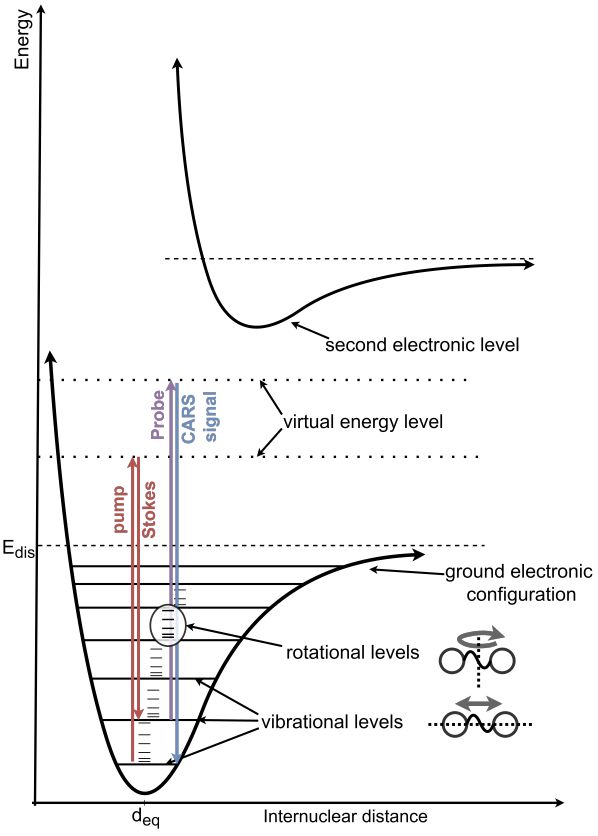

Figure 1.2: Diagram showing the distribution of electronic, vibrational and rotational energy modes of a diatomic molecule. One electronic energy configuration is characterized by the Morse potential (solid, curved line), subdivided into multiple vibrational levels, which in turn are subdivided into multiple rotational energy levels. The energy transitions related to CARS, showing the pump/Stokes, probe and CARS signal is depicted. The pump and probe photons excite the molecule to a virtual energy level, located in between two electronic states.

$$B_v = B_e - \alpha_e(v+1) \tag{1.7}$$

and,

$$D_v = D_e - \beta_e(v+1) \tag{1.8}$$

where e refers to the equilibrium positions of the nuclei and α_e and β_e are correction terms. Finally, eq. (1.3) and eq. (1.6) can be combined into one equation describing one rotational energy "ladder" for one specific vibrational level within one electronic configuration of a molecule:

$$E_{vJ} = E_v + E_r = hcG_v + hcB_vJ(J+1) - hcD_vJ^2(J+1)^2 \quad \text{[Joule]} \tag{1.9}$$

Thus, CARS is a quantum mechanical concept, where the molecular energy is characterized by specific energy levels. Transitions between these energy levels result in quantized energy "jumps", unique for every molecular species. Every transition from one energy state to another, corresponds to a specific transition frequency directly related to the energy difference between the initial and final state:

$$\omega_{n,m} = \frac{2\pi}{hc}(E_m - E_n) \quad [\text{cm}^{-1}] \tag{1.10}$$

Here subscript n denotes the initial state and subscript m the final state. The transition frequencies indicate where the resonant lines occur in the CARS spectrum. The Raman shifts observed in CARS directly result from these transitions between energy states, caused by changes in rotational and vibrational oscillations. In coherent anti-Stokes Raman scattering spectroscopy, the goal is to exploit these Raman modes by actively driving the oscillations through laser excitation. In many works concerning CARS, one often speaks of S-, Q- and O-branches. Depending on the nature of the energy transitions, they can be categorized as purely rotational branches or a combination of rotational and vibrational (ro-vibrational) transitions. In the table below, a quick overview is given of the selection criteria.

Table 1.1: Selection criteria for CARS spectral branches.

Transition type	Δv	ΔJ	Branch
Pure-rotational	0	+2	S
Pure-rotational	0	-2	O
Ro-vibrational	+1	0	Q
Ro-vibrational	1≤	+2	S
Ro-vibrational	1≤	-2	O

In practice this is achieved in two steps, the coherent preparation of the molecule by the pump/Stokes photon pair and the scattering of the probe beam. First, two incoming light fields at two specific frequencies ω_1 and ω_2, with two specific electric fields E_1 and E_2 are directed onto the molecule. The fields E_1 and E_2 can be modelled by the following equation [2]:

$$E_k(t) = A_k e^{i\omega_k t} + c.c \tag{1.11}$$

Where k=(1,2), i represents the imaginary part, ω is the frequency, t is time and A is the amplitude of the electric field. These two electric fields drive an oscillatory mode with resonance frequency ω_ν, assuming ω_1 and ω_2 are much higher than ω_ν and $\omega_1 > \omega_2$. It should be noted here that the high frequency oscillations of the individual electric fields do not permit the nuclei to follow. If the fields are sufficiently intense however, the electrons that surround the nuclei can be assumed to follow the incident fields independent of the motions of the nuclei as a result of the Born-Oppenheimer approximation. This can lead to nonlinear electron motions occurring at combination frequencies $\Omega = \omega_1 - \omega_2$. The photons at frequencies ω_1 and ω_2 are termed as the pump and Stokes photons respectively. Looking at fig. 1.3, these terms originate from the ω_1 photon pumping the medium to an excited energy state and the second ω_2 photon, termed the Stokes photon induces a drop in energy level, by stimulated emission, resulting in a combination frequency Ω.

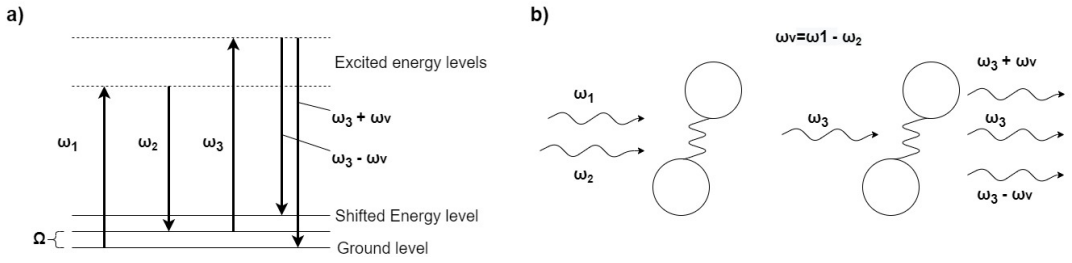

Figure 1.3: a) Schematic of Coherent Raman Scattering representing the energy shifts by the incoming lasers. ω_1 and ω_2 known as the the pump and Stokes beam respectively and ω_3 being the probe beam. $\omega_\nu + \omega_3$ is the emitted CARS signal when the molecule drops back to its initial energy state. b) Schematic of Coherent Raman Scattering [2], where the two incoming light fields aim to induce an energy shift $\Omega = \omega_\nu$ that is coherent with one of the characteristic Raman modes of the molecule. The third field then probes the prepared molecule developing side bands corresponding to the Stokes ($-\omega_\nu$) and Anti-Stokes shifts ($+\omega_\nu$).

Even though the frequencies ω_1 and ω_2 are too high for the nuclei to follow, the combination frequency Ω can be sufficiently low to allow the electronic motions to be coupled to the nuclear motions, permitting the electron field oscillation to drive an oscillation of the nuclear mode. The two incoming fields in this way introduce a time-varying force that oscillates at the difference frequency Ω. Once the molecule is prepared in this energy state a photon of a third field at frequency ω_3 is introduced, developing side bands that are shifted by Ω, resulting in Raman scattered radiation. When Ω equates the resonance frequency ω_ν the molecule is prepared in a coherent state and the amplitude of the electric field of these side bands are maximized

[2]. Figure 1.3 represents the procedure in a schematic form and is also included in fig. 1.2 for a change in vibrational level of 1 . It should be noted that all the frequency combinations where $\Omega \neq \omega_\nu$, contribute to what is called the non-resonant signal. If the non-resonant signal is too high it can lead to inadequate results with low signal-to-noise ratios (SNR), thus it is necessary to take measures that circumvent this issue.

In this way it is possible to drive the Raman modes of a given molecule and induce the scattering of light at Raman-shifted frequencies. The two incoming light fields are usually set to encompass a broader selection of frequencies ω_1 and ω_2 leading to a larger range of possible difference frequencies that match the frequencies corresponding to the energy shifts in one of the Raman modes. This procedure of "preparing" the probed medium is what is called coherent excitation of the molecules. This is opposed to spontaneous Raman Spectroscopy [4], where only the modes that are already excited (e.g. through energy from the combustion process) are probed. As such the term "coherent" in CARS refers to the coherent excitation of the molecular Raman modes by two incoming photons, before the probe photon is introduced, producing coherent light through the scattering of photons, which travel along the path of the probe beam. In spontaneous Raman scattering applications, incoherent light is produced, which is scattered in all directions, greatly reducing the signal intensity.

1.3. Time resolved two beam CARS

CARS comprises a multitude of different techniques, often optimized for a particular application. This project makes use of a hybrid femtosecond/picosecond (fs/ps) two beam CARS setup for studying chemically reacting gas-phase flows. The method maintains the advantages of *time-resolved* CARS techniques, by using a narrowband picosecond probe pulse that is preceded by a femtosecond broadband pump and Stokes pulse combination. This technique circumvents the influences of the non-resonant signal (see fig. 1.4) by offering sufficient temporal resolution, while keeping enough spectral resolution for detecting the frequency domain. The high peak powers associated with these pulses due to their short duration allow for impulsive CARS signal generation. This enables more efficient excitation of the coherence than ns-CARS applications, leading to higher signal levels, which facilitates the study of matter under extreme conditions [5, 6]. The short duration of the pulses being below the decay time of the molecular coherence, makes hybrid fs/ps-CARS a time resolved technique which is particularly suited for combustion diagnostics. The reasons for the decay of the molecular coherence can mainly be attributed to collisions between molecules leading to energy exchange. The latter is explained in more detail in section 2.2, but for the present section it suffices to be aware of the fact that the resonant signal decays over time. This decay happens on a time scale of a few hundred picoseconds, thus with a probe duration of a few picoseconds (<5ps) the CARS signal generation occurs on such a short time scale that the effect of the decay becomes negligible.

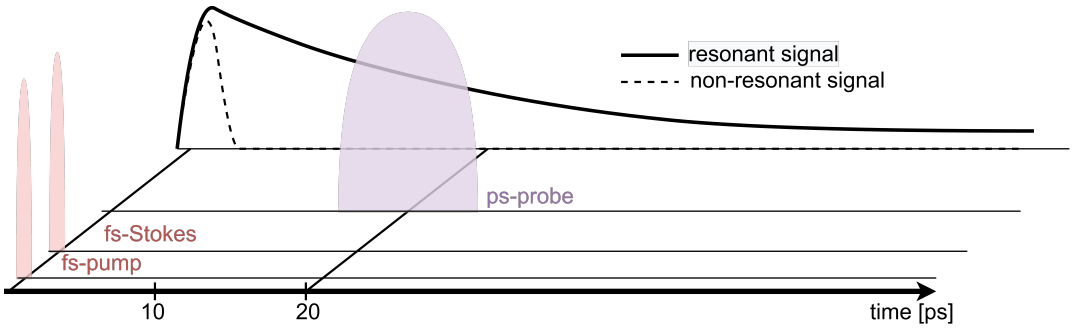

Figure 1.4: The short fs pump/Stokes pulse with high peak power, lead to a rapid decay of the non-resonant signal. The ps probe pulse then can be positioned after a significant decay of the non-resonant signal, leading to a more conclusive CARS analysis. Since the probe duration is still well below the decay time of the molecular response, this hybrid fs/ps technique can be regarded as time-resolved.

In the typical CARS application a total of three incoming lasers are used to generate the CARS signal. The technique used in this project however uses only *two beams*, as the pump and Stokes beams are degenerate [5]. In other words, pump and Stokes photons of different frequencies arrive simultaneously in time for the whole duration of the pump/Stokes pulse, due to the broadband laser beam (i.e. containing a range of photons at different frequencies). This development leads to simplifications on many levels. One simplification being that, because they come in one single beam the pump and Stokes photons are spatially overlapped and automatically synchronized at the measurement location. The shorter the pump and Stokes pulses, the higher the challenge of synchronizing them in the time domain. Thus, making the technique especially use-

ful when using ultra short laser pulses in the order of femtoseconds as applied in this work. Thanks to this spatial and temporal overlap of the pump and Stokes pulses two-beam CARS is also less susceptible to signal loss due to beam-steering than its three beam counterpart. Another favourable feature is that the resulting CARS signal co-propagates with the probe pulse, making it easier to align with the detector. Figure 1.5a) gives a schematic representation of how the changes in energy level are induced by the incoming lasers, with fig. 1.2 giving an example of the interaction chain for a Q-branch transition. The pump and Stokes photons coming in one beam, coherently excite the probed molecule such that its energy shift matches the frequency difference of the two photons.

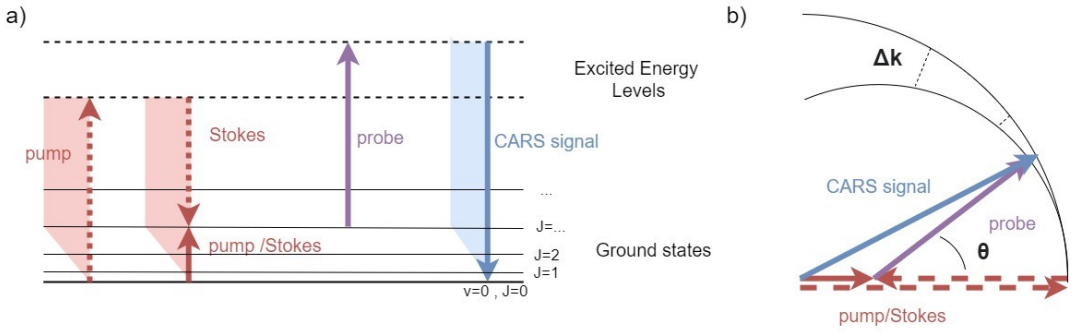

Figure 1.5: a) Raman shifts with the Pump/Stokes photons in one beam and a separate probe beam, generating a CARS signal.The dotted arrows represent the pump and Stokes photon pairs that come together in one beam, while the solid arrows represent the light beams corresponding to the two-beam CARS process.b) Phase matching scheme for the two-beam application with non-collinear beams (θ, beam crossing angle).

The crossing of the lasers in one point inside a gaseous volume will thus generate a third light beam, being the CARS beam. The CARS signal strength obtained by the crossing of these beams can be described by the following equation [5]:

$$I_{CARS} \sim \omega_{CARS}^2 I_{pump} I_{Stokes} I_{probe} |\chi_{CARS}|^2 z^2 \Big(\frac{sin(\Delta k z/2)}{\Delta k z/2} \Big)^2 \tag{1.12}$$

Where ω_{CARS} is the angular frequency according to the conservation of energy equal to $\omega_{probe} - \omega_{Stokes} + \omega_{probe}$, often described as the carrier frequency. I denotes the other beam intensities, while χ_{CARS} is the third order susceptibility of the CARS signal (discussed in section 2.1). Finally z is the probe volume length and Δk is a measure of the phase mismatch, $\Delta k = (k_{pump} - k_{Stokes} + k_{probe}) - k_{CARS}$ for which the wave vector phase matching scheme is shown in fig. 1.5b) . Proper phase matching is what allows the prediction of the direction in which the CARS beam is projected, dictated by the conservation of momentum, with k being the length of the wave vector. Since in a two laser setup the pump and Stokes photons come in the same beam with same direction, the direction of the CARS signal is mainly dependent on the beam crossing angle between the pump/Stokes and probe beam. The CARS signal will often be projected in roughly the same direction as the probe beam for a variety of beam crossing angles, with minimal phase mismatch [5]. Looking at eq. (1.12) the energy conversion and thus the CARS signal strength, is intensified through a minimization of the phase mismatch. Similarly, a longer interaction length and high intensities for the pump, Stokes and probe beams lead to a favourable increase in overall signal intensity.

1.4. Molecular energy structure of CO_2

Like mentioned in the previous discussion regarding the energy manifold of a diatomic molecular species, the CARS signal changes depending on the energy structure of the considered molecule. This energy structure is dependent on the spatial disposition of the atoms that constitute the considered molecule. As one can probably already predict, going from the example of a diatomic molecule, to a triatomic molecular species adds to the complexity of the problem since it adds to the degrees of freedom in which a molecule can vibrate and rotate. Carbon dioxide is a linear triatomic molecule with one rotational and three vibrational modes. The rotational mode comprises rotation around the axis perpendicular to the C-O bonds (y- or x-axis) shown in schematic form along with the vibrational modes in fig. 1.6.

In carbon dioxide the only Raman-active vibrational mode is the symmetric stretching mode v_1, left most schematic in fig. 1.6 .The asymmetric stretch shown in c) denoted as v_3, is infrared (IR) active. The degenerate

bending mode shown in d) and e) is designated as v_2 and like v_3 is IR-active. Every mode can occur at multiple energy levels, depending on the magnitude of the rotational or vibrational motion. These energy levels can be distinguished using a variety of notations. One commonly adapted notation is the one used in the HITRAN database ($v_1 v_2 l v_3 r$) introduced by Rothman and coworkers (1992) [7], where l represents the absolute value of the vibrational angular momentum quantum number (see fig. 1.8) and r numerates the Fermi level. Another notation that is widely applied, is the Herzberg notation $v_1 v_2^l v_3$ usually also including a symbol on the symmetry of the considered molecule.

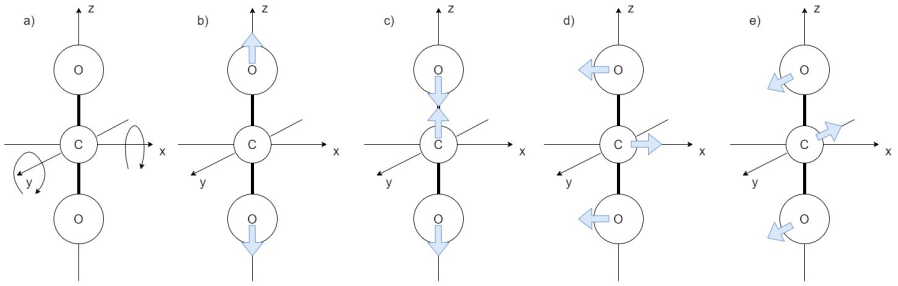

Figure 1.6: CO_2 rotational mode in a) and its vibrational modes from left to right: b) Symmetric stretch , c) Asymmetric stretch, d) degenerate xz bending and e) yz bending [8].

Symmetry becomes important when describing a phenomenon called Fermi resonances, which has a heavy influence on the Q-branch of CO_2. Fermi resonances occur when two molecular modes, of different ro-vibrational origin with equal symmetry, occur in close proximity to one another in the frequency domain. Thus, Raman active modes can interfere with IR-active modes and vice-versa. This can lead to the appearance of more peaks than expected in the frequency domain. As an example for CO_2, the first v_1 Raman active mode is located at a frequency shift of 1351cm^{-1}, while the IR-active $2v_2$ mode sits at a shift of 1344cm^{-1} from the ground level. Separated by only 7cm^{-1}, these modes interfere leading to a "splitting" of the Q-branch peak into two. One of the peaks is shifted to a slightly higher frequency than expected (1388cm^{-1}) and another peak that is shifted to a slightly lower frequency than expected (1285cm^{-1}). Using both the HITRAN and Herzberg notation , fig. 1.7 shows some of the relevant energy levels for CO_2 that lead to the occurrence of Fermi dyads in the Q-branch spectral region.

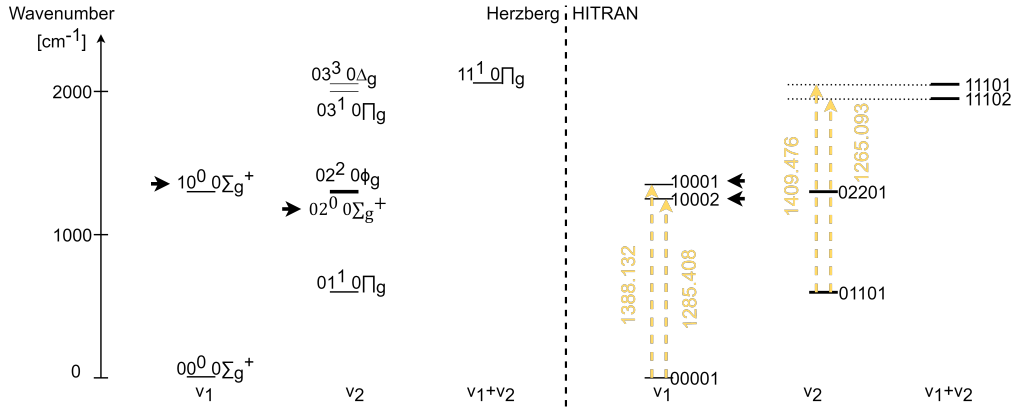

Figure 1.7: The first 7 vibrational energy levels according to the Rothman table with respect to their location in the frequency domain, given in the Herzberg (left) notation with symmetry symbols and the HITRAN (right) notation. The side with the HITRAN notation shows the energy transitions corresponding to the first two Fermi dyads observed at the CO_2 Q-branch.

The 00001→10002 and 00001→10001 transitions lead to the emergence of a 'red' and 'blue' Q-branch [9, 10] peak respectively, described as the $v_1/2v_2$ dyad. The Herzberg notation makes it possible to understand which vibrational levels can interfere and form Fermi peaks by looking at their symmetry. The black arrows indicate the interference of the 10^00 and 02^00 levels with a Σ-symmetry that are distinguished by Fermi level 2 and 1 respectively in the HITRAN notation. The other energy transition marked in fig. 1.7 are the 01101→11102 and 01101→11101 that lead to the so-called first CO_2 "hotbands" at a shift of 1264cm^{-1} and 1409cm^{-1}. These hotbands appear due to Fermi interference between the third level of the degenerate

bending mode $3\nu_2$ and the Raman active $\nu_1+\nu_2$ combined vibrational mode of CO_2. Next to the Q-branch dyad and the hotband dyad, a multitude of other Fermi peaks appear in this part of the CO_2 spectrum [3]. All of these peaks can potentially be used for CARS analysis of CO_2 vibrational temperature. Figure 1.7 also shows, that vibrational levels where the symmetric stretch mode (ν_1) is inactive can still act as an initial vibrational level for a molecule to make the transition to a vibrational level where the ν_1 mode is active. This means that for a molecular energy transition, the initial state does not have to be Raman active in the sense that it vibrates in the symmetric stretching mode. For a transition to become visible in the Raman frequency domain, it is thus only dependent on whether or not the transition involves a change of $\Delta\nu_1 = \pm\mathbb{N}_1$ (all natural numbers starting from 1) . Therefore, in this project all the possible transitions from the Rothman table that fulfill the selection criteria of $\Delta\nu_1$=1, $\Delta\nu_2$=0, $\Delta\nu_3$=0, Δl=0 and ΔJ=0, are considered from a total of 256 vibrational levels for which the constants are provided. Transitions with a $\Delta\nu_1$ higher than 1 are neglected in this work since these will not be observed in the spectral region around the CO_2 Q-branch (1200-1500cm^{-1}).

Lastly a couple of adjustments regarding the energy equation are discussed. Recalling eq. (1.9) from section 1.2 the rotational energy within a given vibrational level for a diatomic molecular species can be adjusted to:

$$E_{\nu J} = hcG_\nu + hcB_\nu J(J+1) - hcD_\nu J^2(J+1)^2 + hcH_\nu J^3(J+1)^3 \quad \text{[Joules]} \tag{1.13}$$

Equation (1.13) includes the same constants as in eq. (1.9) such as the rotational constant B and centrifugal constant D, while G again denotes the Raman shifted frequency from the ground level 00001 . However it adds H to the equation, which is a higher-order correction factor for the rotational energy. The G, B, D and H coefficients differ depending on what vibrational level is considered, hence the subscript ν. Inserting the rotational quantum numbers $J = 1,2,3,...$ in combination with the correct constants for the considered vibrational level (see table 1.2) makes it possible to determine the energy related to each rotational level, within one vibrational energy state.

The above described equation can readily be applied for molecules such as nitrogen (N_2), oxygen (O_2) or hydrogen (H_2) and is one of the equations most widely applied and presented in literature for building CARS models. Carbon dioxide however, is a linear triatomic molecule where a combination of the degenerate bending mode in the yz- and xz-plane (see fig. 1.8) can result in a rotation of the carbon molecule about the internuclear axis. This simultaneous bending in both planes, results in a rotational motion that adds vibrational angular momentum with quantum number l, which must be considered in the energy equation [3, 11]:

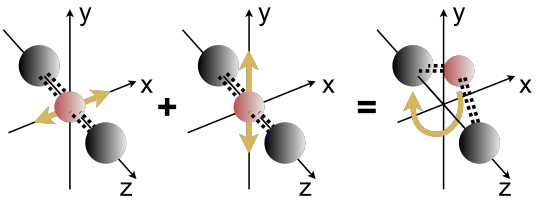

Figure 1.8: Simultaneous xz- and yz-bending resulting in a rotational motion about the z-axis, introducing a vibrational angular momentum component.

$$E_J = hcG_\nu + hcB_\nu[J(J+1) - l^2] - hcD_\nu[J(J+1) - l^2]^2 + hcH_\nu[J(J+1) - l^2]^3 \quad \text{[Joules]} \tag{1.14}$$

Table 1.2: List of the first 6 CO_2 vibrational levels related to Raman transitions used in this work for the calculation of the CO_2 Q-branch and hotband transitions, with e/f denoting the degenerate bending mode. Complete Rothman table with vibrational energy levels can be viewed in reference [7].

Vibrational level	Constants [cm^{-1}]			
$\nu_1\nu_2 l\nu_3 r$	G_ν	B_ν	D_ν	H_ν
00001	0	0.39021889	1.33338e-7	7.7e-15
01101e	667.37996	0.39063900	1.35295e-7	0.099e-13
01101f	667.37996	0.39125465	1.36088e-7	0.149e-13
10002	1285.4087	0.39048155	1.56973e-7	2.196e-13
10001	1388.1847	0.39018823	1.14801e-7	1.846e-13
11102e	1932.47013	0.39074498	1.49447e-7	1.005e-13
11102f	1932.47013	0.39169032	1.56357e-7	1.163e-13
11101e	2076.85588	0.39040962	1.25853e-7	0.906e-13
11101f	2076.85588	0.39133390	1.21099e-7	0.451e-13

2

CO_2-O_2 code description

The previous chapter detailed the theoretical concepts concerning CARS, this chapter covers the structure of the code that models the CARS phenomena. Section 2.1 begins by introducing the third order susceptibility, along with the equations of important constants and parameters. This is followed by section 2.2, which is dedicated to explaining the importance of the linewidth Γ and the models that are used to predict the linewidths for the considered transitions. In section 2.3 a short discussion regarding the changes in the code when moving from CARS to coherent Stokes Raman scattering (CSRS) is included. Lastly, section 2.5 describes the fitting routine and how it is used to determine temperature and concentration.

2.1. Third order susceptibility and relevant coefficients

A good starting point for explaining the model is the third order susceptibility. In order to understand what the third order susceptibility means from a theoretical perspective, it is worthwhile to have a look at the third order polarization [2, 12, 13]. The third order polarization captures the macroscopic behavior of a medium that is composed of a multitude of molecules undergoing the CARS processes on a microscopic level, which are described in the previous chapter. Using Equation 2 from reference [12] the third order polarization without the non resonant term is given by:

$$\begin{aligned} P^{(3)}_{\mathrm{Res}}(t,\tau_{23}) = \left(\frac{i}{\hbar}\right)^3 \int_0^\infty dt_3 \int_0^\infty dt_2 \int_0^\infty dt_1 \Big[\chi^{(3)}(t_3,t_2,t_1)\, E_3(t-t_3) \\ \times E_2^*(t+\tau_{23}-t_3-t_2)\, E_1(t+\tau_{23}-t_3-t_2-t_1)\, e^{i(\omega_1-\omega_2+\omega_3)t_3}\, e^{i(\omega_1-\omega_2)t_2}\, e^{i\omega_1 t_1} \Big] \end{aligned} \tag{2.1}$$

Here $\hbar = \frac{h}{2\pi}$ (h - Planck constant) simply known as h-bar, χ is the molecular response function. The electric field envelopes for the pump, Stokes and probe beam are given by E_1, E_2 and E_3 respectively. Their respective carrier frequencies are given by ω_1, ω_2 and ω_3 with coherence time scales t_1, t_2 and t_3. Since the individual pump, Stokes, probe and CARS pulses do not correspond to any resonant transitions, one can assume that the electronic response is fast compared to the variations in pump and Stokes pulses while integrating over t_1 , and the probe and CARS pulse while integrating over t_3. Thus, $\chi(t_3,t_2,t_1)$ can be rewritten as $\delta(t_3)\chi^{(3)}(t_2)\delta(t_1)$ and eq. (2.1) can be simplified to:

$$\begin{aligned} P^{(3)}_{\mathrm{Res}}(t,\tau_{23}) = \left(\frac{i}{\hbar}\right)^3 E_3(t) \int_0^\infty dt_2 \Big[\chi^{(3)}(t_2)\, E_2^*(t+\tau_{23}-t_2) \\ \times E_1(t+\tau_{23}-t_2)\, e^{i(\omega_1-\omega_2)t_2} \Big] \end{aligned} \tag{2.2}$$

In order to describe the molecular response of a molecule a phenomenological model is used giving every n to m transition in energy level a specific frequency $\omega_{n\to m}$ already described in eq. (1.10). The basis for modelling this molecular response or alternatively the third order susceptibility, represents the tendency of a medium on a macroscopic scale to generate an instantaneous electric dipole, in response to an external electric field. For the modelling of the CO_2 CARS spectrum, the pure rotational O- and S-branch is given by various different references [14, 15, 16, 17, 18] and can be described by the following equation:

$$\chi^{(3)} = \sum_k \sum_v \sum_{\Delta J=\pm 2} X_k \frac{4}{45} \gamma^2_{v,k} F^{(k)}_{\gamma} b_{J\to J+\Delta J} \left(\rho^{(k)}_{v,J+\Delta J} - \rho^{(k)}_{v,J}\right) exp\left[(i\omega^{(k)}_{v,J\to J+\Delta J} - \Gamma^{(k)}_{v,J\to J+\Delta J})\, t\right] \tag{2.3}$$

In this equation k denotes the species, v the vibrational quantum level and J the rotational quantum level. X is the species mole fraction and γ the polarization anisotropy. F is the corresponding Herman-Wallis factor and b is the Placzek-Teller coefficient while ρ denotes the Boltzmann distribution. All of which are described in the subsequent paragraphs. Finally, ω is the corresponding Raman frequency and Γ the linewidths which will be discussed in more detail in section 2.2 . For the ro-vibrational Q-branch a slightly different equation is applied that also includes the isotropic polarizability a [16, 19, 20], which is not the case for O- and S-branches:

$$\chi^{(3)} = \sum_k \sum_{\Delta v=+1} \sum_J X_k (v+1) \left[a^2_{v,k} F^{(k)}_{a_J} + \frac{4}{45} \gamma^2_{v,k} F^{(k)}_{\gamma_J} b_{J\to J}\right] \left(\rho^{(k)}_{v\to v+\Delta v,J} - \rho^{(k)}_{v,J}\right) exp\left[(i\omega^{(k)}_{v+\Delta v,J} - \Gamma^{(k)}_{v\to v+\Delta v,J})\, t\right] \tag{2.4}$$

The *isotropic* and *anisotropic* polarizabilty differs depending on the transition and type of molecule considered. For oxygen work published by Buldakov et al. (2003) [20] provides equations both for computing isotropic and anisotropic polarizabilities given by the equation:

$$\langle v|a|v+1\rangle_{O_2} = [[(v+1)/2]^{1/2} (2B_e/\omega_e)^{1/2} \times [1.779(71) + 0.019(12)\, v] \tag{2.5}$$

$$\langle v|\gamma|v+1\rangle_{O_2} = [[(v+1)/2]^{1/2} (2B_e/\omega_e)^{1/2} \times [3.25(26) + 0.057(19)\, v] \tag{2.6}$$

Here B_e is the rotational constant at equilibrium position, ω_e is the frequency at ground state equilibrium conditions and v is the vibrational quantum number. It should be noted, that eq. (2.5) and eq. (2.6), already include the (v+1) term from eq. (2.4) and should thus be left out in one of the two equations, before simulating the molecular response. These equations in combination with the constants from Rouillé et al. (1992) [21] make it possible to model the oxygen ro-vibrational O-, S- and Q-branch related to $v_0 \to v_1$ transition, but also the oxygen Q-branch hotbands related to the $v_1 \to v_2$ and $v_2 \to v_3$ transitions. For CO_2 however, a different approach is applied based on work conducted by Tejeda et al. (1995) [22] which looks at some of the transitions related to the CO_2 Q-branch Fermi peaks and gives their corresponding isotropic polarizabilities. In this M.Sc. thesis work the provided isotropic polarizabilties for the peaks at 1388cm^{-1}, 1285cm^{-1}, 1409cm^{-1} and 1265cm^{-1} are used from Tejeda and coworkers. For the isotropic polarizabilities of all the other transitions, the polarizability of the red fundamental Q-branch peak (1285cm^{-1}) is used if $\Delta\omega$<1300cm^{-1} and the polarizability of the blue fundamental Q-branch peak (1388cm^{-1}) is used if $\Delta\omega$>1350cm^{-1}. This is similar to what is applied in the work of Vestin and coworkers (2008) [17], where the polarizability was approximated to be the same for each vibrational state. Since the transitions of interest for the CO_2 analysis only concern Q-branch transitions, the anisotropic polarizability is ignored for simplicity. This can be justified for the following reasons. For one, as stated by Gu et al. [23] the depolarization ratio ($\frac{\gamma}{a}$) for CO_2 is very small (0.027), i.e. Q-branch transitions, where $\Delta J = 0$, are dominant. As such, γ is much smaller than a and considering that in eq. (2.4) both polarizabilties are squared this makes the difference between the isotropic and anisotropic terms even larger. Additionally, when looking at eq. (2.4) γ is preceded by the factor $\frac{4}{45}$, diminishing the influence of the anisotropic term further.

The Herman-Wallis (HW) factor accounts for the ro-vibrational coupling of molecules. It includes the effects on the rotational line strength of the interaction between vibrational and rotational modes and represents an important source of perturbation of molecular motion. A number of different versions of the HW factor have been available for years, generally being used for both S- and Q-branch spectrum calculations [14, 24, 12]. Some of the most used HW factors are the ones presented by James and Klemperer (JK), Martinsson, Tipping and Ogilvie (TO), and Buldakov (B)[24]. In this work the HW factor proposed by Tipping and Ogilvie is used [24]:

$$F_{TO} = \left[1 + \kappa^2 \left(\frac{p_1}{p_0}\right)(J^2 + 3J + 3)\right]^2 \tag{2.7}$$

Here B_e and ω_e are the equilibrium rotation constant and vibrational frequency respectively, for the specific species k, while J again represents the rotational level and $\frac{p_1}{p_0}$ indicate the ratio between the first two coefficients of the anisotropic expansion. An interesting study by Marrocco (2009) [19], reveals some physical inconsistencies regarding the HW factor. These physical inconsistencies can mainly be attributed to the fact that earlier versions of the HW factor like JK and TO leave out the isotropic polarizability component,

making it identical to the anisotropic polarizability $F_a(J)$=$F_\gamma(J)$. The proposed new approach from Marrocco suggests to use the anisotropic polarizability expansion coefficient when looking at purely rotational O- or S-branch spectra, and a combination of both anisotropic and isotropic polarizability expansion coefficient when looking at ro-vibrational spectra. In fig. 2.2 a considerable difference is observed depending on whether the anisotropic and isotropic polarizability expansion coefficient is used. The lighter the molecule, the greater the effect becomes, while the opposite is true the heavier the molecule is. In the same figure it can also clearly be seen that heavier molecules have a lower rotation-vibration interaction, to such a point that for CO_2 the effect becomes almost negligible, while it remains important to include for O_2.

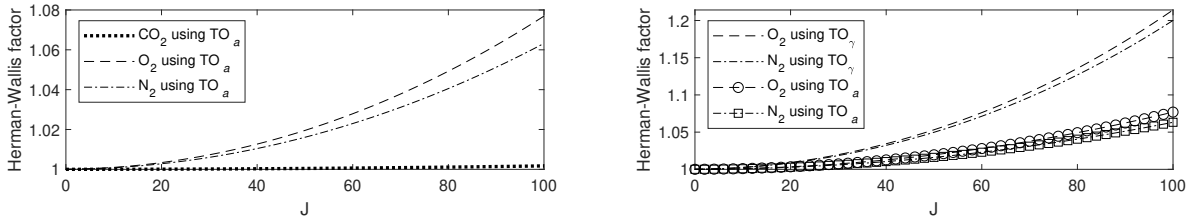

Figure 2.1: *Left graph*: Comparison between the isotropic (a) HW-factors of N_2, O_2 and CO_2. *Right graph*: Observed difference in HW-factor when using the anisotropic (γ) polarizability expansion coefficient. Generally, the heavier the molecule, the lower the vibration-rotation interaction.

The Placzek-Teller coefficients quantify the probability of a single molecule to be excited to a certain Raman shift by a given pump/Stokes photon pair due to the coupling of angular momenta between the rotating nuclei and electron cloud. The detailed physics behind this coupling are not discussed here, but are thoroughly covered in the work of Placzek and Teller (1933) [25] and Eckbreth (1996) [3]. The coefficients are given for the S-, O- and Q-branch and denote the $\Delta J = +2$, $\Delta J = -2$ and $\Delta J = 0$ rotational jumps respectively. Together they fulfill the existence condition adding up to 1 for any J-level. The respective equations for the Q-, S- and O-branch are given by eq. (2.8) to eq. (2.10) [3].

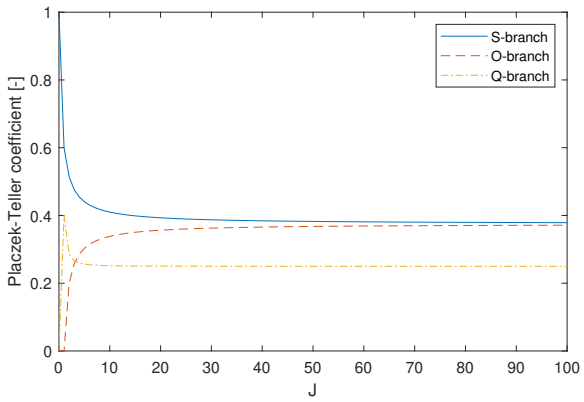

$$b_{J,J} = \frac{J(J+1)}{(2J-1)(2J+3)}, \quad \text{Q-Branch} \tag{2.8}$$

$$b_{J,J+2} = \frac{3(J+1)(J+2)}{2(2J+1)(2J+3)}, \quad \text{S-Branch} \tag{2.9}$$

$$b_{J,J-2} = \frac{3J(J-1)}{2(2J+1)(2J-1)}, \quad \text{O-Branch} \tag{2.10}$$

Figure 2.2: Placzek-Teller coefficients for J values up to 100.

While the previous equations can readily be applied for oxygen, if the Placzek-Teller coefficients for the CO_2 Q-branch are to be determined, the vibrational component of the angular momentum (quantified by the quantum number l) should be taken into consideration. Following the treatment given for symmetric-top molecules in reference [11], taking $\Delta K = \Delta l = 0$ and $\Delta J = 0$ the equation for the Placzek-Teller coefficients of the CO_2 Q-branch becomes:

$$b_{J,J} = \frac{[J(J+1) - 3l^3]^2}{J(J+1)(2J-1)(2J+3)}, \quad \text{Q-Branch} \tag{2.11}$$

Taking l=0 reduces eq. (2.11) to eq. (2.8).

The Boltzmann distribution, gives the probability of a molecule to be in a certain ro-vibrational energy state for a specified temperature. For a statistical ensemble it predicts how many molecules of a selected species populate a certain energy state. The higher the temperature of the probed medium, the more molecules will populate higher energy states. Essentially, the Boltzmann population distribution is what makes it possible to perform temperature measurements. The fraction of a total population in a given state m is given by:

$$\rho_m = \frac{N_m}{N_{tot}} = \frac{g_J g_m \exp\left[\frac{-E_m}{k_B T}\right]}{Z(T)} \tag{2.12}$$

Where the partition function Z(T) is given as,

$$Z(T) = \sum_m g_m \exp\left[\frac{-E_m}{k_B T}\right] \tag{2.13}$$

here g_m is the degeneracy of each rotational state (J), equal to (2J+1), while g_J denotes the spin degeneracy. E_m is the energy associated with a given energy level according to eq. (1.13) and eq. (1.14), depending on which molecule is considered. k_B is the Boltzmann constant, and Z(T) is the partition function, serving as a normalizing factor. In eq. (2.3) and eq. (2.4) the *Boltzmann population difference*, denoted as $\Delta\rho = \rho^{(k)}_{v\rightarrow v+\Delta v,J} - \rho^{(k)}_{v,J}$, adds to the probability for a molecule to undergo a certain energy transition.

The statistical weight of g_J, can differ depending on which vibrational state is considered. For oxygen a weight of 0 is given for even and 1 for odd rotational quantum numbers for Σ_g-symmetries. For CO_2 the pure rotational S-branch 00001 and the blue 10001 and red 10002 Q-branches, have the same degeneracies for even and odd rotational J numbers, being equal to 1 for even J numbers and equal to 0 for odd J numbers [26]. Nevertheless, this degeneracy factor can change for CO_2 to 1 for odd and 0 for even J-numbers depending on the symmetry of the vibrational level considered. Based on the schemes given in reference [26], table 2.1 gives an overview of the degeneracies of the vibrational level, depending on their symmetry. The symmetry of the vibrational levels higher than the ones already depicted in fig. 1.7 are determined using the rules shown in table 2.2 by looking at their combination of vibrational modes. For example, in order to determine the symmetry of 11^10, one can consider it as a combination of the first vibrational level of the symmetric stretch (10^00) and the first vibrational level of the degenerate bending mode (01^10), having a Σ_g- and Π_g-symmetry respectively. Looking at table 2.2 this gives a symmetry of Π_g . All degeneracies other than Σ are also treated as Π symmetries in the tables for determining the spin degeneracy.

Table 2.1: The degeneracies depending on symmetry for CO_2 based on the schemes provided by reference [26].

Symmetry		Σ_g	Σ_u	Π_g	Π_u
g_J	even J	1	0	0/1 - f/e	1/0 - f/e
	odd J	0	1	1/0 - f/e	0/1 - f/e

Note: Π *stands for all symmetries other than* Σ *and f/e denotes the level of the degenerate bending mode according to the HITRAN notation.*

Table 2.2: The resulting symmetries depending on the vibrational level combinations.

Symmetry	Σ_g	Σ_u	Π_g	Π_u
Σ_g	Σ_g	Σ_u	Π_g	Π_u
Σ_u	Σ_u	Σ_g	Π_u	Π_g
Π_g	Π_g	Π_u	Π_g	Π_u
Π_u	Π_u	Π_g	Π_u	Π_g

A distinction is made between rotational and vibrational thermometry. Looking at the left graph in fig. 2.3 the higher the temperature, the more vibrational levels are occupied. Similarly for the rotational levels in the right graph, the higher the temperature the more rotational states are occupied with the distribution peak becoming lower and spreading as proportionately less molecules occupy the corresponding vibrational level. Looking at the right graph for the rotational distribution one can see that the difference between the curve at T=300K and T=900K is more pronounced than the difference between T=900K and T=1500K. As the temperature increases it thus becomes increasingly difficult to differentiate between temperatures. The latter is why rotational thermometry is generally regarded as more suitable for low temperature applications, since it can lack in precision for high temperature studies [27, 28]. The opposite is true for vibrational thermometry, since at low temperatures the population of the vibrational levels above 01101e/f is nearly 0 below temperatures of 600K. Nonetheless, the higher the temperature, the more relevant it becomes to look at higher Raman shifts corresponding to vibrational transitions.

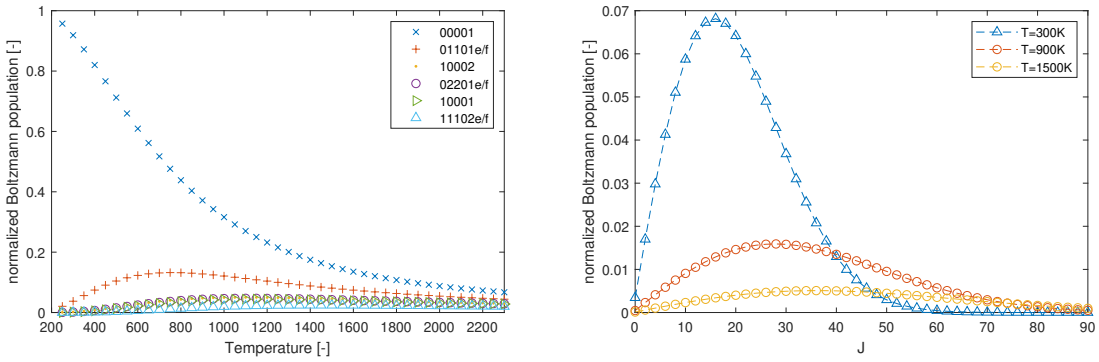

(a) Vibrational population for first 6 v-levels.

(b) Rotational population for 00001.

Figure 2.3: Left graph: Fractional population of the first 6 vibrational states of CO_2 . Right graph: Fractional population for CO_2 rotational levels up to 90 for the ground state (00001) at three different temperatures.

2.2. Linewidth, probe parameters and linewidth model

In spectroscopic applications, what is often observed in practice is that the linewidths of the resonant peaks in the frequency domain of the obtained signal differ depending on pressure and temperature [29, 18]. In a simplistic sense the linewidth Γ can be seen as an energy dispersion term. It embodies the dispersion of energy occurring through two pathways: the collisions of molecules and frequency shifts of the scattered photons that arise due to the Doppler effect [30]. Frequencies from scattered photons coming from molecules that move away from the detector are negatively Doppler shifted, while the opposite is true for photons moving towards the detector. This makes the Doppler contribution to the linewidths dependent on the translational motion of the molecules, which correlates to temperature. The collisional broadening originates from the inelastic energy transfer that occurs when two molecules collide. The smaller the average distance a molecule needs to travel before it hits another one, the higher the collisional linewidth contribution. This contribution is scaled with pressure since higher pressures relate to a higher number of molecules in a given medium, increasing the likelihood for collisions to occur [16].

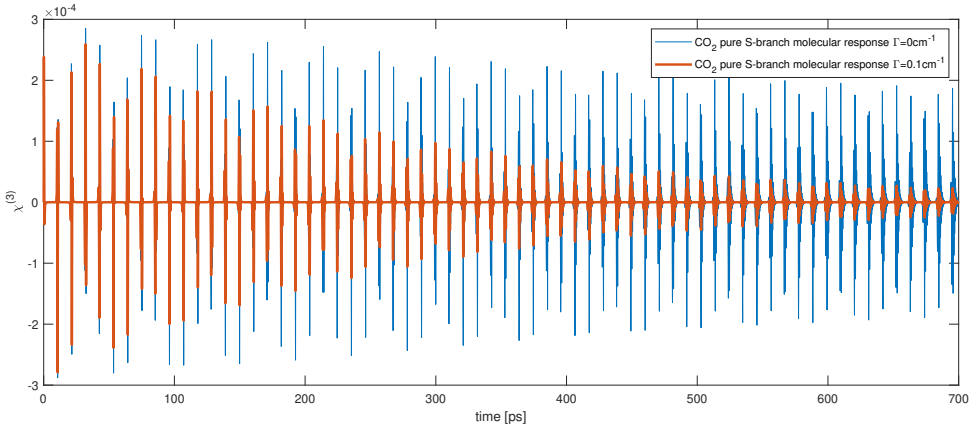

Figure 2.4: The effect of including the linewidth to the molecular response function, leading to an accelerated decay of the molecular response in time based on the CO_2 spectral model developed in this work, given for T=300K.

The effect of Γ is not only noticeable in the frequency domain, but can also be discerned in the time domain. Looking more closely at eq. (2.3) one can draw a comparison to eq. (1.11), using complex numbers describing a wave by its imaginary component ω and real component Γ propagating in time. An analogy can be drawn to classical mechanics, relating to the decay of an oscillation in time. Similarly Γ acts as a damping coefficient that leads to the decay of the molecular response in the temporal domain. The effect of Γ on the molecular response is represented in fig. 2.4 using a constant linewidth for all J-states of 0.1cm^{-1}

at full width at half maximum (FWHM). Without damping (Γ=0cm^{-1}), the amplitude of the oscillations has barely decreased by 10% at 220ps, while the amplitude of the response including the linewidth (Γ=0.1cm^{-1}) has more than halved.

Consequently, this means that the signal strength is dependent on time, making the *probe delay (τ)* an influential parameter. The probe acts as a 'scan' of a portion of the molecular response in time, visualized in fig. 2.5 . A longer *probe duration (Δt)* leads to a larger probed section of the molecular response. Hence, when increasing Δt the decay of the signal over the probe duration becomes a more significant factor leading to increased line broadening. If the probe is too short however, the probed section will not contain sufficient information to perform a frequency analysis of the oscillations. In the spectral domain this results in a convolution of the spectral lines, merging them together. The picosecond probe pulse durations related to the two beam method applied in this work (section 1.3) strikes a good balance between keeping enough spectral resolution for analysis, while minimizing the line broadening effects and keeping a refined temporal resolution. The minimum temporal and spectral resolution is dictated by what is called the time-bandwidth product ($\Delta t \Delta f$>cst), which has to be above a minimum value depending on the shape of the pulse. Recall that the collisional effects leading to line broadening are small for a ps-duration probe, using this two beam technique because it allows to operate on a faster time-scale than the molecular collisions. Even though this is the case, it remains important in considering the decay of the molecular responses in the time domain. The reason being that the relative intensity of the peaks in the spectral domain changes with time, and thus changes with probe delay. The latter becomes especially important for vibrational thermometry in multi-species environments, where the linewidth differs depending on what molecular species are present in the probed medium. The reason behind this relates to the "ease" with which a molecule can transfer energy to another upon collision. The more the energy "ladders" (see fig. 1.2) of the colliders correspond to one another and the smaller the spacing between its energy states, the more likely it becomes that an energy transfer occurs leading to the dispersion of energy. Two identical molecules are thus more likely to exchange energy than two distinct ones. A gas consisting of 100% CO_2 will generally have a higher linewidth for CO_2, than a gas consisting of 50% CO_2 and 50% N_2. Therefore, in a gas mixture the distinction is made between self-broadened (e.g. CO_2-CO_2) linewidths and broadening due to other perturbers (e.g. CO_2-N_2, carbon dioxide perturbed by nitrogen). Since this M.Sc. work deals with reactive multispecies environments, it is important to consider the linewidth contributions of the major species such as nitrogen and oxygen.

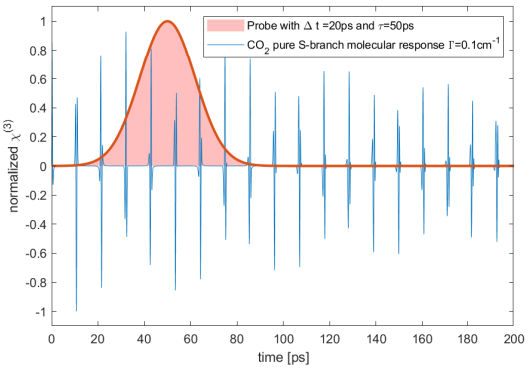

Figure 2.5: Probe plotted over molecular response, with a delay of 50ps and a duration of 20ps (FWHM).

Many works have been dedicated to the determination of linewidths and models that mimic their impact [7, 27, 31]. If the probe duration is short enough, one option is to measure the decay of the molecular response using different probe delays and deduce the linewidth. The other option is to use values generated from a linewidth model. Two widely applied models are the modified exponential energy gap (MEG) model and energy corrected sudden scaling law (ECS). Both are based on fitting laws to compute linewidths and can be used for multispecies environments. Alternative approaches, like the one from Rosenmann et al. (1988) [31] use polynomial fits based on experimental spectra to predict the linewidth. The work presented in this document, relies on a polynomial approach to determine the CO_2 linewidths and a MEG model to give the values for the linewidths for O_2. The polynomial approach is based on the work of Rosenmann et al. (1988) [31], while the MEG model is based on the model described in the work of Rahn and Palmer (1986) [32]. The method applied by Rosenmann et al., uses an analytical law described by:

$$\Gamma_{JJ}(T) = \Gamma_{JJ}(300K)\left[300/T\right]^{N_{JJ}} \tag{2.14}$$

where $\Gamma_{JJ}(300K)$ is the linewidth of the spectral line corresponding to the rotational state J and N_{JJ} is the exponent at a reference temperature of 300K. They are determined from a least square fit and are described by a simple second degree polynomial:

$$\Gamma_{JJ}(300K) = a_2 J^2 + a_1 J + a_0 \tag{2.15}$$

$$N_{JJ} = b_2 J^2 + b_1 J + b_0 \tag{2.16}$$

using this approach used by Rosenmann, linewidths for CO_2-CO_2, CO_2-N_2 and CO_2-O_2 can be determined. The constants used can be found in appendix A . In order to compute the combined linewidth for CO_2 in a gaseous mixture, Rosenmann proposes the following relation:

$$\Gamma_{JJ}(T)(CO_2 - mixture) = \sum_x x_X \Gamma_{JJ}(T)(CO_2 - X) \tag{2.17}$$

where x_X and Γ_{JJ} are the mole fractions of species X and the broadening coefficients of species X respectively. One important thing to note is that the Rosenmann approach is only advised to work for J<101, in the later discussion its possible extension to J=120 or even 140 are evaluated. While the application of these equations is relatively straightforward, the MEG model is slightly more elaborate. The MEG model is a scaling law, that is calculated through the energy gaps between the various rotational levels of a vibrational level. For a given vibrational level, the upward rate of transitions from J to J' for the MEG model can be determined using the following equation:

$$-\mathrm{Re}(W_{JJ'}) = \alpha \left(\frac{T}{T_0}\right)^{-N} \left(\frac{1 + aE_J/kT\delta}{1 + aE_J/kT}\right)^2 \times \exp\left(-\beta E_{J'J}/kT\right) \tag{2.18}$$

Giving a matrix of the form:

$$W_{JJ'} = \begin{bmatrix} 0 & W_{J_1 \to J_2} & W_{J_1 \to J_3} & W_{J_1 \to J_4} & \dots & W_{J_1 \to J_n} \\ 0 & 0 & W_{J_2 \to J_3} & W_{J_2 \to J_4} & \dots & W_{J_2 \to J_n} \\ \dots & \dots & \dots & \dots & \dots & \dots \\ \dots & \dots & \dots & \dots & \dots & W_{J_{n-1} \to J_n} \\ 0 & \dots & \dots & \dots & \dots & 0 \end{bmatrix} \tag{2.19}$$

here α, N, δ and β are the species specific temperature independent parameters given in table A.3 . T_0 is a reference temperature (in this work taken to be 295K) and $E_{J'J} = |E_{J'} - E_J|$ is the energy gap between the J-states. The downward transition rate $W_{J'J}$ is determined using the detailed balance principle according to the equation:

$$W_{J'J} = \frac{(2J+1)}{(2J'+1)} W_{JJ'} \times \exp\left(E_{J'J}/(kT)\right) \tag{2.20}$$

Based on these equations the linewidth Γ_{JJ} can be determined for half width at half maximum (HWHM) according to:

$$\Gamma_{JJ} = -\sum_{J' \neq J} \mathrm{Re}(W_{JJ'}) \tag{2.21}$$

The latter procedure provides the self-broadened linewidths for the various vibrational levels of the considered molecule. To calculate the linewidths related to the various types of transitions, an approach is used that has also been applied by Martinsson et al. (1993) [27] on nitrogen and Lavorel et. al (1990) [33] on the v1/2v2 Fermi dyad of CO_2, where they state that the linewidths of the ground level do not differ much from their corresponding linewidth of the Q-branches. This justifies the use of Γ_{JJ} for all $\Delta v = \pm 1, \Delta J = 0$ transitions. For S- and O-branch transitions for the approximate sum rule can be applied, here given for a transition of $\Delta v = 0$, with $\Delta J = +2$:

$$\Gamma^v_{J,J+2} \approx \frac{1}{2}\left(\Gamma^v_{JJ} + \Gamma^v_{J+2,J+2}\right) \tag{2.22}$$

Following reference [33] this means that the same values can be used for the Q-branch as the ones calculated for the ground level, thus they only need to be computed once for each temperature, saving computing time. Implementing the described methods in *Matlab*® makes it possible to get values for the linewidths, which can be used to compare to experimental ones and essentially incorporated into the spectral code. Figure 2.6 shows the linewidths for CO_2 broadened by itself, oxygen, nitrogen and values of a simulation based on experimental data by Rosenmann et al., while fig. 2.7 shows the linewidth for three different temperatures.

The figures reveal a couple of noteworthy points. One important point is that higher temperatures lead to lower linewidths, which can be explained by a lower density leading to fewer collisions. Thus the higher the temperature, the slower the decay of the molecular response in the time domain. Furthermore, the change in linewidth for both CO_2 and O_2 is much more noticeable from 300K to 1200K than from 1200K to 2100K. Indicating that the linewidth is more sensitive to temperature changes at low temperatures than high temperatures. Another point to note, is that higher temperatures also lead to a nearly constant linewidth for the rotational levels. Additionally, for J-numbers above 80 the linewidth trend "flattens", also at lower temperatures. For this reason, it could be argued that from J=100 onwards the linewdith can be regarded as constant, making the Rosenmann method also applicable to J values above 101. Looking at fig. 2.3b, for temperatures below 1500K, J-levels above 90 are scarcely populated, making their influence on the molecular response small. At temperatures above 2000K however, J-levels up to 120 can still be of influence and for higher flame temperatures even up to 140. Nonetheless, since the linewidth can be considered nearly constant at these temperatures, it should be safe to assume that $\Gamma_{J=101} \approx \Gamma_{J=102} ... \approx \Gamma_{J=140}$. This assumption essentially makes it possible to extend the method to higher J-levels, without diverging significantly from the real values.

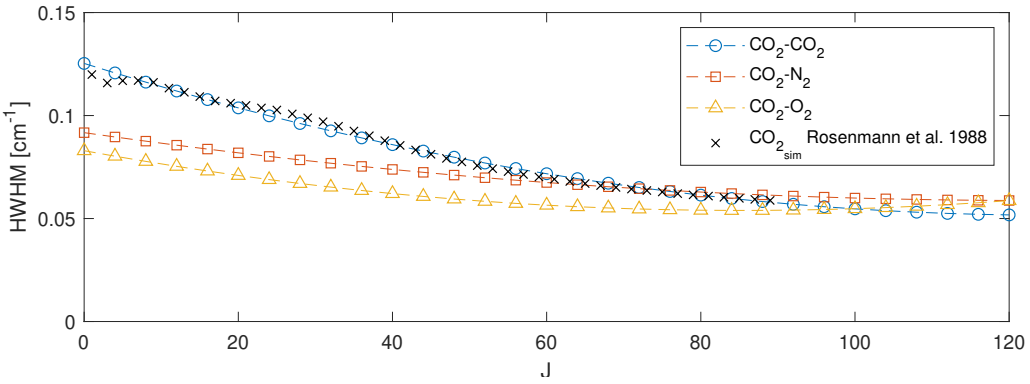

Figure 2.6: The Rosenmann predictions for CO_2 linewidths, perturbed by CO_2, by N_2 and O_2, given in halfwidth at half maximum (HWHM) up to J=120. The experimental data is obtained from Rosenmann et al. 1998[31].

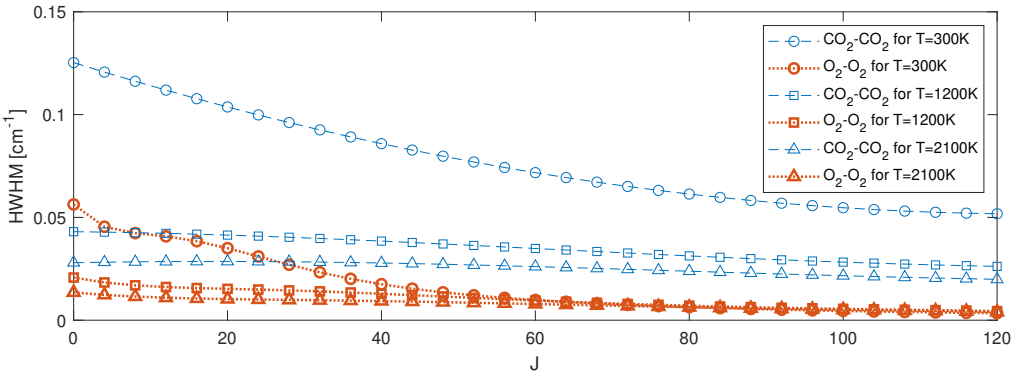

Figure 2.7: The Rosenmann predictions for CO_2 self broadened linewidths for different temperatures of 300K, 1200K and 2100K, given in halfwidth at half maximum up to J=120.

2.3. Coherent Stokes Raman Scattering

Coherent Anti-Stokes Raman scattering, is the most widely adapted term when addressing the practical applications of the theoretical concepts discussed up until now. Nonetheless, it is important not to forget that a similar "mirrored" spectrum to the CARS spectrum occurs on the Stokes side, resulting from coherent Stokes Raman scattering (CSRS). When talking about applications of Raman scattering in spectroscopy, CSRS is referred to much less frequently in literature as its counterpart. Except for the frequency shifts being exactly opposite, it is assumed in this work that not much changes when switching from one to the other. However, a couple of changes adapted in this work need to be noted when moving from CARS to CSRS regarding the spectral model, also described in reference [11].

Importantly, the underlying theory for either CARS or CSRS does not change. However, in order to switch between the two, using the model described in the previous sections, a couple of adjustments need to be made. One adjustment lies in changing the $(v+1)$ factor that includes the vibrational quantum number to simply v in eq. (2.4), which depends on the initial state of the transition. The transition frequencies will also change, resulting in an equal but opposite shift with respect to the carrier frequency (probe beam frequency) as shown in fig. 2.8. Looking at the selection rules of O- and S-branches, they are switched on the CSRS side, with the lower shifts now corresponding to the S-branch. This means that a switch in the Placzek-Teller coefficient needs to be taken into account, when simulating the oxygen ro-vibrational O- and S-branches.

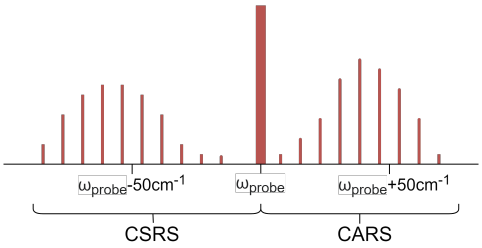

Figure 2.8: The CARS and CSRS side shown in the frequency domain.

2.4. Theoretical library

The procedure for performing temperature and concentration measurements requires a spectral library to fit to the experimental CARS spectra. This is accomplished by running the spectral code that simulates the molecular response given by eq. (2.3) and eq. (2.4), for a variety of temperatures T and relative concentration inputs $\frac{X_{O_2}}{X_{CO_2}}$ in the time domain. These molecular responses can then be translated to the frequency domain by performing a Fourier analysis, which generates the synthetic CARS spectra (seen in fig. 2.9) that can be fitted to the experimental ones.

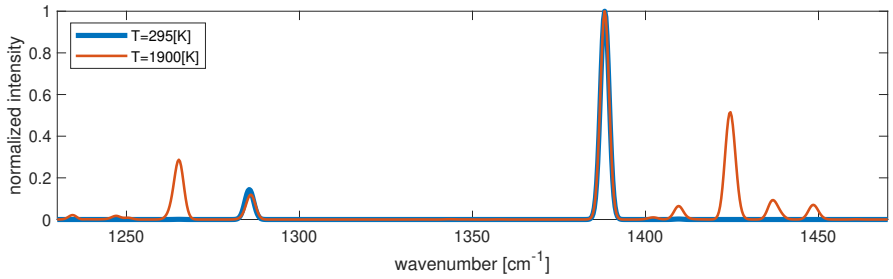

Figure 2.9: Simulated CARS spectra for 295K and 1900K , with a probe delay of 41ps and a probe duration of 4ps. The hotband peaks become clearly visible at higher temperatures where the higher vibrational levels are populated.

In order to compile a spectral library that is accurate enough, but not unnecessarily large, one needs to have an indication what temperatures and what concentrations are to be expected. The experiments are conducted under ambient conditions using a methane-air flame. In the atmosphere, air generally has a $O_2 - CO_2$ ratio of 500, considering that air contains roughly 20% oxygen and only 0.04% carbon dioxide. During the combustion process at an equivalence ratio of 1.0, meaning there is exactly enough oxygen to burn up all the fuel, the oxygen concentration is expected to drop to 0 under ideal conditions. Using $chem1d$, which is a one dimensional laminar flame code that provides temperature and molecular species concentrations within a flame, the progression of the relative $O_2 - CO_2$ concentration can be put into perspective.

The figures below show a strong concentration and temperature gradient across the flame front, with a thickness of roughly 0.5mm . After the flame front there is still a noticeable variation in temperature and

concentration. The former climbing up from about 1800K to 2100K after the flame front for ϕ=1.0 . Although the concentration of oxygen is not 0 right after the flame front it continues to decrease in both graphs, which is due to the continuation of the reactions at a decreased rate. It becomes apparent that the oxygen concentration does not seem to decrease to 0 for ϕ=1.0, which is due to the fact that not all the methane is directly converted to CO_2 and water vapour. Other by-products of the reaction use up the methane, leading to not all the oxygen reacting with the fuel. However, it becomes clear that for higher equivalence ratios where more fuel is available the oxygen concentration does indeed drop to 0. Hence, for this project it suffices to consider relative O_2-CO_2 ratios ranging from 0 to 500.

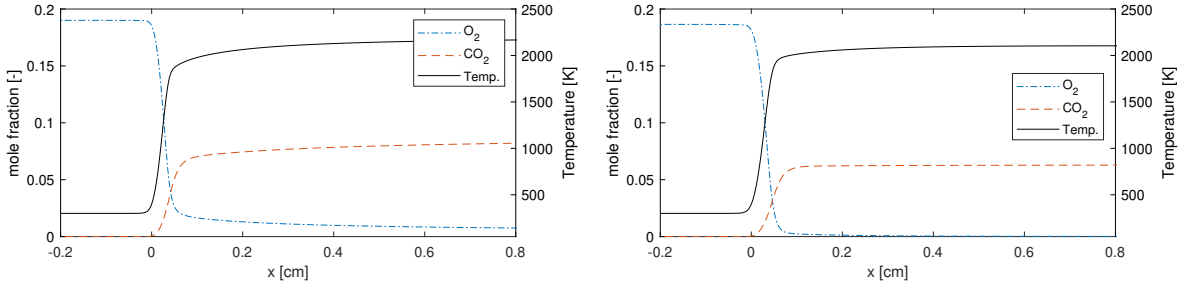

Figure 2.10: Variation of O_2 and CO_2 concentration and temperature across the flame front for ϕ=1.0 (left graph) and ϕ=1.2 (right graph), obtained from $chem1d$ combustion simulation software.

In terms of temperature it seems that a lower limit starting at T=250K is adequate since the experiments are conducted at room temperature and will certainly not drop lower during the combustion process. For the higher temperature limit it seems that a maximum temperature of about 2200K should suffice. However, the temperature does not level out at 0.75cm after the flame front in both graphs in fig. 2.10, which is why 2300K is considered as a higher limit to make sure any further increase in temperature is accounted for.

2.5. Fitting routine

Once the spectral library is generated an experimentally obtained spectrum can be matched to one of the spectra in the library, through a spectral fitting technique. The spectral fitting technique uses the sum of squares (SSQ) of the residuals in combination with a least square interpolating algorithm to find a minimum for the best match. The best match with the smallest residual will then set the temperature and concentration corresponding to the observed spectrum. Sum of squares (SSQ) of the residuals [18]:

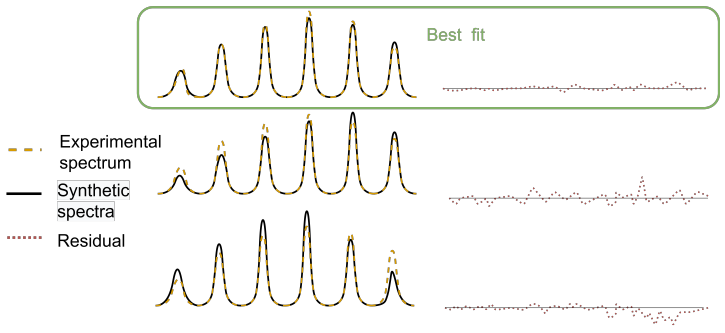

$$\mathrm{SSQ} = \sum_i \left(I_i^{\text{theoretical}} - I_i^{\text{experimental}} \right)^2 \quad (2.23)$$

Figure 2.11: Sketch of the fitting scheme selecting the best fit from the library, judged by the lowest residual.

The figure above gives a simplified sketch of how the fitting procedure is applied. Once the best fit is determined, the optimum temperature can be deduced. Using a *polynomial* interpolation scheme, the adjacent fits can be used to interpolate between them and find the minimum of the resulting curve. This minimum should then correspond to the optimum measured temperature. The same procedure is applied for the concentration measurements.

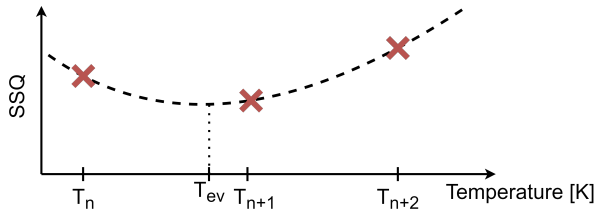

Figure 2.12: Polynomial interpolation scheme, using the values of the adjacent temperature fits in the library. The minimum of the resulting curve then sets the evaluated temperature value.

3

Experiments

The previous chapters covered the theory and describes how to convert the theory to model the molecular response of CO_2 and oxygen. The next, is to acquire the experimental data, which is what essentially links the theory to practice. This chapter begins with a thorough description of the CARS setup used in this M.Sc. project. This is followed by section 3.2 where the combustion experiment is described in more detail. Finally, section 3.3 describes the procedure concerning the data acquisition phase.

3.1. Laboratory setup

The CARS system used in the 'Ultrafast Laser Diagnostics Laboratory' at the Aerospace Engineering faculty of the TU Delft serves to perform studies in chemically reacting flows. The system combines many of the latest advancements for CARS thermometry discussed in the previous sections using a two-beam hybrid fs/ps-CARS setup.

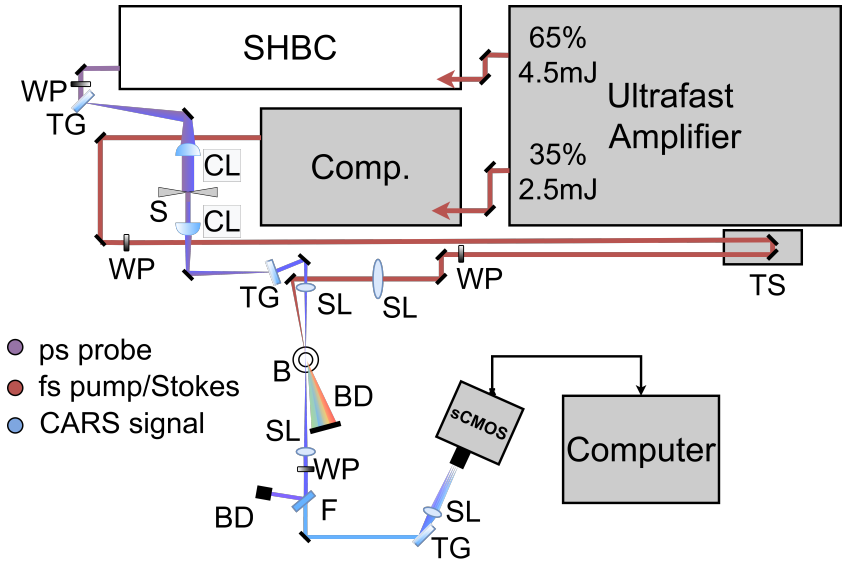

Figure 3.1: Ultrafast amplifier system, combined with SHBC (second-harmonic bandwidth compressor) and an external compressor, produces auto-synchronized fs pump/Stokes and ps probe pulses for space–time CARS diagnostics. A wide-field coherent imaging spectrometer equipped with a sCMOS camera is used for fast image acquisition. TG, transmission grating; S, slit; TS, translation stage; WP, half-wave plate; B, burner; BD, beam dump; F, bandpass filter; CL, cylindrical lens; SL, spherical lens.

Figure 3.3 shows a general layout of the base system for a point measurement setup. The system is mainly based on a single ultrafast regenerative amplifier system (7.5mJ, 1kHz, Astrella Coherent) that outputs two repetition-wise synchronized beams [34]. The two beams are obtained by splitting off a compressed main beam (65%, 4.5mJ/pulse) and an uncompressed beam, which is split off before the internal compressor

(35%, 2.5mJ/pulse). For the amplification of the pulses a chirped pulse amplification (CPA) scheme is applied, which involves the stretching, pumping and re-compressing of the pulses. The stretching of the pulse is achieved by passing the laser pulse through a stretcher, usually making use of a pair of gratings to disperse the light spectrum. This results in a pulse where the various light frequencies are spread over the pulse duration, with higher frequencies towards the trailing end of the pulse, the pulse is said to be chirped. After amplification of the pulse, it is re-compressed applying the same grating technique, to reverse the effect of the stretcher. The compressed beam is guided into a Second Harmonic Bandwidth Compressor (SHBC) unit to generate a narrowband ~4ps probe pulse, having a conversion efficiency of ~30% resulting in a 1.2mJ pulse. Meanwhile the uncompressed beam is sent to an external, coherent compressor, producing a near-transform-limited (NTL) ~35fs pump/Stokes pulse. Near-transform limited means that the time-bandwidth product is near its minimum value, maximizing the resolution in both time and frequency. The resulting pump/Stokes and the probe beam are at wavelengths 785-815nm and 400 nm respectively. This external compressor offers a convenient way for compensating (pre-chirping) of dispersion terms along the optical path. The difference in path length between the two-beams is compensated by an optical delay line, with relative arrival time being adjusted by an automatic translational stage (Thorlabs, sub-10fs resolution). In order to be able to tune the probe pulse instrument linewidth, a spatial 4-f filter is placed in the probe beam path, with two transmission gratings (~3040 1/mm, Ibsen Photonics), two cylindrical lenses with focal length of 300mm and one mechanical slit. The spherical lenses make it possible to perform point measurements by focussing both the pump/Stokes and probe beam on the measurement location for point measurement. The lens in the pump/Stokes path focuses the beam down to such an extent that it undergoes self-phase modulation, generating ultrabroadband light for ultrabroadband excitation of the CARS spectrum. Half wave plates (Eksma Optics) are inserted into the path to fulfill three goals. One being to satisfy the transmission axis of the gratings in the 4f-filter mounted on the probe beam path. Another purpose being to control the relative polarization of the pump/Stokes beam with respect to the probe beam. Lastly, they also serve to turn the polarization of the CARS beam to satisfy the transmission axis of the polarization beam splitter and the grating of the spectrometer. In order to avoid damage to the Andor Zyla 4.2 sCMOS (scientific Complementary Metal Oxide Semiconductor) camera, the powerful probe beam must be separated from the CARS beam. As the CARS and probe beam often overlap quite closely in a two-beam system a rejection through the angle-tuning of a band-pass filter is performed in this setup. The sCMOS camera has a maximum quantum efficiency (QE) of ≈82% , however at 400μm which is roughly the wavelength of the carrier frequency of the probe, QE drops to 40% .

In order to generate ultra-broadband light that allows the excitation of the CO_2 Q-branch, the system implements multicolored light generation. In this case ultra-broadband light is generated in air using a spherical lens that focuses the beam onto itself, leading to self-focusing. This self-focusing leads to the local ionization of the medium, starting in the center of the beam, where the intensity is the highest. This can lead to the creation of an under-dense plasma which decreases the local refraction index of the medium, leading to defocusing of the beam. If this focusing and defocusing happens in a re-occurring fashion a light filament is created. This process results in the temporal variation of the laser intensity, leading to a temporal variation of the refraction index according to $n = n_0 + n_2 I(r,t)$. This process in turn results in the appearance of new frequencies in the light spectrum of the laser pulse; self-phase modulation. Through filamentation it is possible to generate broadband light from a narrowband light source, which is termed "supercontinuum generation" . For the experiments conducted in this project a filament is created right before the pump/Stokes beam enters the flame, leading to ultra-broadband excitation (in-situ generation/in-situ use).

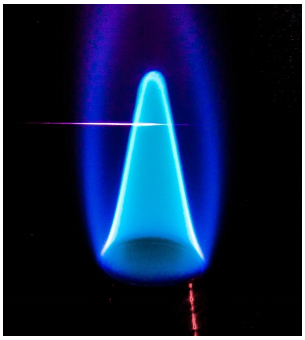

Figure 3.2: Image showing the light filament created in air for ultrabroadband excitation in a canonical flame.

3.2. Combustion experiment

The combustion experiment is conducted using a methane(CH_4)-air flame, with air containing roughly 20% oxygen, 79% nitrogen and 0.04% carbon dioxide. The air is pumped in from an external air tank to a pressure of 2bar, filtered and combined with methane in a mixing tube. The methane comes from a pressurized gas tank, where it is contained at 100bar and then reduced by gas regulators in two stages to about 2 bar, before it enters the mixing tube. Before both channels are combined however, a rotameter for each inlet sets the flow rate Q with which equivalence ratio can also be tuned as depicted in fig. 3.3. The mixing tube consists of two sections, the first stage is made out of a flexible material and is a couple of meters in length. Then the final stage is made of stainless steel with a length of 70cm, comprising the Bunsen burner (12mm diameter), where the gas is ignited upon exit. Considering the mixing length l_{mix} for the inner region of the turbulent boundary layer of a flat plate in eq. (3.1) [35]. Where taking the boundary layer thickness y equal to the radius of the mixing tube r=6mm, κ=0.4 [36], Y=26 [35] and y^+=60 [35], gives l_{mix}= 0.84mm, clearly leading to a well mixed gas upon ignition.

In total measurements on two different types of flames are performed: V-flame and M-flame. The shapes of the flames along with some import features are shown in fig. 3.5. The height of the flame and the gradient of the flame front changes with equivalence ratio and flow rate. Figure 3.4 shows how a canonical flame becomes elongated as the equivalence ratio is increased, where a balance between burning velocity and flow velocity defines the angle of the flame front. The closer the equivalence ratio is to 1.0, the higher the burning velocity and the higher the overall flow rate, the steeper the flame front.

$$(l_{mix})_{\text{inner-region}} \approx \kappa y \left[1 - exp(-y^+/Y)\right] \quad (3.1)$$

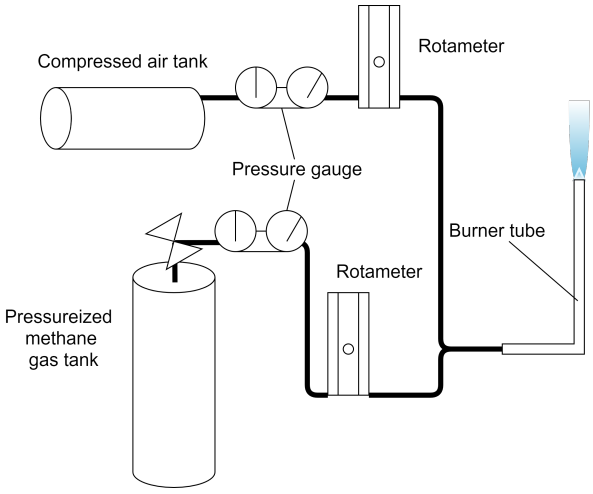

Figure 3.3: The burner setup for the methane-air combustion experiments, showing the flow path for each of the two gases before being ignited upon exit of the burner tube.

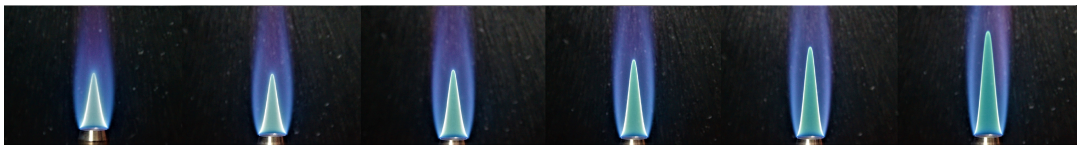

Figure 3.4: Canonical flame for equivalence ratios of $\phi \approx 1.1$ up to $\phi \approx 1.4$ (left to right). The flame is stretched as the flow of methane is increased leading to a steepening of the flame front due to an increase in flow velocity and decrease in burning velocity.

Keeping the previous points in mind the most elaborate experimental campaign is conducted on the M-shaped flame. The idea being that in order to perform an optimal "scan" of the flame, the scanning plane should be as perpendicular as possible to the flame front. With the resources at hand, this is thought to most easily be achieved by performing a horizontal scan starting from the outer flame front of an M-shaped flame. Due to the shape of the canonical flame, achieving a perpendicular scan to the flame front is a tedious task as it would involve both horizontal and vertical adjustments, careful monitoring of the flame and a precise estimation of the half-cone angle. The V-flame, is also precarious as a similar problem arises like the one described for the canonical flame. One of the difficulties, when operating with high temperature gaseous

flows in general, is the lower density giving a lower signal intensity. For this reason the crossing angle of the pump/Stokes and probe beam is kept relatively low to increase the interaction length. A negative influence of this however is that the round shape of the Bunsen burner leads to a rounded flame front. Thus, the temperature of the probed medium can vary, which can lead to inaccurate results. For this reason, a second experiment is performed on a V-flame, where inside the center of the V-valley a more homogeneous temperature can be observed for longer probe sections. The anchoring of the flame proved difficult however, becoming more prone to flashback as the mixture becomes richer. The first experiments to validate the model are conducted in air. One experiment is simply a measurement of the ambient conditions, with an expected temperature of about 293K and atmospheric conditions for the concentrations. The second air experiment is conducted at room temperature, with a person exhaling into the probe volume. This increases the CO_2 concentration roughly by a factor of 100 [37], decreases O_2 concentrations by a fifth and increases the temperature by about 14K ($\approx 34^{\circ}$C [38]). This way the model can be tested with respect to known temperatures and concentration, which is essential for the model validation.

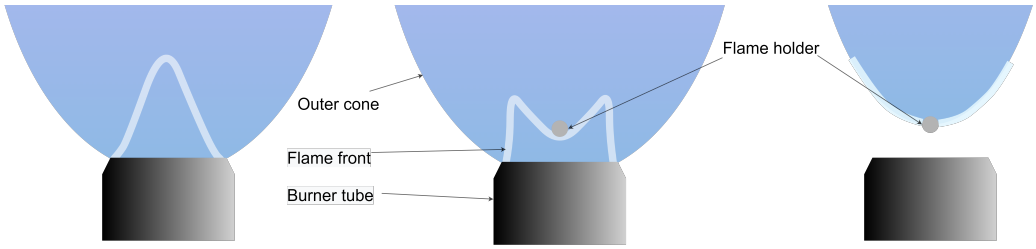

Figure 3.5: The two types of flames used in the experiments, consisting of a M-flame and a V-flame (middle to right) along with a canonical flame (left).

All in all, three experiments are performed. One horizontal scan of the M-flame to show the progression of O_2-CO_2 concentration from the flame front to just outside the flame. The second one is a measurement conducted at six different equivalence ratios in the product region of a V-flame and the last two are spectra obtained close to room temperature, probing a human breath upon exhalation and at ambient conditions.

3.3. Procedure

The experiment in the M-flame, included point measurements at 4 locations across the flame. The measurement locations of the M-shaped flame and the measurement location in the V-flame, are shown in fig. 3.6. For the M-flame, these locations are chosen because they are expected to give a progressive view of temperature and concentration from the reactant zone, across the outer cone to position 4 just outside the flame. Using reference [39] as guidance, it is expected that the temperature decreases from 1 to 2 and then drops to a considerably lower temperature between positions 2 and 3, as it mixes with the ambient air. It should be noted that position 1 is located inside the product zone, only a couple of millimeters after the flame front. The changes in position for the various measurements of the M-flame are shown in table 3.1, also giving the distance from the burner center. The experiments were conducted at three different equivalence ratios: 0.8, 1.0 and 1.2 . Recalling that the burner radius is 6mm, the experiment conducted at ϕ=1.2 gives the flame front closest to the rim, as would be expected from reference [39]. First the flow rate is set such that it matches the desired equivalence ratio and gives a near vertical flame front on the outer flame front of the M . Subsequently, a scan is performed starting in the product zone, right at the flame front and moving out step by step from one measurement location to another. Five different probe delays are used (21ps, 31ps, 41ps, 51ps and 61ps), from which an optimal one is selected later on, at a probe duration of 4.56ps . For the V-flame the procedure is slightly more simple. The probed section is located in the center of the V-valley, roughly 0.5cm from either flame front, where the rather longitudinal flame should offer more uniform flame conditions along the interaction length. Measurements are taken for equivalence ratios of: 0.5, 0.6, 0.7, 0.8, 0.9, 1.0 . This means a mainly lean combustion regime is probed, one of the reasons being that rich flames are significantly harder to stabilize to the flame holder and re-anchor more regularly to the exit of the burner tube. The V-flame and air experiments are performed at a probe delay of roughly 57ps and probe duration of 3.42ps .

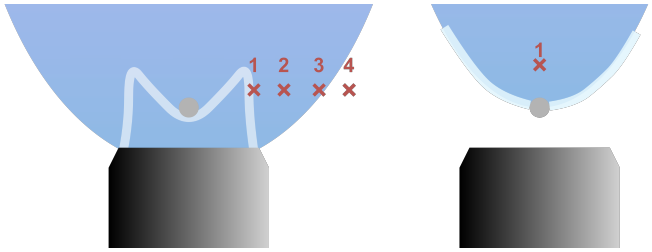

Figure 3.6: Left: The 4 locations where measurements are performed on the M-shaped flame, starting inside the reactant zone and progressing towards position 4. Right: Measurement location in the V-flame.

For every measurement for a given probe delay, 1000 frames are taken. The M- and V-flame measurements are binned 2-by-2 to increase the signal intensity, while a binning of 1-by-1 is applied for the air measurements. Every measurement is conducted with an exposure time of 0.04 seconds. Considering the 1kHz repetition rate of the amplifier system, this means that each image is averaged over 40 shots. After the measurements are conducted, a background measurement is performed using 20 frames to capture the background noise that can later be averaged and subtracted from the resonant spectra. Finally once all the measurements are completed, an argon scan is performed to characterize the probe and the excitation efficiency. Argon is a monoatomic species that does not have any resonant peaks, resulting in a non-resonant signal that is spread evenly over all frequencies. The argon scan is performed through a stepwise change in probe delay, achieved through a stepwise change in translation stage position. The intensity of the argon non-resonant signal scales linearly with the probe, resulting in a mapping of the probe shape. The scan indicates at what position for the translation stage the peak is observed, essentially making it possible to define t=0. The non-resonant signal at t=0 also maps the excitation efficiency, enabling ex-situ correction of the resonant signal. The software used to perform the measurements and view the imaged results is *Andorsolis*®, provided with the Andor Zyla 4.2 sCMOS camera.

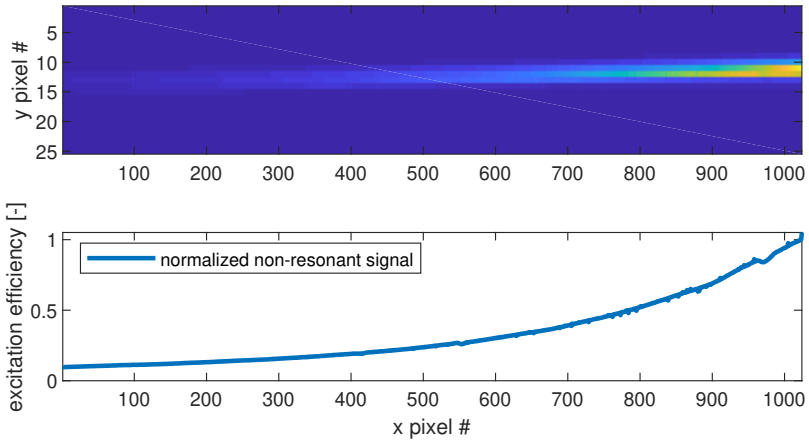

Figure 3.7: Excitation efficiency (bottom) obtained for the V-flame measurements by normalizing the non-resonant signal (top) obtained from the argon scan. The excitation efficiency decreases for higher Raman shifts due to a lower number of pump/Stokes photon pairs of which the difference frequency Ω corresponds to a resonance frequency of the molecule.

Table 3.1: Changes in position for the M-flame experiments.

	position change [mm]				
ϕ	$\Delta\mathbf{x}_{p_1-p_2}$	$\Delta\mathbf{x}_{p_2-p_3}$	$\Delta\mathbf{x}_{p_3-p_4}$	$\Delta\mathbf{x}_{p_1-p_4}$	$\Delta\mathbf{x}_{center-p_1}$
1.2	0.98	3.44	2.15	9.06	5.53
1.0	2.14	5.48	1.25	8.87	4.67
0.8	1.6	3.8	3.66	6.57	4.89

4

Results and discussion

The present chapter takes a close look at the obtained experimental data and the results of the fitting routine regarding temperature and concentration. Section 4.1 first covers how the experimental data is processed to extract the Raman spectra that can be fitted by the code. Then section 4.2 presents the results for the temperature measurements for CO_2, subdivided into a subsection presenting the experimental data, followed by a subsection showing some examples of the resulting fits and finally the data is assessed in the last subsection. This is followed by section 4.3 following the same structure, but focussing on O_2 thermometry. Section 4.4 then explains the method applied for the concentration measurements and presents the final results. Finally section 4.5 takes a critical approach to the data, looking at the correspondence of the evaluated flame temperatures and concentrations to a combustion simulation software ($chem1d$).

4.1. Data Processing

The results from each measurement are composed of 1000 2×2 or 1×1 binned images. Each pixel contains a photon count, saturating at 65535 counts. The data is then processed into cartesian format where the y-axis denotes the normalized intensity and the x-axis the frequency in wavenumbers. The data is calibrated by using the frequency difference between two known peaks (e.g. red and blue fundamental Q-branch peaks). The resulting spectrum can then be fitted by the synthetic library (see fig. 4.1).

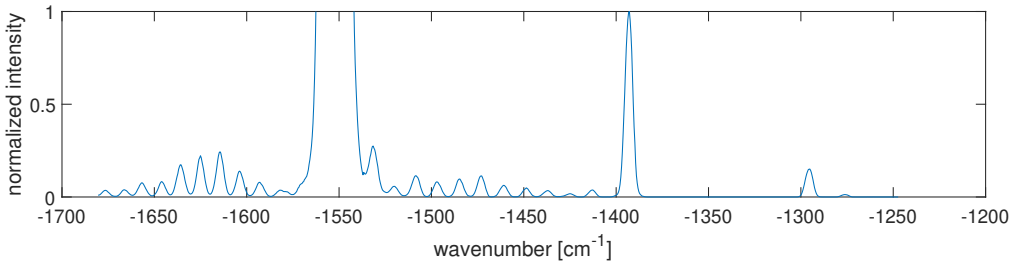

Figure 4.1: Vertically binned image to obtain the peaks at the various frequencies where the oxygen ro-vibrational O-, Q- and S-branches can be seen between -1700 and -1450cm^{-1} and the carbon dioxide Q-branch peaks between -1420 and -1250cm^{-1} .

Along with the resonant images, the corresponding background image for non-resonant background subtraction and the images from the argon scan are loaded. The non-resonant background is averaged over 20 frames and subtracted from each one of the 1000 frames containing the resonant spectra. The background subtraction aims to reduce the noise level to correct for influences such as stray light. As discussed in the previous chapter, the images obtained from the argon measurements serve two purposes. One is to characterize the probe, the other purpose is to correct for the excitation efficiency.

Applying this procedure for every frame makes it possible to reduce image noise and obtain spectra that can be analyzed using the spectral library. The settings for the probe from the argon scan can then be applied to the library to obtain the corresponding theoretical spectra. For every measurement, a frame by frame

fitting analysis can then be performed to find the observed temperature and relative concentration. Finally, an instrument response function (IRF) is implemented to account for line broadening effects that can be attributed to the spectrometer itself. The IRF is the convolution of a Gaussian and Lorentzian profile, resulting in a Voight profile. It leads to an improvement in the robustness of the fits, with the aim of obtaining a better overlap between experimental and synthetic spectra.

In the ensuing analysis, the main guiding quantities to assess the data are the standard deviation (σ) and the mean value of the temperature (T_{ev}) or relative concentration (C_{ev}). The former indicates the precision of the consecutive measurements, i.e. how close every measurement is expected to be to the mean temperature or concentration. Meanwhile, the mean value is compared to the expected temperature (e.g. 293K at room temperature) or concentration, to indicate the accuracy of the method, i.e. how close is the evaluated temperature/concentration to the actual value. The method in this case refers to the type of thermometry or concentration assessment applied. One method consisting of a specific combination of spectral window and molecular species used for the analysis (either oxygen, or carbon dioxide or both). As an example, investigating the CO_2 Q-branch using a spectral window of 1250-1440cm^{-1} is considered as one distinct method.

4.2. CO_2 Thermometry

The fitting routine described in section 2.5 is applied for both temperature and relative O_2-CO_2 concentration. It gives the evaluated temperature and concentration for every frame and determines the observed quantities by averaging the frame by frame values. This section presents the obtained results for CO_2 thermometry, pointing out some peculiarities that are later discussed in section 4.2.3.

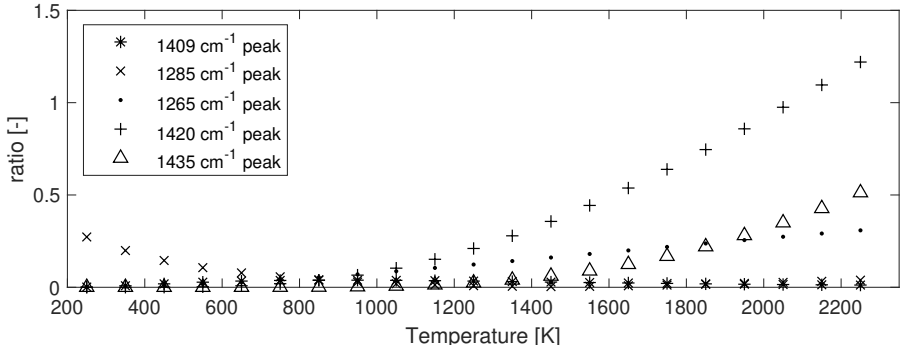

Figure 4.2: Evolution of the CO_2 peaks at 1409cm^{-1}, 1420cm^{-1}, 1435cm^{-1}, 1285cm^{-1} and 1265cm^{-1}, normalized with respect to the blue Q-branch peak at 1388cm^{-1} with τ=41ps obtained from the model. The peaks that show the highest slope in relative intensity w.r.t. temperature are deemed the most sensitive regarding thermometry.

The temperature measurements presented in this section look at one specific spectral window between -1440cm^{-1} and -1250cm^{-1}. The approach looks at performing thermometry on CO_2 using both the red and blue peaks of the Fermi influenced Q-branch. From the synthetic spectra the 6 CO_2 peaks with the strongest CARS signal across a temperature range of 250K to 2300K for the 5 different probe delays are located at about 1388cm^{-1}, 1409cm^{-1}, 1420cm^{-1}, 1435cm^{-1}, 1285cm^{-1} and 1265cm^{-1}. The most consistent peak in terms of intensity across the considered temperature range for a variety of probe delays, is the blue Q-branch peak at 1388cm^{-1}, which is why it is chosen as a normalizing peak. Looking at the evolution of the peaks relative to the peak at 1388cm^{-1}, τ=41ps is deemed most convenient in terms of curve trends and sensitivity. Therefore, the subsequent temperature analyses using CO_2 for the M-flame experiments in this chapter focuses on the measurements taken at a probe delay of 41ps. Figure 4.3 shows the evolution of the peak ratios, where steeper curves indicate a higher temperature sensitivity. At low temperatures the ratio to the red peak at 1285cm^{-1} is clearly important, while at higher temperatures both the ratio to the peak at 1420cm^{-1} and 1435cm^{-1} show significant increases in relative intensity. For temperatures between 600K and 1000K the model seems to have a low sensitivity and one can expect the temperature assessments to be less accurate for those cases. It should be noted that more CO_2 peaks than the ones mentioned here occur just outside of this spectral window. These are deliberately ignored in the analysis for a couple of reasons. One reason is that above 1440cm^{-1}, a peak assumed to originate from hydrogen appears at equivalence ratios above 0.8 . This results in an overlap of the H_2 and CO_2 peaks at about 1450cm^{-1}, interfering with the temperature assessment. The second reason is that below 1250cm^{-1} hydrogen can also interfere with the red peaks and generally the signal-to-noise ratio

(SNR) for the CO_2 peaks below 1250cm^{-1} is too low to say anything meaningful about them.

4.2.1. Experimental data

This section gives a brief overlook of the obtained spectra as they are analyzed from the experiments shown for the CO_2 Q-branch peaks. It begins with presenting the spectra from the air measurements, then shows the M-flame spectra and lastly the experimental spectra obtained for the V-flame. The spectra shown here are the resonant spectra, averaged over 1000 frames.

I. Air measurement

The air experiment results are binned vertically over the complete height of the obtained image, obtained using a probe delay of 56ps and a probe duration of 3.42ps . The spectra shown are averaged over 1000 frames and should hit a temperature of roughly 34°C (307K) [38] for a human breath and 20°C (293K) for the ambient air measurement. The spectra seem to be slightly tilted towards lower wavenumbers. This could lead to difficulties regarding the fitting algorithm for which adequate measures should be taken. The exact reason for this tilt is unclear and is not discussed any further in this work as the quality of the spectra are still deemed sufficient for an analysis. The relative intensities of the peaks and their location in the spectral domain, should not be influenced significantly by this occurrence. The spectra (fig. 4.3a versus fig. 4.3b) look very similar regarding the peaks corresponding to CO_2. The biggest difference being the oxygen S-branch peaks between 1460cm^{-1} and 1420cm^{-1} for the measurements at ambient conditions. The non-resonant signal is also stronger relative to the CO_2 peaks, which can be noticed from the signal intensity not being 0 between 1300cm^{-1} and 1380cm^{-1}. The noise is also higher leading to a slightly more "jagged" curve.

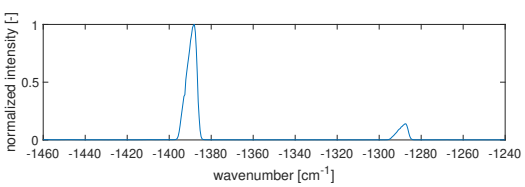

(a) Human breath showing the fundamental CO_2 Q-branch peaks.

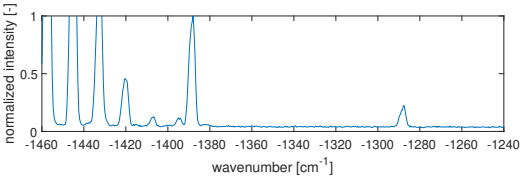

(b) Ambient air showing the fundamental CO_2 Q-branch peaks and a strong signal from the O_2 ro-vibrational S-branch.

Figure 4.3: CO_2 Q-branch experimental spectrum for the air from a human breath and under ambient conditions both obtained for a probe delay of 56ps and a probe duration of about 3.42ps .

II. M-flame

In order to obtain the M-flame results, the spectrum has been binned vertically about a central resonant line. The spectra shown here are the averaged resonant spectra for flame positions 1 (fig. 4.4a) to 4 (fig. 4.4d). The figures show a clear decrease in the CO_2 spectral signature moving away from the flame front. Most noticeable is the peak at 1420cm^{-1}, being very prominent close to the flame front at higher temperatures, but completely disappearing at position 4. At position 4 the higher rotational lines of the oxygen S-branch can be observed (fig. 4.4d), becoming absent closer to the flame front, deeper inside the outer cone. Figure 4.5 shows the peaks at position 1 for the three different equivalence ratios, presented to highlight the appearance of a third major peak at higher equivalence ratios at about 1450cm^{-1} which is assumed to be the fifth rotational line (O5) of hydrogen on the CSRS side. The signal strength of this peak seems to show a dependence on equivalence ratio, being more prominent at ϕ=1.2 and as good as absent for ϕ=0.8, while all the other peaks keep relatively constant intensities.

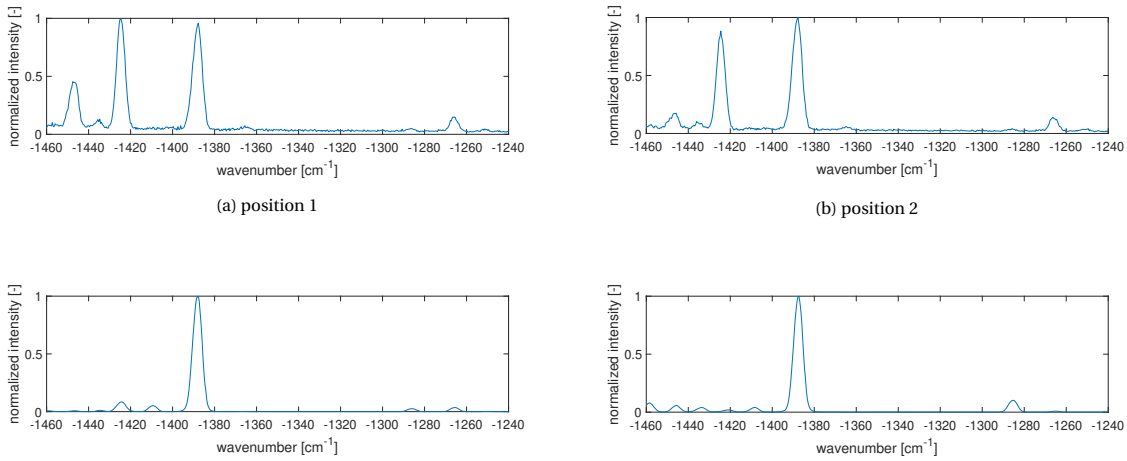

(a) position 1

(b) position 2

(c) position 3

(d) position 4

Figure 4.4: CO_2 Q-branch experimental spectrum for position 1, 2, 3 and 4 for equivalence ratios of 1.0 at a probe delay of 41ps and a probe duration of about 4.5ps. The CO_2 spectral envelope undergoes a number of clear changes with position. Most noticeable is the peak at about 1430cm^{-1}, disappearing completely at position, just outside of the outer flame cone.

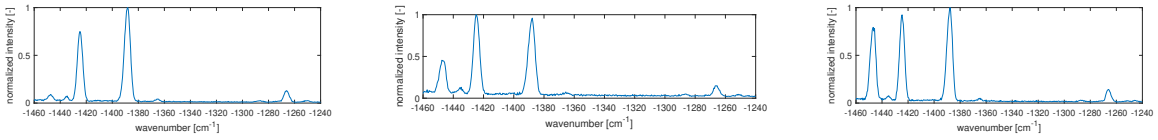

(a) ϕ=0.8

(b) ϕ=1.0

(c) ϕ=1.2

Figure 4.5: CO_2 Q-branch fits for position 1 at ϕ=0.8,ϕ=1.0 and ϕ=1.2 at a probe delay of 41ps and a probe duration of about 4.5ps, showing the emergence of a strong third peak at 1450cm^{-1} assumed to originate from hydrogen.

III. V-flame

The V-flame experiments are processed the same way as the air measurements using vertical binning. The presented figures show the averaged resonant spectra, obtained using a probe delay of 56ps and probe duration of 3.42ps . For increasing equivalence ratio there is a clear increase in relative signal intensity for the peaks at 1420cm^{-1}, 1440cm^{-1} and 1450cm^{-1}, corresponding to higher vibrational transitions. This is an indication that temperature increases with increasing equivalence ratio, where higher vibrational states become populated following the Boltzmann population distribution (fig. 2.3). Similar to the air experiments, the peaks appear to be slightly tilted. The latter becomes more apparent when looking at the graphs in section 4.2.2, where the evaluated synthetic spectrum is plotted over the experimental one.

An interesting thing to note, is that the spectra for ϕ=1.0 and ϕ=0.8 do not exactly match the ones obtained for the M-flame. This has to do with different trends in peak ratio versus temperature, depending on what probe duration and probe delay is used. In fact, a so called "beating pattern" [15] (see fig. 4.6 left) exists in the time domain, as a result of the vibrational bands being unresolved due to the applied probe duration. As such, some peaks undergo significant increases and decreases in intensity (e.g. peak at 1430cm^{-1} for CO_2), considerably altering the spectral fingerprint of the considered molecule over time. The spectra observed under the presented experimental conditions show the Q-branch peaks of CO_2 as one single resonant peak, while in fact they consist of a convolution of a multitude of ro-vibrational resonant lines [9, 10] positioned closely together. Due to the short probe duration, the spectral resolution (≈0.04cm^{-1} assuming a perfect Gaussian probe shape) is too low to show these resonant lines spaced by as little as 0.001cm^{-1} (see fig. 4.6 right). The smaller the spacing between these lines, the stronger they convolve for low spectral resolutions and the more pronounced their combined spectral intensity can become. This convolution, being at the root of this beating behavior, can affect the perceived coherence dephasing rate (linewidth Γ) of the considered molecule [40].

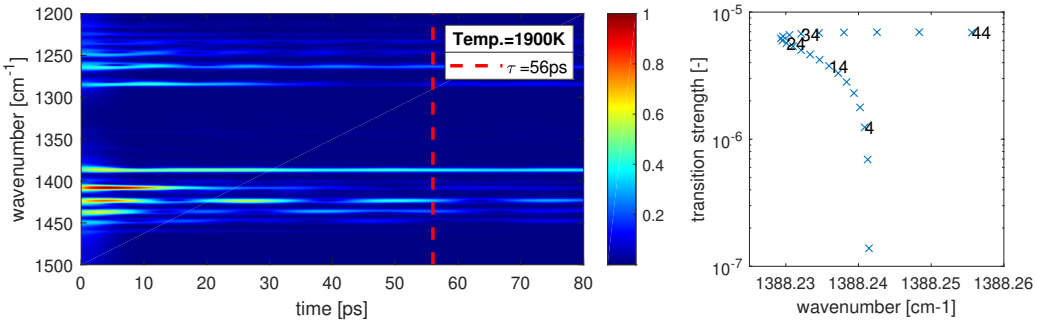

Figure 4.6: *Left:* Simulated beating behavior of the CO_2 red and blue Q-branch peaks for a probe duration of 3.42ps mapped over a duration of 80ps, normalized w.r.t. the maximum observed peak intensity. The evolution of the various peaks due to the unresolved vibrational lines becomes apparent, showing a clear "beating pattern" over time most visible for the hotbands. The vertical line indicates where the observed spectra using a probe delay of 56ps are located. *Right:* Positions of the resonant lines and their respective transition strength corresponding to the $J \rightarrow J, v \rightarrow v+1$ transitions of the CO_2 Q-branch peak at 1388cm^{-1} located between 1388.2cm^{-1} and 1388.26cm^{-1} . The numbers indicate to which J-number the position corresponds.

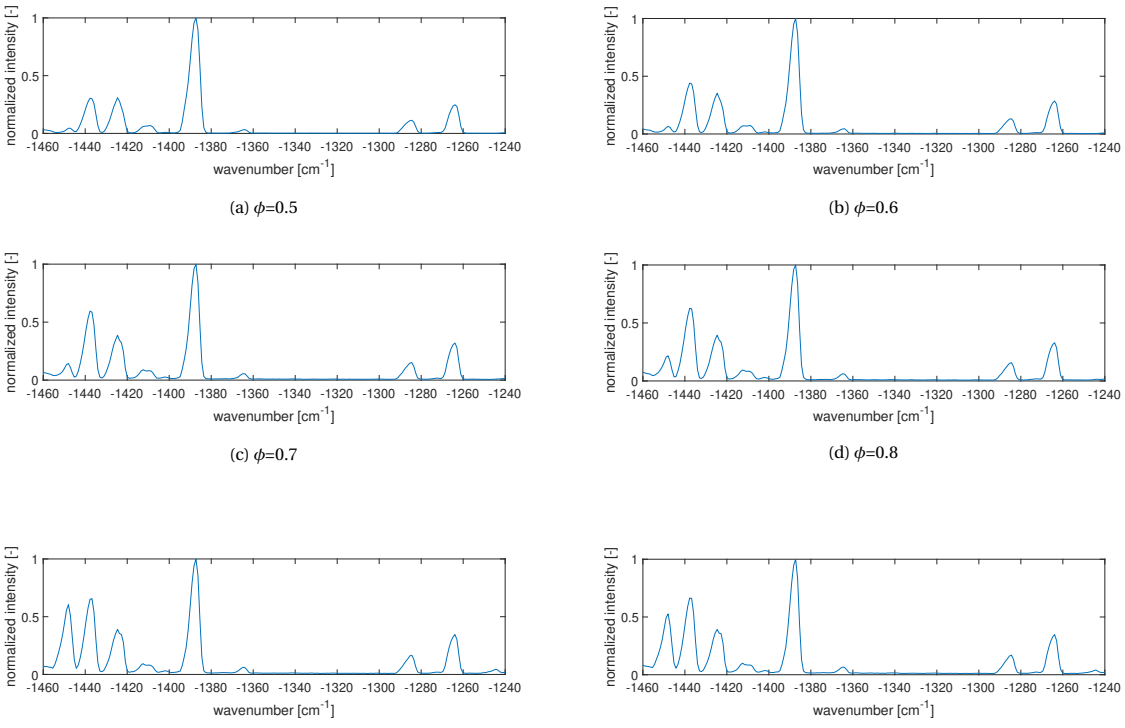

(a) ϕ=0.5 (b) ϕ=0.6

(c) ϕ=0.7 (d) ϕ=0.8

(e) ϕ=0.9 (f) ϕ=1.0

Figure 4.7: CO_2 Q-branch experimental spectrum for the V-flame experiment at ϕ=0.5, ϕ=0.6, ϕ=0.7, ϕ=0.8, ϕ=0.9 and 1.0 obtained for a probe delay of 56ps and a probe duration of 3.42ps . The most noticeable variations in the spectrum can be seen above 1420cm^{-1}, where the peak at 1450cm^{-1}, is again assumed to be part of the hydrogen spectrum.

4.2.2. Spectral fits

This subsection presents the spectral fits obtained for CO_2, using the spectral window between -1440cm^{-1} and -1250cm^{-1}. The fits are inspected by looking at the residual from the theoretical and synthetic spectra, plotted together in each of the presented figures. The aim is essentially to obtain an optimal overlap by minimizing the residual as is described in the section on the spectral fitting routine (see section 2.5).

I. Air measurement

The measurements performed on the exhaled human breath, show a relatively good correspondence in terms of peak intensity. However, as mentioned before, one issue that can be noticed is that the experimental peaks are slightly tilted. Even though the peak intensities seem to match well, it does not give a good overlap between the simulated and the experimental spectra. The peaks match well in width at their base, but diverge closer to the top. It is assumed however that due to a good match in relative intensity and thus a good match in peak ratio, that the fits are reliable enough for a temperature assessment. Also when increasing or decreasing the linewidth using the instrument response function (IRF), σ seems to increase without significantly changing the mean temperature of the 1000 frames. This indicates that the best conditions for the spectral fit should be met, giving the highest quality fits possible given the circumstances. The ambient air experiment compared to the one performed on the human breath shows more noise, which is due to the overall signal intensity of CO_2 caused by a lower concentration at ambient conditions.

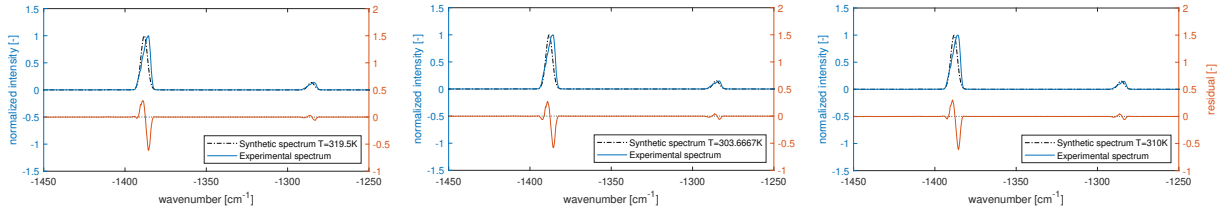

Figure 4.8: Three fits arbitrarily chosen for the measurement conducted in air showing the fundamental blue and red Q-branch peak. The synthetic spectrum accentuates the slight tilt in the experimental spectrum.

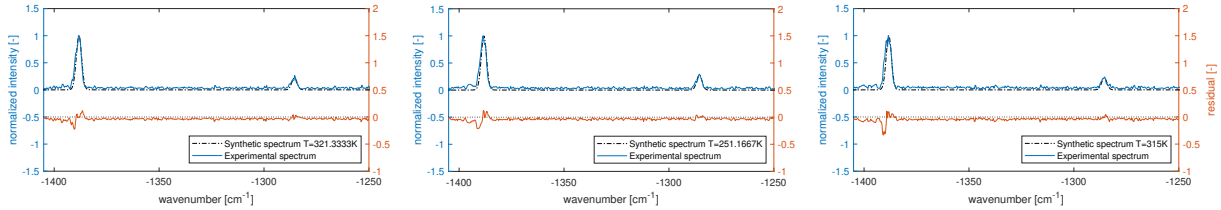

Figure 4.9: Three fits arbitrarily chosen for ambient conditions showing the fundamental blue and red CO_2 Q-branch peak . The relative peak intensities do not seem to differ from the measurements conducted on a human breath, but a clear increase in noise can be noticed.

II. M-flame

The M-flame fits generally show a good overlap with the experimental spectra. Nonetheless, a couple of reoccurring discrepancies can be noticed. One is that at higher temperatures, the first hotband peak of the red side of the Q-branch at 1265cm^{-1} is overestimated by the model in nearly every frame. Meanwhile, on the blue side this is the case for the third hotband at about 1435cm^{-1}. At lower temperatures this discrepancy seems to disappear almost completely giving a satisfactory overlap of both the synthetic and experimental spectra. This might indicate that there is a theoretical discrepancy in the model, pointing at a possible dependence of the polariziability on temperature. Another reason might be that the probe delay and/or duration is ill defined, leading to different beating patterns than anticipated. The noise level is noticeably higher for higher temperatures (see fig. 4.10 versus fig. 4.13), which is due to the already previously described drop in density leading to a lower overall signal intensity.

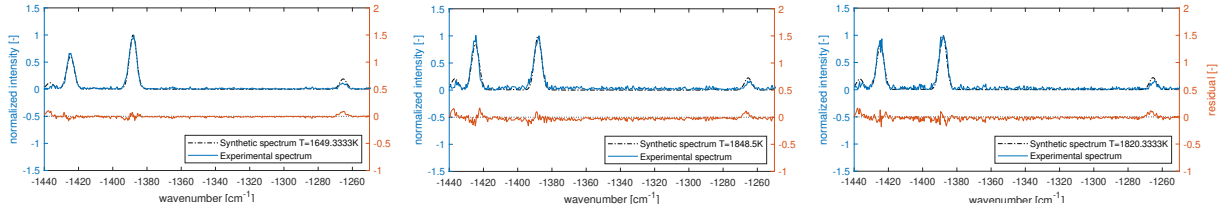

Figure 4.10: Three fits arbitrarily chosen for position 1 for different equivalence ratios of 0.8, 1.0 and 1.2 (left to right).

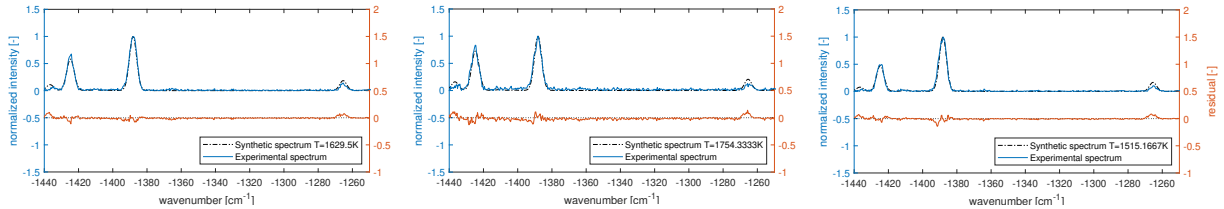

Figure 4.11: Three fits arbitrarily chosen for position 2 for different equivalence ratios of 0.8, 1.0 and 1.2 (left to right).

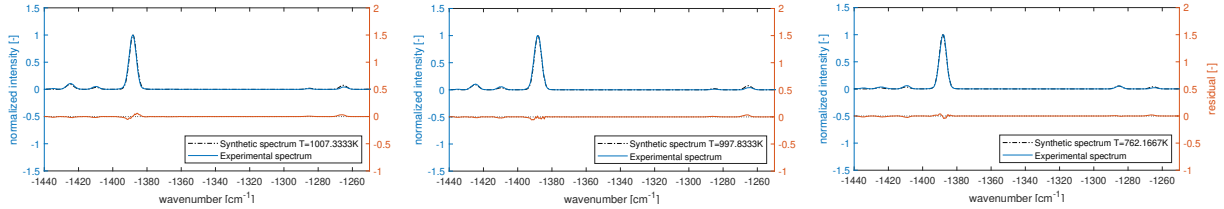

Figure 4.12: Three fits arbitrarily chosen for position 3 for different equivalence ratios of 0.8, 1.0 and 1.2 (left to right).

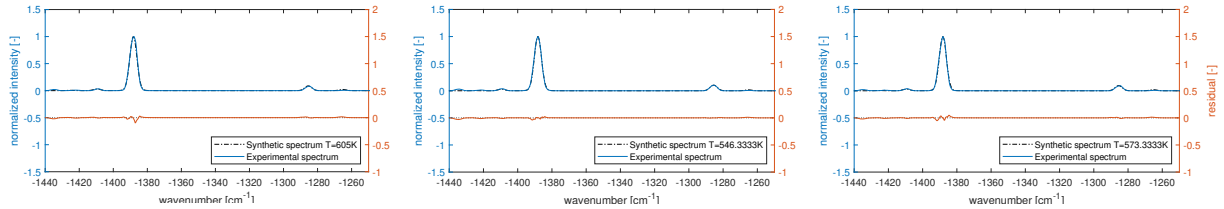

Figure 4.13: Three fits arbitrarily chosen for position 4 for different equivalence ratios of 0.8, 1.0 and 1.2 (left to right).

III. V-flame

The V-flame measurements give a good correspondence of the synthetic and experimental spectra. Nonetheless, they suffer from the same tilted spectrum as the air measurements as both were performed on the same optical setup. Similarly the peak intensities show a good correspondence between synthetic and experimental spectra, while the superposition of the spectral shape is slightly off.

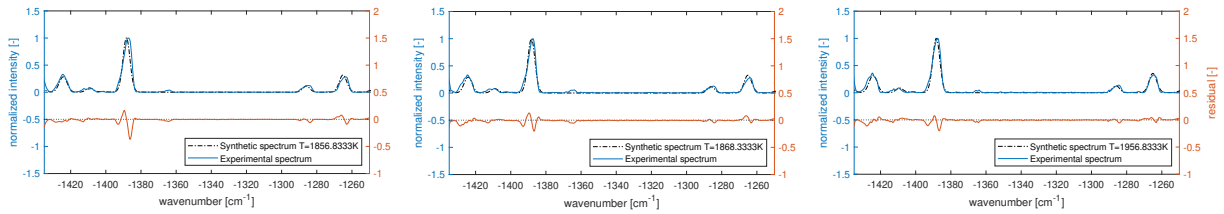

(a) ϕ=0.5 (b) ϕ=0.6 (c) ϕ=0.7

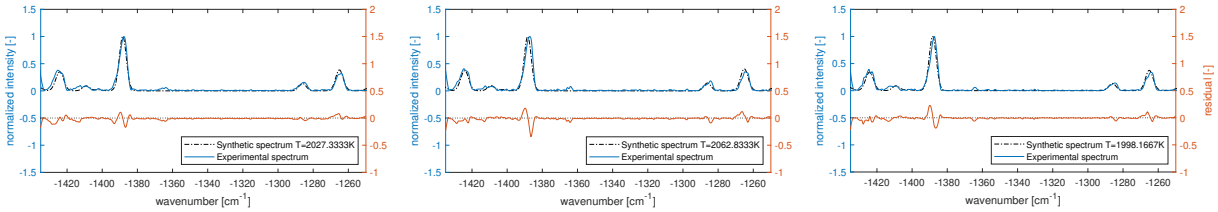

(d) ϕ=0.8 (e) ϕ=0.9 (f) ϕ=1.0

Figure 4.14: CO_2 Q-branch experimental spectrum for the V-flame experiment at ϕ=0.8, ϕ=0.9 and ϕ=1.0 .

4.2.3. Discussion

The present section discusses the CO_2 CARS thermometry performed on the experimental spectra for the three experimental cases described chapter 3. Through a number of temperature histograms the various results are compared and give an indication on the accuracy and precision of the considered method used for CO_2 thermometry.

I. Air measurement

The evaluated temperatures for the air experiments predict the expected temperatures with relative accuracy. The average temperature of a human breath is roughly 307K (34°C)[38], while the evaluated temperature by the model is 318K (accurate within 3.6%) with a standard deviation of 7.72K (2.43%). Temperature fluctuations observed under these experimental conditions can in reality not differ by more than 16K (approximate difference between ambient temperature recorded in the laboratory and human normal body temperature), thus giving a rather stable probe medium to analyze when compared to the flame experiments. As these experiments are not conducted in a reacting medium with considerable changes in properties due to flame fluctuations, the precision of the measurement should be positively affected. It should also be considered however, that only two peaks are available for fitting, which can decrease the robustness of the method. For the experiment under ambient conditions, the standard deviation is higher (30.71K, ≈9.6%), and 24K (~8%) off from its expected value of 293K. A reason for the higher σ in temperature and higher inaccuracy of the evaluated value is most likely the lower SNR (see fig. 4.9) changing from 70dB to 20dB, as a result of a low concentration in CO_2 (~100× lower than in human breath [37]), combined with the presence of only two peaks, which decreases the precision due to an increase in random error. The results indicate that CO_2 Q-branch thermometry, which is largely dependent on the population fraction of the vibrational levels, is not as suitable for low temperature applications as O_2 ro-vibrational O-branch thermometry, which will be elaborated further upon in section 4.3.

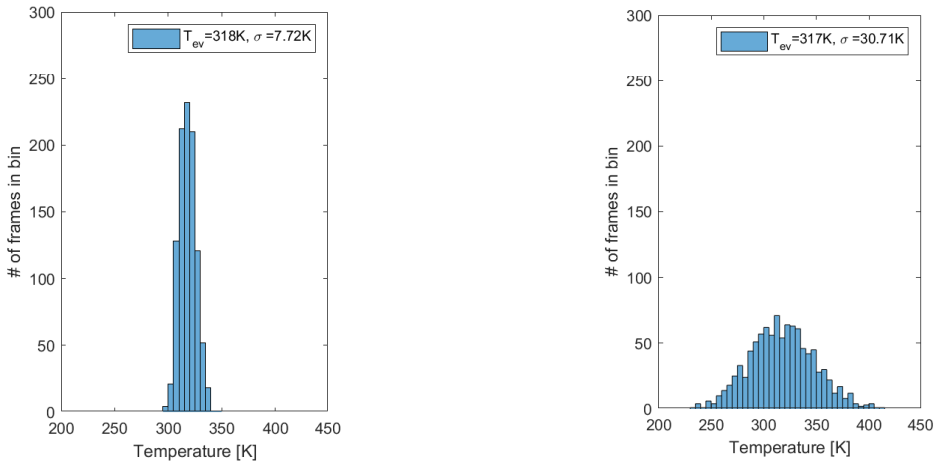

Figure 4.15: Left: Histograms binned in steps of 5K measured in the exhaled breath of a human using the CO_2 blue and red peaks. Right: Histograms binned in steps of 5K measured in ambient conditions using the CO_2 blue and red peaks.

II. M-flame

The histograms in fig. 4.16a, fig. 4.16b and fig. 4.16c reveal a number of interesting points. First off, the temperatures decrease as one moves further away from the flame front for all of the three equivalence ratios. Another point to mention is that higher temperatures seem to have a lower standard deviation (50K>σ, ≈2.48% for position 1) than lower temperature regions. The position with the highest standard deviation in terms of Kelvin is position 3 (103.2K≈11.37% on average) in all three graphs, while the experiments using ϕ=0.8 (fig. 4.16a) have the lowest standard deviation overall. One more thing to note is that the experiments using an equivalence ratio of 1.0 (fig. 4.16b) show the highest temperature at position 1, followed by the experiments conducted for ϕ=1.2 (fig. 4.16c) and then by ϕ=0.8 (fig. 4.16a). Most of the distributions in the figures show a Gaussian-like distribution. However, two distributions noticeably deviate from this general shape: position 3 for ϕ=1.0 and position 4 for ϕ=1.2 . The former seems to have a secondary distribution centered at roughly 1200K, while the latter seems to lean to lower temperatures. This can probably be linked to the location of these measurement positions, where the outer flame cone can be moving in and out of the probe section, leading to two very distinct regions being probed.

One of the possible reasons why the standard deviations of these measurements are relatively high, is assumed to be the unstable experimental platform. When looking at the frame to frame spectra, there appear to be considerable changes in the relative intensities of the peaks indicating substantial changes in temperature and concentration of the probe medium. This can be attributed to the flame oscillating in space, resulting in an unsteady flame region.

An explanation for the increase in standard deviation as one progresses away from the flame front, could also be attributed to the flame oscillating increasingly when progressing towards position 4 corresponding to the outer flame regions, further increasing the temperature divergence. Another reason could be the lower sensitivity between 600K and 1000K (see fig. 4.3) especially for position 3, having the highest standard deviation in every set of experiments corresponding to one equivalence ratio. This forms the basis for taking the decision to perform an experiment inside the valley of a V-flame and in air, mitigating the mentioned effects. These two experiments, should provide a more homogeneous medium in terms of concentration and temperature along the probed section and the air experiments give a fixed, known temperature to compare to.

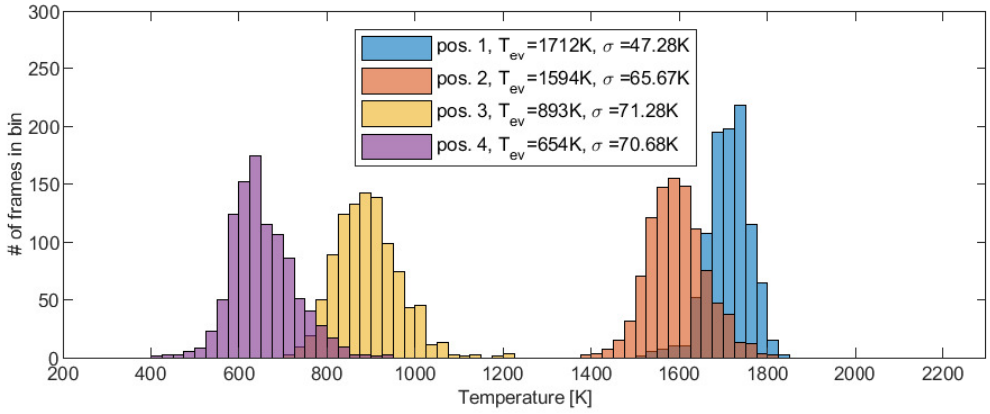

(a) ϕ=0.8

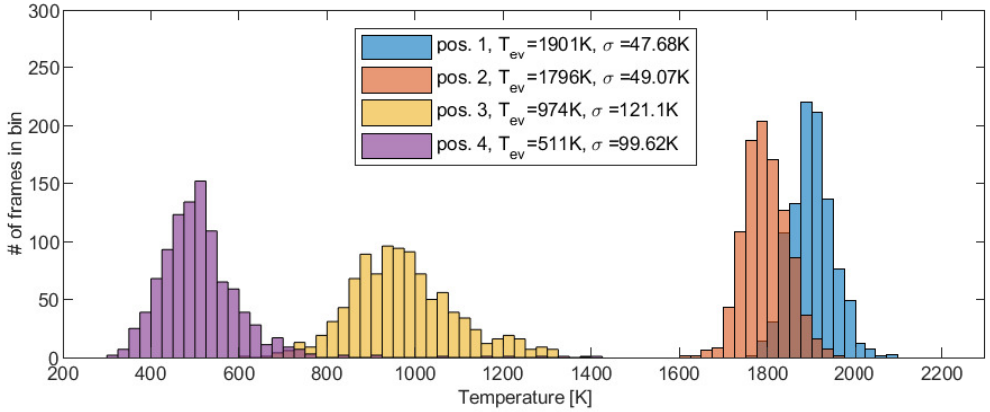

(b) ϕ=1.0

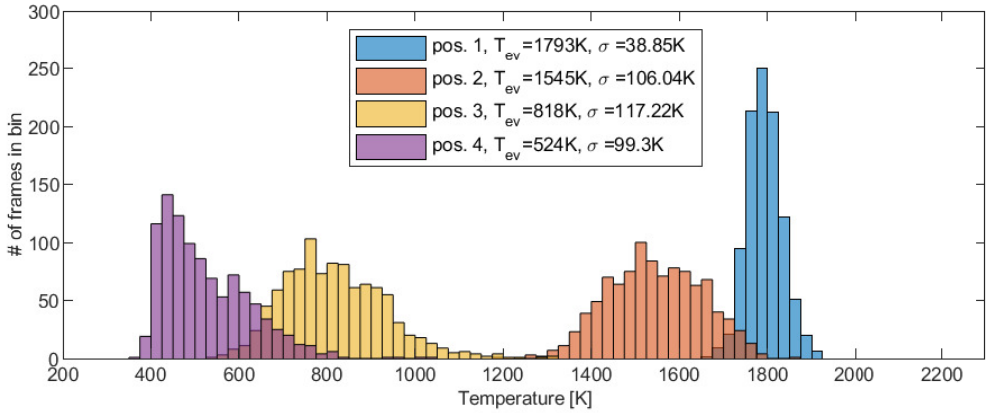

(c) ϕ=1.2

Figure 4.16: Histograms binned in steps of 25K for $\phi = 0.8$, $\phi = 1.0$ and $\phi = 1.2$ for positions 1-4 in an M-shaped flame using both blue and red CO_2 peaks.

III. V-flame

The V-flame experiments nearly all give standard deviations below 45K (σ of ≈1.9% on average). Comparing this precision to precisions described by works applying the same two-beam CARS technique such as Kearney (2014) [15] reporting a precision of 1% or Vestin et al. (2008) [17] of 2-3%, then 1.9% can be judged as a satisfactory result. Only the experiment conducted at ϕ=0.5 showed a higher σ. A good indication is that the higher the equivalence ratio, the higher the evaluated temperature, as can be expected. Nonetheless, the temperature steps between the experiments with ϕ=0.7 up to 1.0 are small (10K at a time), which is small considering a temperature change of ~60K between ϕ=1.0 and ϕ=1.2 in fig. 2.10.

The worst temperature evaluation according to highest σ is for ϕ=0.5, with σ=63.73K . When looking at the frame to frame temperature analysis however, frames #20 to #30 and #210 and #250 show an abrupt decrease in temperature evaluation. The reason for this local decrease is unclear, but a possibility might be a sudden gust of air leading to a considerable shift in flame region or an unexpected pocket of air in the premixed gas. The concentration analysis (see section 4.4) seems to support this possibility, since the same frames (see fig. 4.28 right) show a considerable increase in relative O_2-CO_2 concentration. This makes it possible to argue that the shift in temperature evaluation for these frames is indeed due to a temporary fluctuation of properties in the pre-mixed gas, possibly caused by a jump in the flow meters. Since in that case, the local decrease in temperature is caused by the measurement platform rather than the measurement technique itself, it is possible to neglect these frames leaving 950 frames for analysis. The evaluated temperature then changes

to 1814.8K, with a standard deviation of 22.97K, the lowest of all four experiments. Contrary to the M-flame experiments, lower temperature regions seem to show a lower standard deviation. These results together with the air experiment seems to indicate a trend, that lower flame temperatures show lower deviations in terms of Kelvin. Speaking in terms of percentages, σ for ϕ=0.5 is 1.27% at 1814K as compared to 2.16% for ϕ=1.0 at 2066K . Regarding these points the arguments for moving to a V-flame from an M-flame, also seem to be justified by the outcomes. The larger σ for higher equivalence ratio, could be explained by the flame becoming increasingly unstable since it becomes more likely for the flame to re-attach to the buner exit when more fuel is added to the mixture. This leads to an augmented oscillation of the flame front on either side of the flame holder, possibly leading to the higher fluctuations in temperature.

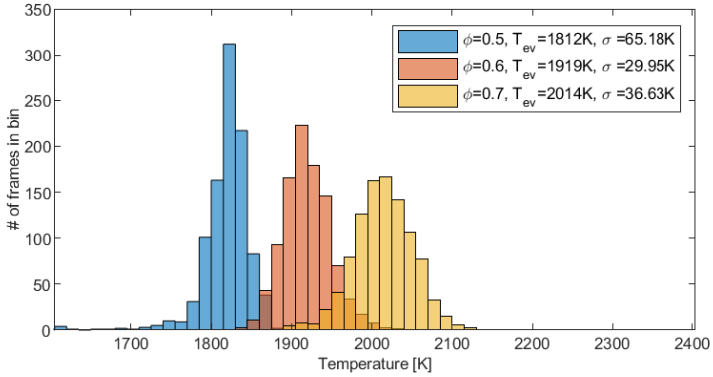

(a) CO_2 temperature histograms for the V-flame experiments for ϕ=0.5, 0.6 and 0.7, binned in 15K bins .

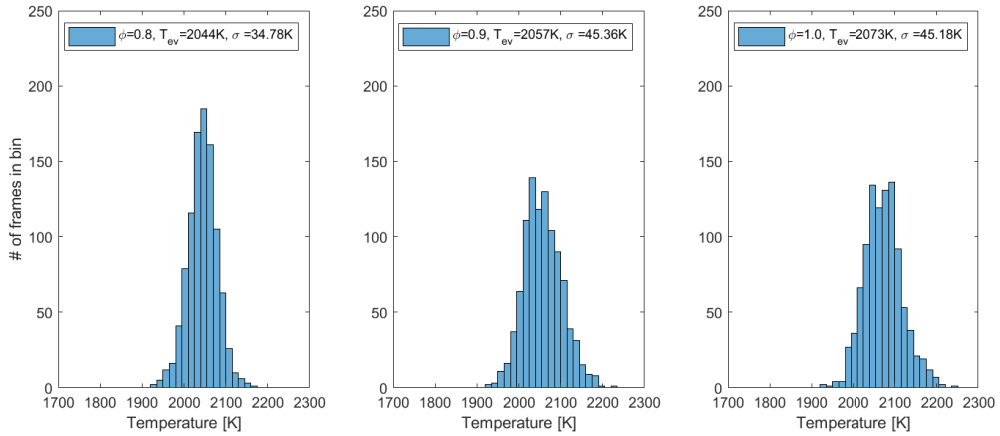

(b) CO_2 temperature histograms for the V-flame experiments for ϕ=0.8, 0.9 and 1.0, binned in 15K bins . The evaluated temperatures span over a range of only 33K, which is why they are shown in three separate plots.

Figure 4.17

4.3. O_2 thermometry

The oxygen thermometry, similar to the CO_2 thermometry looks at a spectral range that disregards the influences of other molecular species, in this case CO_2 and H_2. Therefore the spectral window between 1680cm^{-1} and 1430cm^{-1} is chosen, where the O-, Q- and S-branch of O_2 can be observed. The analysis focuses on the Q-branch and O-branch, where especially the former is key for concentration measurements since the latter is only observable in low temperature regions, which are high in oxygen content. Nonetheless, not all experimental spectra presented oxygen branches that can be used for thermometry. The reason for this can be a low SNR, which is often the case in flame regions where oxygen is present in low concentrations (e.g. V-flame experiment for ϕ=0.7-1.0,). Low SNR results in imprecise temperature evaluations comparable to what is observed in fig. 4.15 for the CO_2 fits in air under ambient conditions. Another reason for discarding the oxygen spectrum for thermometry can be due to saturation of the oxygen Q-branch peak or in some measurements insufficient spectral information (e.g. only one usable peak available). In contrast to CO_2, O_2 is not impacted by Fermi interference in this spectral region, this provides less peaks to analyze. In addition, the O_2 individual vibrational peaks are also spread over a larger section in the spectrum, leading to a higher overlap of its Q-branch peaks. This increases the challenge of performing an analysis exclusively on the O_2 Q-branch, since the variation in spectral envelope is less pronounced for a change in temperature.

4.3.1. Experimental data

In this subsection the relevant experimental data on which O_2 thermometry can be performed is presented. Due to the considerations mentioned in the introduction of this section, not all data can be used. Therefore only 4 experimental cases are examined for O_2 compared to 20 for CO_2. Even though no O_2 thermometry is performed for the V-flame experiment, the experimental spectra are still discussed briefly to highlight a couple of interesting points.

I. Air measurement

The air spectra are obtained in the same manner as the CO_2 spectra, using the same vertical binning procedure, looking at the spectral window of -1680cm^{-1} and -1450cm^{-1} . The measurement probing the breath, can not be used for thermometry since it does not show a ro-vibrational O- or S-branch and only shows a single peak for the Q-branch. The measurement performed purely in air though can be used to perform thermometry. The peaks here are also slightly tilted, but not to the same extent as is the case for the CO_2 data.

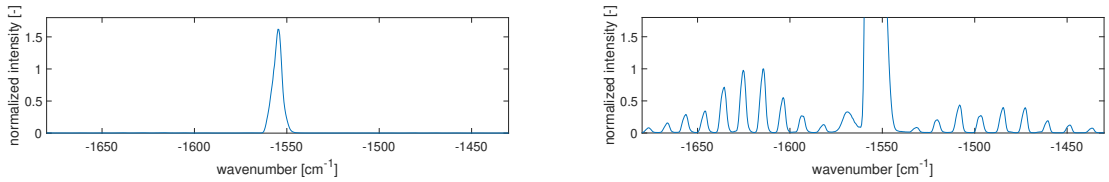

Figure 4.18: Left: O_2 Q-branch experimental spectrum for the air measurement in breath. Right: O_2 O-, S- and Q-branch experimental spectrum for the air measurement under ambient conditions.

II. M-flame

Analogous to the air experiment, the M-flame data for O_2 is obtained in the same manner as for CO_2. Depending on whether the Q- or O-branch is assessed a spectral window of 1680cm^{-1}-1430cm^{-1} or 1680cm^{-1}-1580cm^{-1} is used respectively, normalizing to the highest, unsaturated peak available. Position 1 offered too low a signal for oxygen to be examined, while position 3 offered too few unsaturated frames for a Q-branch analysis. The latter is also true at position 4, but the ro-vibrational O-branch seemed adequate for thermometry. Nonetheless, there proved to be too high discrepancies between the synthetic and experimental spectrum, with too little peaks for a meaningful analysis and was thus left out for this experiment. The distinct shape of the Q-branch and its hotbands in position 2 however, make it interesting to analyze and compare to the CO_2 results.

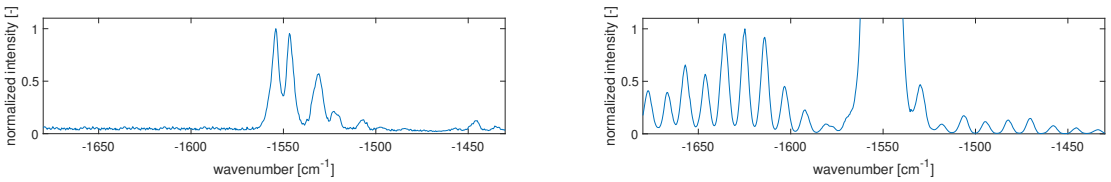

(a) position 2

(b) position 4

Figure 4.19: O_2 O-, Q- and S-branch experimental spectrum for position 2 and 4 for an equivalence ratios of 1.0 .

III. V-flame

Finally the V-flame measurements are obtained the same way as the air measurements, looking at the spectral window of -1580cm^{-1} and -1450cm^{-1} . What is interesting to note though, and what becomes clear from the figures below, is that the relative peak intensity of the O_2 Q-branch shrinks from 2.5 (normalized w.r.t. 1388cm^{-1} CO_2 peak) for ϕ=0.5 to nearly 0 for ϕ=1.0, indicating a significant decrease in relative oxygen concentration. Due to a higher probe delay, the shape of the O_2 Q-branch and its hotbands is expected to be different. Nonetheless, the model had an unconvincing correspondence to the experimental spectra (see fig. 4.20), which could not be resolved. The three shallow peaks between 1510cm^{-1} and 1540cm^{-1} give a relatively good fit, but the fundamental peak is evidently off. It is assumed that the observed tilt, and the averaging over 40 shots, play a role in this discrepancy. The tilt can lead to a stronger overlap of the O_2 Q-branch peaks leading to unpredictable peak envelopes, while the shot averaging can lead to an overlap of multiple spectra, individually corresponding to slightly different temperatures.

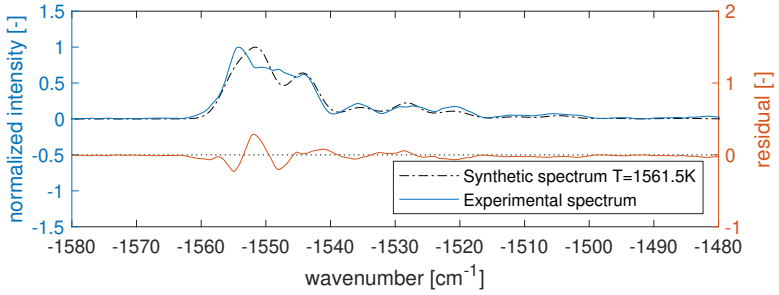

Figure 4.20: Example of an O_2 Q-branch fit for ϕ=0.5, clearly showing a mis-fit regarding the fundamental Q-branch peak. It is assumed that a combination shot averaging (40 shots) and tilted spectral peaks is causing this issue.

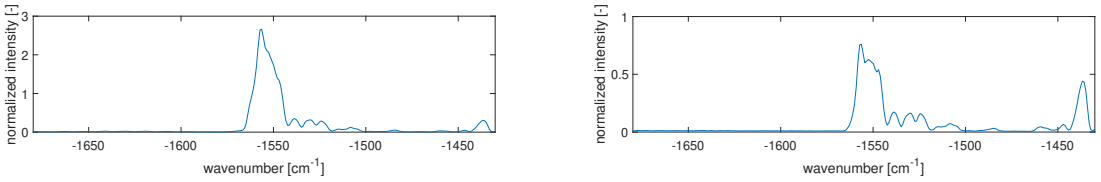

(a) ϕ=0.5

(b) ϕ=0.6

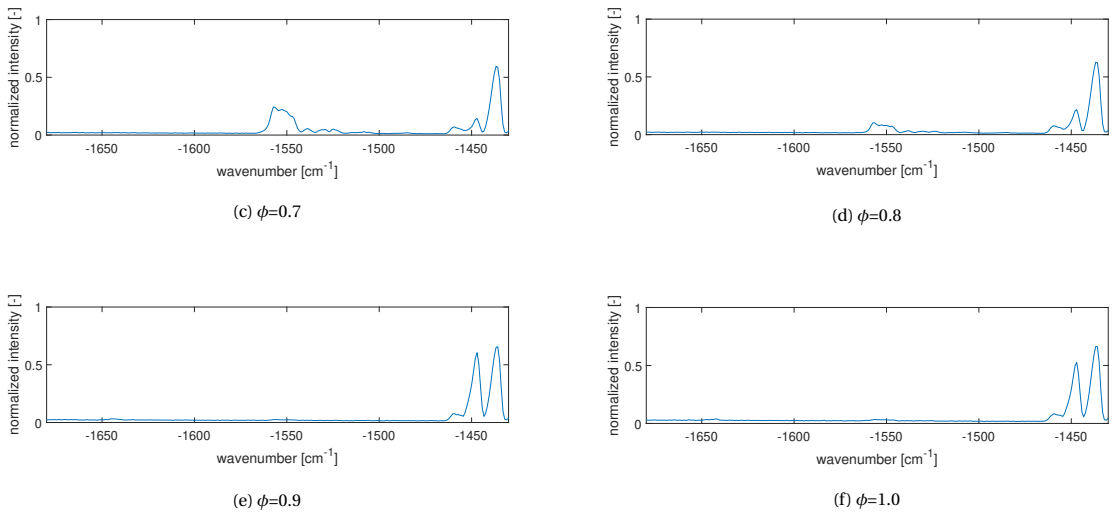

(c) ϕ=0.7 (d) ϕ=0.8

(e) ϕ=0.9 (f) ϕ=1.0

Figure 4.21: O_2 Q-branch experimental spectrum for the V-flame experiment at ϕ=0.5, ϕ=0.6, ϕ=0.7, ϕ=0.8, ϕ=0.9 and 1.0 for a probe delay of 56ps and a probe duration of 3.42ps. The spectra are normalized to the CO_2 fundamental Q-branch peak at 1388ccm^{-1} to emphasize on the change in relative peak intensity. Evidently, the Q-branch peak decreases considerably in relative intensity from ϕ=0.5 to ϕ=1.0 , indicating a substantial evolution in oxygen concentration.

4.3.2. Spectral fits

This subsection presents the spectral fits obtained for O_2, using two spectral windows. One between -1580cm^{-1} and -1450cm^{-1} for the Q-branch, and the second one between -1680cm^{-1} and -1580cm^{-1} for the O-branch. The fits are inspected by looking at the residual from the theoretical and synthetic spectra, all plotted together in the presented figures.

I. Air measurement

The air measurement at ambient conditions (T_{amb}=293K, $C_{O_2-CO_2amb}$ ≈500) makes it possible to test the rotational thermometry capability of the model. The O-branch fits show a good correspondence for most of the peaks. It becomes clear however that the second and third peak (1592cm^{-1} and 1603cm^{-1} respectively) consistently show lower signal intensities than expected from the synthetic spectra. The reason for this is unknown, but could be due to a local mis-characterization of the excitation efficiency or an overlooked physical aspect that is not included in the O_2 model. A local mis-characterization of the excitation efficiency in this case is regarded as a discrepancy between the non-resonant signal that is observed in the flame, versus the signal detected during the argon scan. One important aspect to point out, is that the argon scan is an ex-situ measurement of the non-resonant signal and thus gives an ex-situ characterization of the excitation efficiency. The argon scan is performed at room temperature at pressures close to atmospheric. This differs from the conditions observed in a reactive medium such as an methane-air flame, where temperatures above 2000K can be measured. In this regard, the in-situ, non-resonant signal that corresponds to flame conditions, can differ from the one obtained from the argon scan, potentially leading to a mis-characterization of the excitation efficiency.

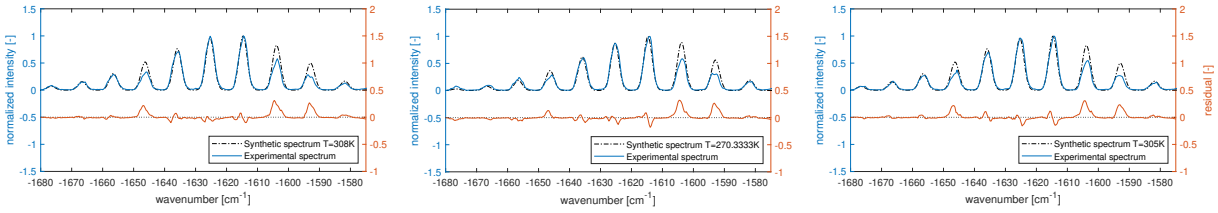

Figure 4.22: Three fits arbitrarily chosen for ambient conditions taken at random for O_2 O-branch measurement .

II. M-flame

The oxygen fits for the M-flame experiment at position 2 show satisfactory superposition of the synthetic and experimental spectra. Nothing out of the ordinary can be noticed on a consistent basis looking at the frame to frame fits regarding spectral inadequacies. Overall giving confident results from a spectral fitting perspective.

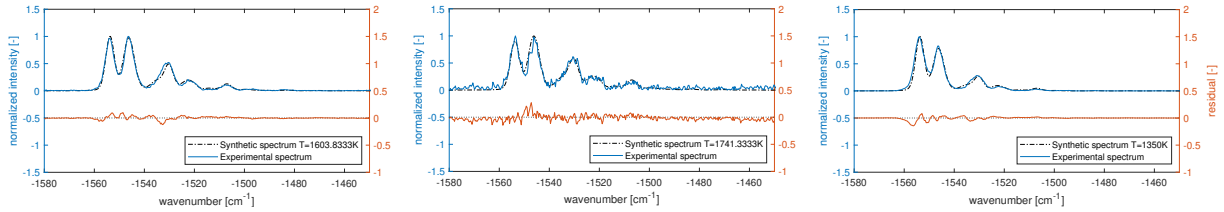

Figure 4.23: Three fits arbitrarily chosen for position 3 taken at random from different equivalence ratios of 0.8, 1.0 and 1.2 .

4.3.3. Discussion

The present section discusses the temperature analysis of the experimental spectra for the three experimental cases described in chapter 3 (air, M-flame, V-flame). Through a number of temperature histograms the various results are compared and give an indication on the accuracy and reliability of the considered method used for O_2 thermometry. Possible patterns are brought to attention and potential reasons are mentioned that are discussed further in the conclusion.

I. Air measurement

The experiments conducted in air, provided only one analyzable dataset, which is the one conducted in air at ambient conditions, showing the O_2 O-branch. The experiment probing the human breath, contained too little spectral information on O_2 for thermometry, providing only a single resonant Q-branch peak for analysis. The assessment on the O-branch shows an increased temperature measured up to frame #150 (see fig. 4.24), before dropping to lower temperatures. Looking at the frame to frame data in *Andorsolis* it becomes clear that around frame #150 the signal intensity decreases slightly while the peak distribution also shifts, giving lower temperature evaluations. Hence, in the histogram two separate distributions seem to appear. The frame to frame analysis however, does not jump between two temperature extremes as observed in the M-flame measurements and stays rather constant. Neglecting the first 150 frames, brings the temperature down to 294.82K and σ to 9.67K (≈3.27%), corresponding quite well to the expected temperature of 293K, greatly increasing the precision and accuracy. Interestingly the first 150 frames have nearly the same σ (σ=9.70K) as frames above 150, but give a mean temperature of 336.02K .

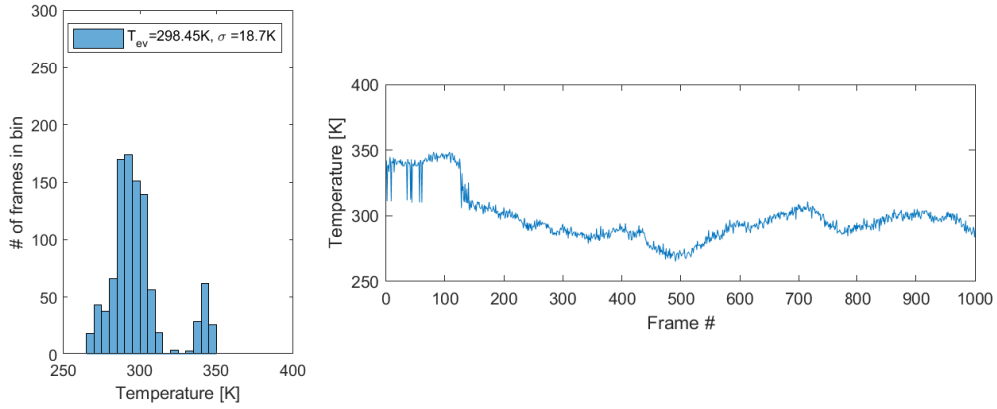

Figure 4.24: Left: O_2 O-branch temperature histogram for air at ambient conditions ($T_{amb.}$=293K) in bins of 5K. Right: O_2 O-branch frame to frame temperature trend for air at ambient conditions, clearly showing a change in temperature evaluation around frame #150.

II. M-flame

The only thermometry conducted on O_2 for the M-flame experiments are for position 2 since all frames can be used, the spectrum does not saturate and the SNR is high enough for a reliable analysis. An interesting point to note is that the histograms in fig. 4.25 seem to be split into two distributions, one centered at a higher and one centered at a lower temperature. Using *Andorsolis* to look at the frame to frame spectra, it becomes clear that the flame conditions change quite rapidly for the analysis with ϕ=0.8 and ϕ=1.2, giving very distinct spectra from one frame to another. In fig. 4.27a the frame to frame evaluated temperature trend is depicted for the oxygen M-flame analysis at ϕ=1.2 , while fig. 4.27b gives an idea of how much three successive frames can differ by comparing their obtained spectra. In fig. 4.27b a distinction can not only be made in terms of peak intensity, but also by looking at their spectral envelope. When comparing the peaks around 1550cm^{-1} for frame #31 to the one for frame #30, a clear change in peak ratio can be distinguished. Meanwhile, the notable difference in peak intensity also hints at a sudden change in oxygen concentration. These points indicate that the most probable cause for the high standard deviation (σ>90K, ≈7.77% on average), is due different flame regions wavering in and out of the probe medium. Next to the possibility that this imprecision is due to the inherent flame oscillations in space, the averaging of the data can also be of influence. A relatively long interaction length (~1cm) paired with images averaged over 40 shots, can make it difficult for the model to accurately diagnose the observed temperature. Slight temperature variations along the interaction length, together with a shifting flame position could lead to a convolution of spectra corresponding to different temperatures. Nonetheless, the temperature fits show satisfactory results, which implies that the effect of the averaging can only be minor. This makes it more probable that the jumps are indeed due to the fluctuations of the flame front rather than the averaging.

Taking a closer look at the temperature evaluation for ϕ=1.0, a sudden drop in temperature can be noticed for frames above #900 (see fig. 4.26) . Inspecting the concentration evaluation for these frames, it becomes clear that a sudden increase in oxygen can be noticed, which again implies that some disturbance in the regular gas flow might have occurred. Ignoring these frames increases the temperature to 1853K and decreases the standard deviation to 81.09K .

Looking back at the temperature evaluations of the same position for CO_2 (see fig. 4.16a, fig. 4.16b and fig. 4.16c) they seem to be corresponding to an acceptable degree, with a maximum of 82K between the O_2 and CO_2 temperature evaluation for ϕ=0.8 and a minimum difference of 40K for ϕ=1.2 . In fig. 4.26 both the O_2 and CO_2 evaluations seem to follow the same temperature trend. The CO_2 temperature evaluations give lower values than the O_2 evaluations. The CO_2 results however, do not seem to be affected by the same "splitting" of the temperature distribution as the O_2 thermometry results. For the three equivalence ratios ϕ=1.0, gives the lowest standard deviation, for both the O_2 and the CO_2 thermometry. Meanwhile, for both methods, the standard deviation for the evaluated temperature for ϕ=1.2 is the highest. This could be linked to the stability of the combustion process, being more stable around stoichiometric conditions. In this regard, one could also say that a lean burning condition is more favourable for flame stability than rich conditions. The reason why the "splitting" occurs for oxygen and not for carbon dioxide could be linked to the number of isolated peaks available. As discussed in the introduction of this chapter, the peaks of the oxygen CARS spectrum become more convolved at higher temperatures, which increase the difficulty for the model to identify the correct temperature.

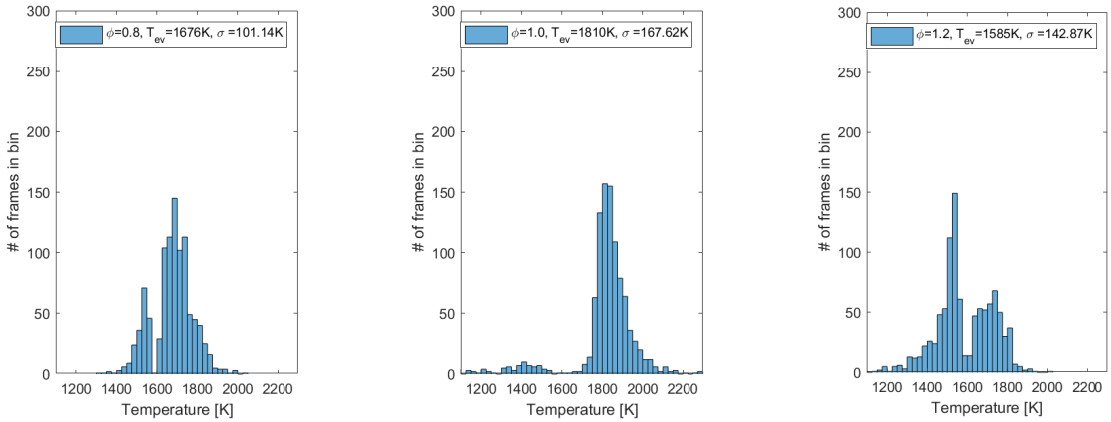

Figure 4.25: Three histograms binned at 20K for position 2 of the M-flame experiment, for different equivalence ratios of 0.8, 1.0 and 1.2 (left to right). The histograms each seem to give two seperate distributions, one centered at a higher and the other centered at a lower temperature. It is assumed that this is caused by the movement of the flame.

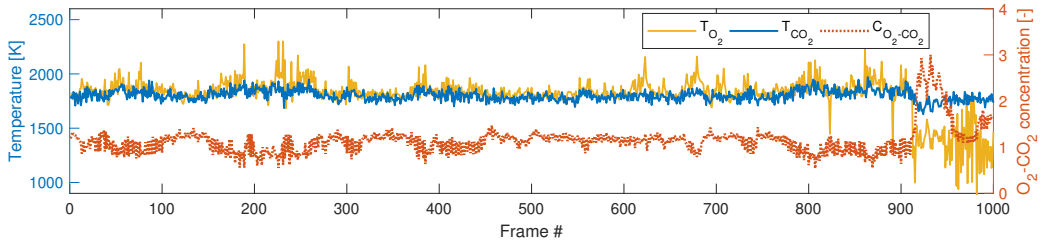

Figure 4.26: O_2 and CO_2 temperature analysis for the M-flame at position 2 for ϕ=1.0, also including the O_2-CO_2 relative concentration, depicting a sudden decrease in temperature for both the O_2 and CO_2 temperature analysis, paired with an increase in oxygen concentration. It is presumed that the strong presence of oxygen is due to entrainment of ambient air into the probed flame region.

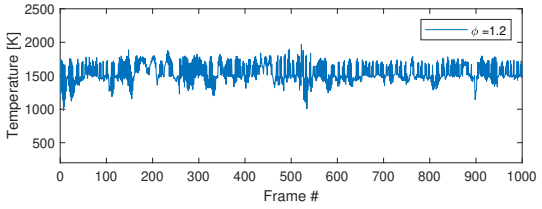

(a) O_2 frame to frame temperature analysis for the M-flame at position 2 for ϕ=1.2 showing significant changes in temperature, alternating between ≈1700K and ≈1500K assumed to lead to the appearance of two separate distributions in the histograms.

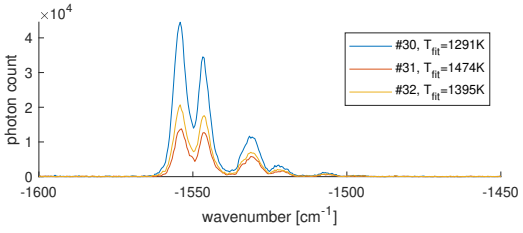

(b) O_2 Q-branch experimental spectra for three successive frames, for the M-flame at position 2 for ϕ=1.2. A significant change in the spectral contour can be observed. While in frame #30 the peak above 1550cm^{-1} is clearly higher than the peak below 1550cm^{-1}, in frame #31 they are nearly equal, leading to a difference in best fit temperature of 170K .

Figure 4.27

4.4. Concentration

This section covers the measurements conducted regarding relative O_2-CO_2 concentration. Due to the proximity of the spectra relative to one another in the CARS spectral domain, O_2 becomes a convenient choice for preforming CO_2 concentration measurements and vice-versa. The section provides evaluated concentrations for the M-flame measurements, the V-flame measurements and the measurements performed in air. First the method is discussed before the results are presented.

4.4.1. Method

The method for relative concentration measurement applies the same fitting procedure as for the thermometric applications. A library is generated for a number of different concentration inputs given as a ratio C=$\frac{O_2}{CO_2}$, ranging from 500 (20% O_2, 0.04% CO_2 in air) to 0 (optimal combustion conditions). Since both concentration and temperature influence relative signal intensities, before determining the concentration, the temperature should be fixed. Using the results from the thermometry, the evaluated temperature can be used to select the concentration library, which the code then applies for the fitting procedure.

The choice is made to use the spectral window of $1370cm^{-1}$ to 1580cm^{-1} since it includes the O_2 Q-branch and CO_2 blue side of its Q-branch. The section is calibrated using the first rotational peak of the O_2 O-branch and the CO_2 Q-branch peak at $1388cm^{-1}$. All in all this should include the most prevalent spectral peaks across all experimental ranges for both O_2 (fundamental Q-branch peak) and CO_2 (blue fundamental Q-branch peak), while presenting enough known peaks for a good calibration. It should be noted that in some cases (e.g. position 4 for M-flame) the O_2 Q-branch peak saturates, in which case the spectral window is adjusted to only view the unsaturated section up to 1530cm^{-1}.

The different types of experiments are aimed to give some interesting insights. The M- and V-flame experiments should be representative to how concentrations in various flame regions change with equivalence ratio and flame region. The air measurement are rather intended to validate the model and have a known temperature, as well as concentration to measure.

4.4.2. Discussion and Results

The results for the experiments are presented in table 4.1 , also including the results for the temperature assessments. First the air experiments, then the M-flame and finally the V-flame experiments are discussed.

The *air* measurements give an almost exact correspondence to the expected conditions. At ambient conditions the expected O_2-CO_2 concentration is about 500, while the result in table 4.1 shows a ratio of 524.47 . The measurement performed on a human breath, corresponds closely with the expected ratio of 16% O_2 and 4% CO_2 according to reference [37]. These experiments show that the method can indeed quite accurately predict relative molecular concentrations, supporting the results conducted in the M- and V-flame.

For the *M-flame* experiments the analysis shows a considerable increase in oxygen concentration, progressing away from the flame front. This increase in oxygen is due to the entrainment of oxygen from the surrounding air into the flame, mixing with the hot combustion gases. It is clear that at position 4, though located outside of the outer flame cone is not representative for ambient conditions. The heating of the flame and partial mixing of the gases leads to a region that is high in oxygen and well above ambient temperatures.

The *V-flame* experiments show a clear decrease in oxygen content as the equivalence ratio is increased. At an equivalence ratio of 1.0 the analysis gives a slight increase in oxygen with respect to ϕ=0.9 . In both cases however, it should be noted that the signal is flat in most of the frames, showing no detectable oxygen peak and is mainly influenced by fluctuations in noise leading to misfits. Thus small signal jumps due to noise can considerably influence the outcome of the concentration analysis.

Another inspection to support that the concentration and temperature analysis perform in a good way is to compare the frame to frame temperature trends to the frame to frame concentration trends. Generally at higher temperatures, less oxygen can be expected since more is being consumed by the combustion process. Higher concentrations in oxygen mean less efficient burning of the air-fuel mixture and thus lower temperatures. Alternatively higher oxygen concentrations can also mean more entrainment of oxygen from the ambient air. Figure 4.28 shows two examples one for the M-flame at position 1, for ϕ=0.8 and one for the V-flame at ϕ=0.5, clearly showing drops in temperature where concentration is high and vice versa. The V-flame experiment shows the temperature dips also described in section 4.2.3 for frame #20-#30 and #210-#250, indicating a significant rise in oxygen concentration for those same frames. The latter adds to the possibility of an air pocket in the gas mixture or a gust of air must have disturb the flame dynamics at the measurement location.

One last point to discuss is the relevance of giving an indication of precision using the standard devia-

tion for a relative concentration ratio of two molecular species of which the concentrations inversely evolve during the combustion process. Looking at the molecular equation of the chemical reaction $CH_4 + 2 \cdot O_2 \rightarrow CO_2 + 2 \cdot H_2O$, and viewing the graphs in fig. 2.10, it is evident that more oxygen means less CO_2 and more CO_2 means less oxygen. Through this relation the variation in relative O_2-CO_2 concentration is amplified, leading to increases in standard deviation. The standard deviations for relative O_2-CO_2 concentrations are generally much higher than for temperature, reaching σ=29% for the M-flame experiment at position 2 for an equivalence ratio of 1.2 (see table 4.1). It is interesting to note that when comparing the graphs in fig. 4.28, the M-flame experiment shows higher oscillations in concentration than the V-flame experiments. Table 4.1, confirms this, with the highest V-flame deviation being about 50% lower than the lowest M-flame standard deviation. Thus, it is probable that the flame oscillations, paired with the inverse relation between O_2 and CO_2 are at the root of these high standard deviations. As such, the flame oscillations and the choice of molecular species do not make it possible to provide a "true" indication of the precision of the applied technique. For a more concise conclusion one would require another molecular species such as Nitrogen (considered an inert gas), with a constant, known concentration to compare it to and give a quantitative estimate. It should be stressed though, that the relative concentration ratios can still be used effectively for determining concentration trends and identifying different flame regions. It is advised though to simultaneously capture the Nitrogen spectrum in future applications to make a quantitative concentration analysis possible.

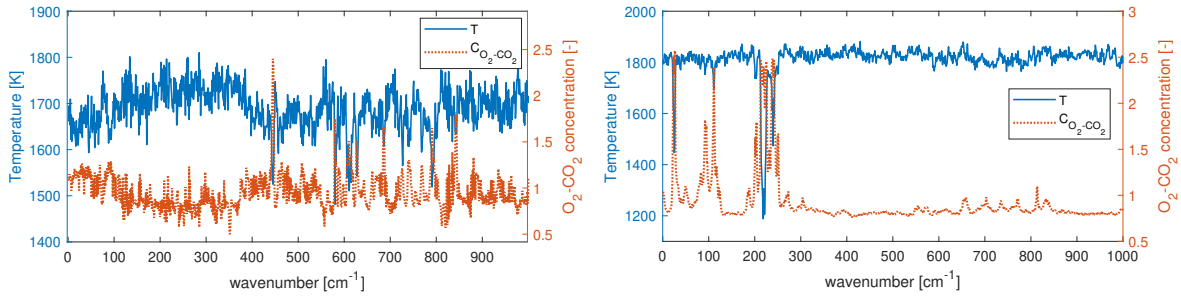

Figure 4.28: Left: Temperature versus concentration graph for M-flame at position 1 for ϕ=0.8 . Right: Temperature versus concentration graph for V-flame for ϕ=0.5 . In both graphs a clear inverse relation can be seen between concentration and temperature.

Table 4.1: The temperature and relative O_2-CO_2 concentration results, evaluated by the model. The standard deviation is given for the temperature evaluations and expected values are provided where applicable. (n/a: not applicable)

Experiment		Temperature				Concentration		
		$T_{expected}$ [K]	T_{ev} [K]	σ [K]	σ [%]	$C_{expected}$ [-]	C_{ev} [-]	σ [%]
Air	**ambient**	293	317	30.7	9.68	500	524.47	10.46
	ambient$_{O_2}$	293	294.82	9.67	3.27	-	-	-
	breath	307	318	7.72	2.51	4	4.13	7.03
M 0.8	**p1**	1900	1712	47.28	2.76	0.59	0.93	18.6
	p2	n/a	1594	65.67	4.11	n/a	1.61	14.91
	p2$_{O_2}$	n/a	1676	101.14	6.03	n/a	-	-
	p3	n/a	893	71.28	7.98	n/a	12.63	-
	p4	n/a	654	70.68	10.81	n/a	23.35	-
M 1.0	**p1**	2038	1901	47.68	2.50	0.19	0.34	16.88
	p2	n/a	1796	49.07	2.73	n/a	0.82	14.83
	p2$_{O_2}$	n/a	1853	81.09	4.37	n/a	-	-
	p3	n/a	974	121.10	12.43	n/a	9.02	-
	p4	n/a	511	99.62	19.49	n/a	40.76	-
M 1.2	**p1**	2046	1793	38.85	2.17	0.025	0.28	16.53
	p2	n/a	1545	106.04	6.86	n/a	2.11	29
	p2$_{O_2}$	n/a	1585	142.87	9.01	n/a	-	-
	p3	n/a	818	117.22	14.33	n/a	18.95	-
	p4	n/a	524	99.30	18.95	n/a	31.56	-
V	**0.5**	n/a	1814	22.97	1.27	n/a	0.9391	4.97
	0.6	n/a	1919	29.95	1.56	n/a	0.5287	2.43
	0.7	n/a	2014	36.63	1.82	n/a	0.2717	8.78
	0.8	1980	2044	34.78	1.70	0.51	0.1527	-
	0.9	n/a	2057	45.36	2.21	n/a	0.096	-
	1.0	2140	2073	45.18	2.18	0.11	0.1051	-

4.5. Comparative discussion on flame results

In this section a closer look is taken at the temperatures that should be measured under ideal conditions in the flames, using *chem1d* as reference. *chem1d* is a 1-D flame simulation software, which gives adiabatic temperature and molecular species concentrations for a one dimensional flame. Based on the figures from *chem1d* (see fig. 4.29), a couple of general trends can be distinguished further away from the flame front, such as $T_{\phi=0.8}<T_{\phi=1.2}<T_{\phi=1.0}$. Other conditions that follow from the graphs, are that the temperatures evaluated at ϕ=0.8 should be about $\Delta T_{\phi=0.8-1.0} \approx$190K lower than the ones for ϕ=1.0 and for ϕ=1.2 roughly $\Delta T_{\phi=1.2-1.0} \approx$60K than for ϕ=1.0.

The following general qualitative assumption is made regarding the temperature profile in the *M-flame* experiment, taking into account the mixing of ambient air into the outer flame cone: $T_{p4}<T_{p3}<T_{p2}<T_{p1}$. Due to air mixing into the outer cone it is difficult to say anything specific about the temperatures at positions 2, 3 and 4 . It is unknown what the influence is of air mixing into the flame is on temperature and concentration. Quantifying this for the experiment would require a thorough flame analysis from a heat transfer perspective, which is outside of the scope of this project. For position 1 however, due to its proximity to the flame front it can be said with relative certainty what the temperature is expected to be. Looking at the description of the experiment in section 3.3 and table 3.1, considering the burner diameter and distance of position 1 from the burner center, it can be argued that position 1 is not more than 1mm away from the flame front. From Figure 4.29 a thickness of about 0.6mm for the flame front can be deduced, using the inflection points of the temperature curve as a reference. Using the graphs in fig. 4.29, this would mean that position 1 is at about 1.6mm from x=0cm . Thus, taking x=1.6mm as reference for position 1, a more quantitative evaluation of the temperature and relative O_2-CO_2 concentration assessments can be made: $T_{0.8}$=1900K,$C_{0.8}$=0.93; , $T_{1.0}$=2038K, $C_{1.0}$=0.34; $T_{1.2}$=2046K, $C_{1.2}$=0.28 . A clear discrepancy can be noticed when looking at the temperatures predicted by *chem1d* and the temperatures observed in the M-flame. All temperatures are off by at least 120K for position 1, giving significantly lower temperatures than should be observed. Based on this assessment, the evaluations are within 9.9%, 6.8% and 12.4% accurate for position 1 at ϕ=0.8, ϕ=1.0, and ϕ=1.2 respectively. In terms of concentration the experiments show a much higher oxygen content than the simulated concentrations from *chem1d*, but correctly reproduces the trend: $C_{1.2}<C_{1.0}<C_{0.8}$. The relative concentration trend from position 1 to 4 is also roughly what could be observed for these flame regions, nearing ambient conditions as one moves outside of the flame. A last interesting observation from *chem1d* is that it shows elevated concentrations in hydrogen for higher equivalence ratios. The richer the mixture, the stronger the H_2 CARS signature becomes, which could explain the appearance of a major peak at 1450cm^{-1}, where the simulated CO_2 spectrum does not predict a peak this high in intensity. Thus it can be said with a high degree of certainty that next to studying the CO_2 and O_2 CARS spectrum in this frequency window, it is also possible to make temperature and relative concentration assessments using the hydrogen peaks at 1450cm^{-1} and 1240cm^{-1}.

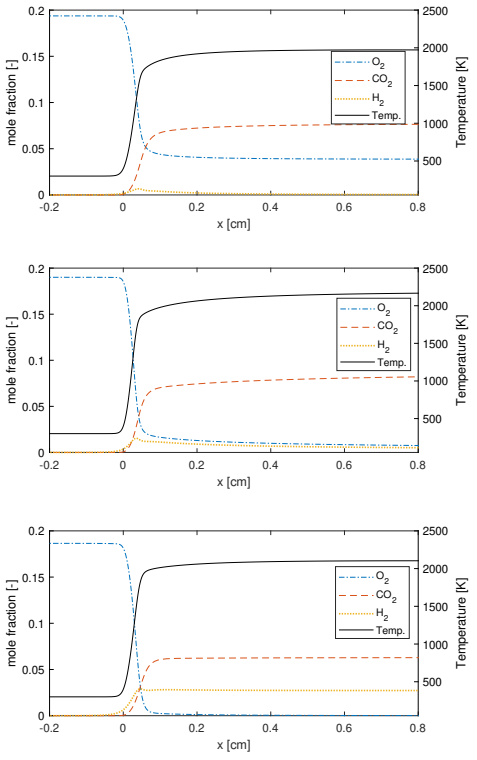

Figure 4.29: *chem1d* concentration predictions for CO_2, H_2 and O_2 along with temperature for ϕ=0.8, ϕ=1.0 and ϕ=1.2 .

The *V-flame* experiment on the other hand, shows a better match with the temperatures from *chem1d*. With the probe location being approximately half a centimeter from either flame front, x=0.5cm is taken as a reference point this gives: $T_{0.8}$=1980K,$C_{0.8}$=0.52; $T_{1.0}$=2140K,$C_{1.0}$=0.11. Comparing to $T_{\phi=1.0}$=2073K and $T_{\phi=0.8}$=2044K evaluated for the V-flame experiment, this means that the thermometric method applied is within 3.23% and 7.5% accurate for ϕ=0.8 and ϕ=1.0 respectively. Thus the model overestimates the temperature for ϕ=0.8 by about 54K and does not adhere to the assumption of $\Delta T_{\phi\approx 0.8-1.0}$=190K either. Nevertheless, a couple of points should be considered here. Under these experimental conditions, and with the knowledge

at hand it is not possible to quantify heat losses. On one hand, mixing of air into this flame region is extremely limited and certainly leads to less heat loss due to mixing with ambient air than the M-flame experiment. On the other hand, it is also unknown to what extent the flame holder can be an influence regarding heat transfer away from the flame. Additionally, it should not be forgotten that the presence of two flame fronts at equal distances from the probe location can possibly lead to an increased heating of the medium. This could result in slightly higher temperatures than would be expected in the presence of a single flame front, making it difficult to see the $chem1d$ data as a valid comparison in this case. Regarding the concentration, it does not seem abnormal to still detect oxygen at stoichiometric conditions (ϕ=1.0), but like mentioned in the previous section, due to the relatively low SNR ratio the V-flame measurements for ϕ=1.0 and ϕ=0.9 are inconclusive in terms of concentration assessment. Considering that the signal is almost flat for these measurements, it can be stated with relative certainty that the oxygen concentration is ≈0 for both cases. For ϕ=0.8, the concentration given by $chem1d$ should be roughly 0.52, meaning that the model underestimates the concentration by a factor of about 3.4 . Thus, the model is not accurate for concentration predictions under flame conditions, when compared to the *chem1d* data. It should be noted nonetheless, that the model manages to capture the increasing trend in concentration. Indicating under which circumstances higher or lower relative O_2-CO_2 concentrations can be found.

5

Conclusion and Outlook

The discussions in the previous chapter clearly bring to light that the applied methods (i.e. one molecular species, one specific spectral window) are adequate for thermometry in their current form. Nonetheless, improvements in the model, but also regarding the experiments need to be included before the technique can be used to its full potential. The study of CO_2 in this spectral range shows promise when it comes to capturing the chemical processes related to hydrocarbon combustion, making the implementation of further improvements well worth the effort. In this chapter the main findings of this project are highlighted and possible development ideas are presented that are deemed most effective in obtaining an accurate, functioning system that can effectively measure CO_2 temperature and concentration.

5.1. Conclusion

The project demonstrates that thermometry and relative O_2-CO_2 concentration measurements are possible looking at the CO_2 Q-branch and O_2 ro-vibrational O-, S- and Q-branches in the CARS spectral range of 1250cm^{-1} to 1680cm^{-1} through ultrabroadband excitation, for temperatures between 294K and 2066K. The theoretical model for CO_2 includes 181 vibrational levels, using the molecular constants provided by Rothmann et al. (1992) [7]. To validate the model, measurements at room temperature are conducted and results from flame experiments are compared to predicted values provided by a 1-D flame simulation tool called $chem1d$. Applying the presented methods, precisions below 3% are achieved for thermometry, accurate to within 2% of the expected value depending on the experimental setup. The model also evaluates relative O_2-CO_2 concentrations under ambient conditions and closely determines the O_2-CO_2 concentration ratio in a human breath.

The project reveals the impact, that a particular experimental platform can have on the outcome of the experiment. Changing from the M-flame experiments to the V-flame experiments and air measurement, essentially provides better results through a more stable medium for probing. This change in setup brings the evaluated temperatures roughly 3% closer to the actual temperature expected from $chem1d$ (1907K for ϕ=1.0, position 1, M-flame to 2073K for ϕ=1.0, V-flame), while the precision improves from 2.55% to 2.18%. It can thus be stated that these changes in accuracy and precision have their origin in the conditions the experimental platform has to offer, rather than the CARS technique itself. The results of the V-flame experiment can thus be judged closer to what the technique can offer than the M-flame experiments since it provides a more homogeneous medium with reduced flame oscillations. The measurements in air using the methods presented in this thesis work, are accurate to within 3.6% (breath) and 1% (ambient) of the expected temperature and show precisions of roughly 2.4% and 3.3% respectively. Conclusively the air and V-flame experiments provide results that are more "true" to the capability of the technique, but remain suspect due to the difficulty of quantifying other effects such influence of the flame holder on heat transfer and entertainment of ambient air.

One other point to mention is that the applied averaging, limits the capability to correct for the flame oscillations. Through using a rather long interaction length and averaging over 40 shots, it is probable that the obtained spectra can become challenging to fit, since they do not necessarily correspond to one specific temperature or concentration ratio. If single shot were used, it would have been possible to track the movement of the flame and compare the evaluated temperature to a more realistic value provided by the flame

simulation software.

The project also shows that this spectral window (1250cm^{-1} to 1680cm^{-1}) offers an adequate range for CARS spectroscopic studies in hydrocarbon combustion applications and fits the Fermi influenced CO_2 Q-branch peaks with acceptable results. It demonstrates that simultaneous (O_2) rotational and (CO_2) vibrational thermometry is possible, while also offering the option of performing relative O_2-CO_2 concentration measurements. This makes the technique applicable to both the reactants and product regions of the flame, since on both sides it is possible to measure both temperature and concentration. The appearance of spectral peaks assumed to originate from hydrogen, which is a major contributing molecule regarding combustion processes, further adds to the interest of looking at this spectral range from a combustion perspective. The project has thus proved successful in demonstrating CO_2 CARS thermometry and to a lesser degree relative O_2-CO_2 concentration measurements in a typical hydrocarbon flame.

5.2. Prospect developments

The code could be improved, in a number of ways. For one it is well worth including the H_2 rotational spectrum to investigate the overlap with the CO_2 peaks. Since the code structure is already present, a mere addition of H_2 constants and their integration into the code to compute the molecular response of Hydrogen, should suffice to examine the CARS spectral influence of hydrogen in this CARS frequency window. Additionally, parallel to the development of the CO_2 model in this project, an M.Sc. project on Hydrogen has also been conducted, thus the necessary framework is already in place to combine the two models. Another possible improvement is to adjust the spectral range used for fitting to the specific flame regime where the experiment is conducted. This makes it possible to neglect peaks that are known to be influenced by the CARS spectra of more than one molecular species.

Further improving the quality of the experimental data is a slightly more complex task. Clearly, optimizing the conditions at the probe volume has a significant impact on the precision and accuracy of the method. The proper evaluation of the conditions inside the flame, even with flame simulation software tools like $chem1d$, proved challenging. Performing a quantitative validation of the model at higher temperatures due to unquantified heat transfer pathways such as mixing of ambient air and the impact of the flame holder or the presence of two flame front in the V-flame. Applying a different type of burner other than a Bunsen burner can aid in testing the theoretical model and further alleviate the problems assumed to originate from flame instabilities. Another option that would help in further validating the code experimentally, would be to look at possibilities to operate on a more stable measurement platform. Flames constitute a dynamic, reactive, multispecies environment, with relatively high flow speeds and shifts in flame position. The use of a gas cell containing pure CO_2, makes it possible to study the CO_2 spectrum without the influence of other molecular species on the CARS signal and create a static gaseous medium for high temperature validation. One other point that proved difficult, is to specify the effects of the method to generate ultrabroadband light on the observed spectrum. The technique makes use of filamentation in air and the generation of an under-dense plasma, making it complicated to characterize its impact. One option would be to look at more stable ways of generating ultrabroadband light, by using glass, crystals or hollow-core fibres. These applications also provide the possibility of increasing the bandwidth even further, which could improve the excitation efficiency for the Raman shifts studied in this work. Another possibility would be to look deeper into the physics and implement corrections based on theory, that help characterize its impact.

One other option to improve the results from the measurements would be to compensate for the flame oscillations. When close to the flame front (e.g. positions 1, 2 and 3) it seems that one does not consistently probe the same location with respect to the flame front (especially the M-flame). In order to improve the signal intensity, the flame experiments were compiled at 40 shots per frame (40ms exposure time), which is insufficient to capture the flame dynamics. Thanks to the 1kHz amplifier system it is possible though to track the flame position and correct for this phenomenon. Reducing the exposure time, can then indeed make it possible to characterize the flame dynamics and thus correct for the position of the flame front, but would lead to a severe reduction in signal intensity. One option would be to split-off part of the main beam and introduce a secondary spectrometer to the setup, which tracks the flame position using single-shot *or* using a second channel on the spectrometer to detect the rotational spectrum, making it possible to quantify the change in flame position over a 40 shot acquisition. It is then possible to either acquire a desired amount of single-shot measurements for the flame spatial dynamics and multi-shot average them in the data processing, *or* run two acquisitions in parallel, one single-shot and the other multi-shot averaged allowing for a similar analysis. Since the code to measure Nitrogen at Raman shifts below 300cm^{-1} and the capability

to track the flame front are already implemented in the system [34], it might be an interesting option to look into. This would in turn also make it possible to perform a more quantative analysis regarding concentration, since nitrogen can be considered as an inert gas. It would make simultaneous single-shot rotational CARS on the N_2/O_2 spectrum and multi-shot ro-vibrational $CO_2/O_2/H_2$ CARS possible, providing data on the flame oscillations and an appealing set of molecular species to study regarding temperature and concentration.

Furthermore, in the discussion related to the oxygen O-branch fits it is mentioned that the argon scan gives an ex-situ characterization of the excitation efficiency since it is not obtained under flame conditions. Implementing in-situ referencing of the excitation efficiency can be achieved by splitting the non-resonant spectrum from the resonant one [41], which could lead to improvements regarding the data processing. In this case however, one would probably need to make a choice on how to distribute the channels if one desires to also capture the flame dynamics using single shot and/or measure nitrogen. Angle tuning and precise splitting of the beam to make a two-channel analysis possible, is already challenging in itself, possibly making the implementation of a third channel even more intricate. In this case a secondary spectrometer might come in handy, since the split-off beam does not have to be re-directed to the same camera, possibly simplifying the problems otherwise encountered in two-channel calibration.

Summing up, this gives the following options for future development that can lead to a more reliable application of the presented CO_2 CARS model for combustion applications in a typical hydrocarbon flame:

- Include the molecular response of hydrogen to study its effects on the the spectral window from 1250cm^{-1} to 1680cm^{-1} and to further exploit the multi-species diagnostic potential it has to offer.
- Make use of a second channel and/or spectrometer to capture the flame dynamics using single-shot from the pure rotational nitrogen spectrum allowing for a more conclusive statement on concentration and temperature, or alternatively allowing for in-situ non-resonant referencing.
- Look into different techniques for more stable ultrabroadband generation and possibly even broader excitation of the Raman shifts.
- Validate the model at higher temperatures using a more stable combustion environment by using a different burner type (e.g. McKenna burner) and/or use a gas cell.

Acknowledgements

I would like to spend a few words to thank the people that helped me most in completing this project and kept supporting me throughout. Even though these few words can only offer a glimpse of the importance they had in my eyes, these acknowledgements at least give me a small opportunity to try.

My biggest thanks go to Francesco Mazza, who took on the role as my daily supervisor and mentor throughout the project. Without his help the project would not have been even half as learnsome as it has been. Your thorough knowledge on the theory regarding CARS and your inherent interest in other surrounding topics such as quantum theory, impressed me on a daily basis. This, together with a strong working spirit, even through times of frustration, and being a constant person I could count on, leaves no doubt in my mind that many successful works lie ahead of you and the people you are working with. That being said, I also enjoyed our talks on best italian snacks from spianatas to torta fritta while performing the famed argon scans at the end of a long experimental campaign.

Then I would also like to offer my special thanks to Alexis Bohlin. Next to the fact that he offered me a great opportunity through getting me involved in this thesis topic, I am especially grateful for his sincere efforts to get other M.Sc. students and myself involved in the subject matter and create a feeling of connection throughout these trying times of COVID-19. Thanks to his efforts, the project became "whole" in my eyes, enabling me as a student to get a good look at what it takes to be a researcher from seminars, to theory, to experiment, to results and finally conclusions. The organized seminars were of great value to me from an educational point of view, especially in my literature study phase. Next to that, I was also happy that they did not always end in a formal "goodbye", but rather finished with a refreshing update on how everyone is doing and regularly led to off-the-topic talks such as ice skating and swedish meatballs.

Two people that can also not be left out on this list are Dmitrii Kliukin and Leonardo Castellanos. Thank you for helping out in the lab and sharing your ideas on how best to procede whenever I (or sometimes even Francesco and I) got stuck on something, be it the code or the experimental setup. The two of you combined together with Francesco are great people to work with and form a talented pool of individuals to gain knowledge from. Apart from serious hard work, I am happy that there was room for an occasional joke and some time to get to know one another. I think it can not be underestimated how important it is to have a good working atmosphere for the sake of everyone's productivity. In my opinion the three of you strike a perfect balance in that regard.

Additionally, my fellow M.Sc. student Thijmen Klijn Velderman can not be forgotten either. I am glad for the calls, chats and meetings we had, where we could share some of the obstacles we were facing. It was great to have gone through many of the stages regarding a thesis project together and have a sparring partner throughout.

Last but not least, I would like to thank my family, friends and especially also my girlfriend for supporting me for the duration of the project.

Bibliography

[1] IPCC. “Proposed outline of the special report in 2018 on the impacts of global warming of 1 . 5 ° C above pre-industrial levels and related global greenhouse gas emission pathways , in the context of strengthening the global response to the threat of climate”. In: *Ipcc - Sr15* 2.October (2018), pp. 17–20.

[2] E.O. Potma and S. Mukamel. *Theory of coherent Raman scattering*. 2013, pp. 3–42. ISBN: 9781439867662.

[3] A.C. Eckbreth. *Laser Diagnostics for Combustion Temperature and Species*. Ed. by William A. Sirigano. Second. Taylor & Francis, 1996. ISBN: 90-5699-532-4.

[4] A.C. Eckbreth. “Recent advances in laser diagnostics for temperature and species concentration in combustion”. In: *Symposium (International) on Combustion* 18.1 (1981), pp. 1471–1488. ISSN: 00820784. DOI: 10.1016/S0082-0784(81)80150-6.

[5] A. Bohlin, B.D. Patterson, and C.J. Kliewer. “Communication: Simplified two-beam rotational CARS signal generation demonstrated in 1D”. In: *Journal of Chemical Physics* 138.8 (2013). ISSN: 00219606. DOI: 10.1063/1.4793556.

[6] A. Kessel. *Generation and parametric amplification of few-cycle light pulses at relativistic intensities*. Springer, 2017. ISBN: 9783319928425.

[7] L. S. Rothman et al. “Energy levels, intensities, and linewidths of atmospheric carbon dioxide bands”. In: *Journal of Quantitative Spectroscopy and Radiative Transfer* 48.5-6 (1992), pp. 537–566. ISSN: 00224073. DOI: 10.1016/0022-4073(92)90119-O.

[8] M. Basire et al. “Fermi resonance in CO2: Mode assignment and quantum nuclear effects from first principles molecular dynamics”. In: *Journal of Chemical Physics* 146.13 (2017). ISSN: 00219606. DOI: 10.1063/1.4979199.

[9] V.G. Arakcheev et al. “Collisionally induced dephasing and rotational energytransfer in the CO2Fermi dyad ‘blue’ Q-branch1388 cm-1”. In: *Journal of Raman Spectroscopy* 38.April (2007), pp. 1046–1051. ISSN: 10974555. DOI: 10.1002/jrs.1783.

[10] V.G. Arakcheev et al. “Collisonally induced dephasing and rotational energy transfer in the CO2 Fermi dyad ’red’ Q-branch 1285 cm-1”. In: *Journal of Raman Spectroscopy* 38.April (2007), pp. 1538–1553. ISSN: 10974555. DOI: 10.1002/jrs.1780.

[11] D.A. Long. *The Raman effect: a unified treatment of the theory of Raman scattering by molecules. 2002*. Vol. 8. 2002, pp. 21–22. ISBN: 0471490288.

[12] J. D. Miller et al. “Single-shot gas-phase thermometry using pure-rotational hybrid femtosecond / picosecond coherent anti-Stokes Raman scattering”. In: *Optics express* 19.16 (2011), pp. 15627–15640.

[13] B.D. Prince et al. “Development of simultaneous frequency- And time-resolved coherent anti-Stokes Raman scattering for ultrafast detection of molecular Raman spectra”. In: *Journal of Chemical Physics* 125.4 (2006). ISSN: 00219606. DOI: 10.1063/1.2219439.

[14] S.P. Kearney. “Hybrid fs/ps rotational CARS temperature and oxygen measurements in the product gases of canonical flat flames”. In: *Combustion and Flame* 162.5 (2014), pp. 1748–1758. ISSN: 15562921. DOI: 10.1016/j.combustflame.2014.11.036.

[15] S.P. Kearney, D.J. Scoglietti, and C.J. Kliewer. “Hybrid femtosecond/picosecond rotational coherent anti-Stokes Raman scattering temperature and concentration measurements using two different picosecond-duration probes”. In: *Optics Express* 21.10 (2013), p. 12327. ISSN: 1094-4087. DOI: 10.1364/oe.21.012327.

[16] J.D. Miller. “Hybrid femtosecond/picosecond coherent anti-Stokes Raman scattering for gas-phase temperature measurements”. PhD thesis. Iowa State University, 2012.

[17] F. Vestin, K. Nilsson, and P.-E. Bengtsson. “Validation of a rotational coherent anti-stokes Raman spectroscopy model for carbon dioxide using high-resolution detection in the temperature range 294-1143k”. In: *Applied Optics* 47.11 (2008), pp. 1893–1901. ISSN: 15394522. DOI: 10.1364/AO.47.001893.

[18] M. Afzelius et al. “Pure rotational coherent anti-Stokes Raman spectroscopy in mixtures of CO and N2”. In: *Applied Optics* 43.36 (2004), pp. 6664–6672. ISSN: 15394522. DOI: 10.1364/AO.43.006664.

[19] M. Marrocco. “Comparative analysis of Herman-Wallis factors for uses in coherent anti-Stokes Raman spectra of light molecules”. In: *Journal of Raman Spectroscopy* 40.7 (2009), pp. 741–747. ISSN: 03770486. DOI: 10.1002/jrs.2201.

[20] M. A. Buldakov et al. “Role of intramolecular interactions in Raman spectra of N2 and O2 molecules”. In: *Journal of Molecular Spectroscopy* 217.1 (2003), pp. 1–8. ISSN: 00222852. DOI: 10.1016/S0022-2852(02)00012-7.

[21] G. Rouille et al. “High-resolution stimulated Raman spectroscopy of O2”. In: *Journal of Molecular Spectroscopy* 154.1 (1992), pp. 372–382. ISSN: 1096083X. DOI: 10.1016/0022-2852(83)90029-2.

[22] G. Tejeda, B. Maté, and S. Montero. “Overtone Raman spectrum and molecular polarizability surface of CO 2”. In: *The Journal of Chemical Physics* 103.2 (1995), pp. 568–576. ISSN: 00219606. DOI: 10.1063/1.470091.

[23] M. Gu, A. Satija, and R.P. Lucht. “CO2 chirped-probe-pulse femtosecond CARS thermometry”. In: *Proceedings of the Combustion Institute* 000 (2020), pp. 1–8. ISSN: 15407489. DOI: 10.1016/j.proci.2020.06.134.

[24] A. Bohlin, P.-E. Bengtsson, and M. Marrocco. “On the sensitivity of rotational CARS N2 thermometry to the Herman-Wallis factor”. In: *Journal of Raman Spectroscopy* 42.10 (2011), pp. 1843–1847. ISSN: 03770486. DOI: 10.1002/jrs.2869.

[25] G. Placzek and E. Teller. “"Die Rotationsstruktur der Ramanbanden mehratomiger Moleküle"”. In: *Zeitschrift für Physik* 81.11-12 (1933), p. 839. ISSN: 14346001. DOI: 10.1007/BF01342084.

[26] D. C. M. van den Bekerom et al. “ How the alternating degeneracy in rotational Raman spectra of CO 2 and C 2 H 2 reveals the vibrational temperature ”. In: *Applied Optics* 57.20 (2018), p. 5694. ISSN: 1559-128X. DOI: 10.1364/ao.57.005694.

[27] L. Martinsson et al. “A test of different rotational Raman linewidth models: Accuracy of rotational coherent anti-Stokes Raman scattering thermometry in nitrogen from 295 to 1850 K”. In: *The Journal of Chemical Physics* 99.4 (1993), pp. 2466–2477. ISSN: 00219606. DOI: 10.1063/1.466197.

[28] A. Bohlin. “Development and application of Pure Rotational CARS for Reactive Flows”. PhD thesis. Lund University, 2012. ISBN: 9789174733235.

[29] D.A. Long et al. “The air-broadened, near-infrared CO2 line shape in the spectrally isolated regime: Evidence of simultaneous Dicke narrowing and speed dependence”. In: *Journal of Chemical Physics* 135.6 (2011). ISSN: 00219606. DOI: 10.1063/1.3624527.

[30] R. H. Dicke. “The Effect of Collisions upon the Doppler Width of Spectral Lines”. In: *Physical Review* 89.2 (1953), pp. 472–473.

[31] L. Rosenmann et al. “Accurate calculated tabulations of IR and Raman CO 2 line broadening 300-2400-K temperature range”. In: *Applied Optics* (1988), pp. 0–4.

[32] L. A. Rahn and R. E. Palmer. “Studies of nitrogen self-broadening at high temperature with inverse Raman spectroscopy”. In: *Journal of the Optical Society of America B* 3.9 (1986), p. 1164. ISSN: 0740-3224. DOI: 10.1364/josab.3.001164.

[33] B. Lavorel et al. “Study of collisional effects on band shapes of the $v1/2v2$ Fermi dyad in CO2 gas with stimulated Raman spectroscopy. I. Rotational and vibrational relaxation in the $2v2$ band”. In: *The Journal of Chemical Physics* 93.4 (1990), pp. 2176–2184. ISSN: 00219606. DOI: 10.1063/1.459049.

[34] L. Castellanos et al. “Pure-rotational 1D-CARS spatiotemporal thermometry with a single regenerative amplifier system”. In: *Optics Letters* 45.17 (2020), pp. 4662–4665. ISSN: 0146-9592. DOI: 10.1364/ol.398982.

[35] E.M. Greitzer, C.S. Tan, and M.B. Graf. *Internal Flows - Concepts and Applications*. Vol. 53. 9. Cambridge Univserity Press, 2004, pp. 1689–1699. ISBN: 9788578110796.

[36] A.F. Mills. *Basic heat and mass transfer*. 2nd. Pearson, 2013. ISBN: 9781292042480.

[37] D. Zhao et al. “A novel real-time carbon dioxide analyzer for health and environmental applications”. In: *Sensors and Actuators, B: Chemical* 195 (2014), pp. 171–176. ISSN: 09254005. DOI: 10.1016/j.snb.2013.12.110.

[38] J. M. Cowan et al. “The relationship of normal body temperature, end-expired breath temperature, and BAC/BrAC ratio in 98 physically fit human test subjects”. In: *Journal of Analytical Toxicology* 34.5 (2010), pp. 238–242. ISSN: 01464760. DOI: 10.1093/jat/34.5.238.

[39] A. I. Krikunova. “M-shaped flame dynamics”. In: *Physics of Fluids* 31.12 (2019). ISSN: 10897666. DOI: 10.1063/1.5129250.

[40] W. D. Kulatilaka, J. R. Gord, and S. Roy. “Effects of O2-CO2 polarization beating on femtosecond coherent anti-Stokes Raman scattering (fs-CARS) spectroscopy of O2”. In: *Applied Physics B: Lasers and Optics* 102.1 (2011), pp. 141–147. ISSN: 09462171. DOI: 10.1007/s00340-010-4188-2.

[41] F. Mazza et al. “Coherent Raman imaging thermometry with in-situ referencing of the impulsive excitation efficiency”. In: *Proceedings of the Combustion Institute* 000 (2020), pp. 1–10. ISSN: 15407489. DOI: 10.1016/j.proci.2020.06.360.

[42] G. Millot et al. “Collisional effects in the stimulated Raman Q branch of O2 and O2-N2”. In: *The Journal of Chemical Physics* 96.2 (1992), pp. 961–971. ISSN: 00219606. DOI: 10.1063/1.462116.

A

Spectroscopic constants

Table A.1: List of constants used in this work for the calculation of the O_2 ro-vibrational O-, S- and Q-branches, from Rouillé et al. (1992)[21].

	$\mathbf{v}_0$	$\mathbf{v}_1$	$\mathbf{v}_2$	$\mathbf{v}_3$	
Symbol	**value**	**value**	**value**	**value**	**unit**
Be	1.4456	1.4456	1.4456	1.4456	[cm^{-1}]
ω_e	1580	1580	1580	1580	[cm^{-1}]
$\mathbf{B}_v$	1.436764	1.42186454	1.406119	1.390425	[cm^{-1}]
$\mathbf{D}_v$	4.84256e-6	4.8418e-6	4.8410e-6	4.8402	[cm^{-1}]
$\mathbf{H}_v$	2.8e-12	2.8-12	2.8e-12	2.8e-12	[cm^{-1}]
$\mathbf{G}_v$	0	1556.384	1532.86	1509.5275	[cm^{-1}]
λ_v	1.984751332	1.989578940	1.99440656	1.99923418	[cm^{-1}]
λ_v'	1.94521e-6	2.10924e-6	2.2733e-6	2.4374	[cm^{-1}]
λ_v"	1.103e-11	1.103e-11	1.103e-11	1.103e-11	[cm^{-1}]
μ_v	-8.425390e-3	-8.445771e-3	-8.466152e-3	-8.486533e-3	[cm^{-1}]
μ_v'	-8.106e-9	-8.264e-9	-8.42e-9	-8.85e-9	[cm^{-1}]
μ_v"	-4.7e-14	-4.7e-14	-4.7e-14	-4.7e-14	[cm^{-1}]

Table A.2: Rosenmann polynomial fitting constants for CO_2 self broadening and broadened by N_2 and O_2.

	$\mathbf{CO_2}$-$\mathbf{CO_2}$	$\mathbf{CO_2}$-$\mathbf{N_2}$	$\mathbf{CO_2}$-$\mathbf{O_2}$
constant	**value**	**value**	**value**
$\mathbf{a}_2$	0.00466	0.002149	0.003982
$\mathbf{a}_1$	-1.172	-0.5323	-0.6797
$\mathbf{a}_0$	125.3	91.69	82.93
$\mathbf{b}_2$	0.00003078	-0.000007544	0.000008167
$\mathbf{b}_1$	-0.006017	-0.0006306	-0.001798
$\mathbf{b}_0$	0.7706	0.7146	0.6947

Table A.3: MEG fitting constants for O_2 self broadening and broadened by N_2 from Millot et al. (1992) [42].

	$\mathbf{O_2}$-$\mathbf{O_2}$		$\mathbf{O_2}$-$\mathbf{N_2}$	
constant	**value**	**unit**	**value**	**unit**
N	1.32	[-]	1.31	[-]
α	0.0167	[cm^{-1} atm^{-1}]	0.017	[cm^{-1} atm^{-1}]
β	1.45	[-]	1.41	[-]
δ	1.32	[-]	1.30	[-]